# An electrostatic ion trap for laser and nuclear spectroscopy at the IGISOL

A thesis submitted to the University of Manchester for the degree of

Doctor of Philosophy (PhD)

in the Faculty of Engineering and Physical Sciences

**2013**

**Duncan J. S. Johnson**

**School of Physics and Astronomy,**

**Nuclear Physics Group**

# Contents

Total word count: 29,856

# List of Figures

# List of Tables

# Abstract

The thesis “An electrostatic ion trap for laser and nuclear spectroscopy at the IGISOL" was submitted to The University of Manchester on $11^{th}$ September 2013 by Mr Duncan James Stewart Johnson for the degree of Doctor of Philosophy.

This thesis presents the theoretical modelling and commissioning of the laser station at the newly constructed IGISOL 4 facility. The experimental techniques and apparatus of the facility, focusing on a line dedicated to laser spectroscopy, are described, followed by details on simulations of the beam-line.

First spectroscopic data has been acquired at IGISOL 4. The isotope shifts and hyperfine structure of stable and radioactive molybdenum isotopes were acquired using collinear laser spectroscopy. The spectroscopy of this element was chosen in order to compare the results with those previously acquired at IGISOL 3. The isotope shifts and hyperfine dipole constants calculated were found to agree and the hyperfine structure of the $4d^4(^5D)5s\ ^6D_{1/2}$ to $4d^4(^5D)5p\ ^6F_{1/2}$ transition in $^{107}$Mo has been observed for the first time.

A new electrostatic ion trap (ConeTrap) has been designed for trapping and optical pumping of ions in high vacuum using realistic ion optical simulations. The ConeTrap has been designed with an extended central section in order to facilitate the optical pumping of contained ions. The trap uses asymmetric voltages to achieve greater extraction efficiency and an acceptance time of $\sim$10 $\mu$s. Fast high-voltage switching circuitry has been created, with fall and rise times of $<$240 ns and $<$700 ns respectively, for dynamic trapping of ion bunches. The IGISOL ConeTrap has been designed and built for axial and radial optical pumping, however several other possible applications are also presented. These applications, to be deployed at the IGISOL 4, include using the ConeTrap as a potential energy elevator, a “high-density” ConeTrap for two-photon spectroscopy, a “dual-stability” ConeTrap that can provide pure, doubly-ionised bunches, a ConeTrap designed for radiation detection for spectroscopy and lifetime measurements and a combination of the ConeTrap and the current IGISOL light collection region for collinear laser spectroscopy of trapped ions.

# Declaration

No portion of the work referred to in this thesis has been submitted in support of an application for another degree or qualification of this or any other university or other institute of learning.

# Copyright statement

1. The author of this thesis (including any appendices and/or schedules to this thesis) owns any copyright or related rights in it (the "Copyright") and he has given The University of Manchester the right to use such Copyright for any administrative, promotional, educational and/or teaching purposes.

2. Copies of this thesis, either in full or in extracts and whether in hard or electronic copy, may be made **only** in accordance with the Copyright, Designs and Patents Act 1988 (as amended) and regulations issued under it or, where appropriate, in accordance with licensing agreements which the University has from time to time. This page must form part of any such copies made.

3. The ownership of certain Copyright, patents, designs, trade marks and other intellectual property (the "Intellectual Property") and any reproductions of copyright works in the thesis, for example graphs and tables ("Reproductions"), which may be described in this thesis, may not be owned by the author and may be owned by third parties. Such Intellectual Property and Reproductions cannot and must not be made available for use without the prior written permission of the owner(s) of the relevant Intellectual Property and/or Reproductions.

4. Further information on the conditions under which disclosure, publication and commercialisation of this thesis, the Copyright and any Intellectual Property and/or Reproductions described in it may take place is available in the Uni-

versity IP Policy (see http://www.campus.manchester.ac.uk/medialibrary/-policies/intellectualproperty.pdf), in any relevant Thesis restriction declarations deposited in the University Library, The University Library's regulations (see http://www.manchester.ac.uk/library/aboutus/regulations) and in The University's policy on presentation of Theses.

# Acknowledgments

I would, first of all, like to express my greatest thanks to my supervisor Paul 'Batman' Campbell for providing his help and support (and for buying more rounds than I did). My PhD has been a fantastic learning experience and Paul's advice has been invaluable. I would also like to thank his 'intrepid Robin' Bradley Cheal for his indispensable help in Finland.

While my professional skills have benefited from the expertise of my supervisor and others at both Manchester and Jyväskylä, my sanity has also been kept intact thanks to the many wonderful people I have met. These include Richard and Alex, with whom I endured the extremes of Finnish weather, my friend Ross Edwards, for letting me know that the letter he wrote me didn't, in fact, come from the University, and an especially big thanks to my friend Andrew Pollitt (who probably tested my sanity more than anything else). I would also like to take this opportunity to thank my friend Chris Perry, with whom I bested undergraduate physics.

Finally, my thanks go out to my family for their support (especially financial) and to my friends back in 'The Bridge' for always welcoming me back with a smile and a pint.

*"Trust those who seek the truth,*

*be wary of those who say they've found it."*

# CHAPTER 1

# Introduction

Hyperfine structure in atomic transitions was first observed in the late 19th century. An explanation for the phenomenon was only proposed in 1924 by Pauli [1] who attributed it to the interaction between the nucleus and the surrounding electron cloud. The largest contribution to hyperfine structure comes from the magnetic dipole moment of the nucleus interacting with the magnetic field created by the motion of the electron cloud. In 1935 hyperfine structure arising from the interaction of the electric quadrupole moment of the nucleus with the electric field gradient caused by the electron cloud was described by Schüler and Schmidt [2] and the isotope shift, caused by changes in nuclear size and charge distribution between isotopes, was modeled in the early 1930s [3, 4]. Hyperfine structure splittings are usually two to three orders of magnitude smaller than the fine structure of atomic states and components can overlap due to line broadening. High resolution lasers and the minimization of Doppler broadening are therefore required for measurement of the hyperfine structure.

The IGISOL facility, JYFL, measures the hyperfine structure of atomic transitions using collinear laser spectroscopy and high resolution mass spectroscopy is performed using a double-penning trap, JYFLTRAP. Collinear laser spectroscopy was originally developed in the 1970s [5] and measures the hyperfine structure of atomic transitions by overlapping a high resolution laser beam with a counter-propagating

ion beam accelerated to high energy (keV). The increase in energy reduces the velocity spread of ions in the axial direction, therefore reducing the Doppler broadening of the atomic transitions and allowing the hyperfine structure to be measured with greater resolution and, critically, greater efficiency. The collinear laser spectroscopy station at the IGISOL was established in the late 1990s [6, 7] and has since become an integral part of the facility.

## 1.1 History of the IGISOL facility

The IGISOL method was originally developed in the 1980s at the University of Jyväskylä to quickly (<ms) provide chemically non-selective, mass separated radioactive ion beams [8]. The original IGISOL was moved to the K130 cyclotron laboratory in 1991 [9]. The move gave the new IGISOL 2 access to the K130 cyclotron, which, by the late 90s, could provide up to 50 $\mu$A current and 65 MeV proton beams (compared to the 100 nA current and 20 MeV limit of the previous M20 cyclotron [10]).

An ion-beam cooler and buncher (Cooler-Buncher) was installed in 1999 and enabled the facility to cool and reduce the energy spread of the ion beam [11]. This both provided reduced Doppler broadening for laser spectroscopy and decoupled the ion-beam energy spread from the conditions in the IGISOL. The bunching of the ions enabled bunched-beam spectroscopy to be performed, which greatly reduced background from random laser scatter [12], and allowed the injection of ion bunches into the Penning Trap that was installed after the Cooler-Buncher [13]. Another advantage of using the Cooler-Buncher is the collisional relaxation of ions into the ground state during cooling, thus depopulating metastable states formed in the IGISOL. The cooled ions can then be optically pumped into a chosen metastable state if the ground state is not suitable for spectroscopy [14].

The facility was upgraded in 2003 with greater radiation shielding, a larger target

chamber and improved vacuum pumps [15]. These improvements resulted in the IGISOL 3 and enabled the use of greater intensity proton beams.

The IGISOL 3 facility at Jyväskylä was dismantled, redesigned and moved to a purpose built laboratory in 2011. The new facility, IGISOL 4, still has access to the old K130 cyclotron, but now has a new, dedicated cyclotron (MCC30/15) that provides 30 MeV proton and 15 MeV deuteron beams with respective currents of up to 200 $\mu$A and 62 $\mu$A already achieved [16]. A new electrostatic ion trap, ConeTrap, designed using ion optical simulations, has been constructed and installed in a high-voltage (low energy) region beyond the Cooler-Buncher. The high voltage region and ConeTrap will allow the optical pumping of slow moving ions in vacuum; either traveling in the beam-line or confined within the ConeTrap.

## 1.2 This work

Ion optical simulations have been performed to optimise beam transport through the new high voltage region of the IGISOL beam-line. The voltages required on the IGISOL quadrupole deflectors, to divert ions by 90 degrees, and the voltage switch timing required for injection and extraction of the ConeTrap have been determined. An Einzel lens was designed and built to transport ions between the deflectors and into the ConeTrap.

The electrostatic ion trap, ConeTrap, has been designed and installed at the IGISOL facility. The trap was built to enable the optical-pumping of ions in vacuum. At IGISOL 3, optical-pumping was performed on ions contained in the, gas-filled, Cooler-Buncher in order to populate metastable states. This allowed collinear laser spectroscopy to be performed from a metastable state when transitions from the ground state were either too weak for spectroscopy or beyond the range of the high-resolution dye laser. However, high-energy states were lost through collisional relaxation inside the Cooler-Buncher. Optical-pumping of ions in vacuum allows

these high-lying states to be populated, thus expanding the range of isotopes available for investigation at the IGISOL.

Ion optics simulations were used to design the ConeTrap for the injection and extraction of ~10 $\mu$s ion bunches and with an extended central region of uniform potential for optical-pumping. Circuitry was created for dynamic trapping of the ion bunches with rise and fall times below 1 $\mu$s. Alternative designs of the ConeTrap were investigated for other possible applications at the IGISOL facility, including a "high-density" ConeTrap for two-photon transition experiments, a "dual-stability" ConeTrap to provide a pure bunch of $2^+$ ions and a "fast-beam" ConeTrap that can be used for collinear laser spectroscopy of trapped ions. A non-optical ConeTrap has been designed specifically for radiation detection, for spectroscopy and to determine the lifetimes of radioactive isotopes, and can accept ion bunches of up to 22 $\mu$s

The first spectroscopic results from the new IGISOL 4 facility have been obtained in this work. Isotope shifts and hyperfine structure coefficients were measured for the stable isotopes of molybdenum ($^{92,94-98,100}$Mo) and some radioactive isotopes $^{102,104,106}$Mo to compare with similar measurements made at the IGISOL 3 facility [17]. Measurements of the hyperfine structure and isotope shift for the $^{107}$Mo radioactive isotope have been achieved for the first time.

Chapter 2 summarizes the theoretical considerations pertinent to this work. A description of the new IGISOL beam-line is given in Chapter 3, followed by details of the simulation of the beam-line. A description of quadrupole traps and Penning traps, and their use as the Cooler-Buncher and JYFLTRAP at Jyväskylä, are given in Chapter 4, followed by the details of the ConeTrap simulations, construction and circuitry, and possible applications in Chapter 5 (with ConeTrap designs considered for the future presented in Appendix B). The results of the new molybdenum experiments and their comparison to previous measurements are presented in Chapter 6, followed by a summary of this thesis in Chapter 7.

# CHAPTER 2

# Theoretical considerations

A dedicated station at the IGISOL facility is used to determine characteristics of nuclei by measuring the hyperfine structure of atomic transitions. These splittings are caused by the interaction between the electron cloud and the nucleus. They are observed using collinear laser spectroscopy, where high-resolution laser light is scanned over the atomic transition with scattered photons counted to determine resonance. The form of the hyperfine structure is then used, with comparisons to adjacent isotopes, to calculate model-independent properties of the nucleus. This Chapter describes the nuclear and atomic theory behind the hyperfine structure phenomenon and the theory used to acquire the high resolution laser light needed for its measurement.

## 2.1 Nuclear theory

The matter radius of the nucleus has been experimentally determined to be $R \simeq R_0 A^{1/3}$ where $R_0 = 1.25$ fm. The binding energy of the nucleus is smooth (approximately saturated per nucleon above $A \sim 10 - 20$) as the nucleus increases in size, with only minor structural deviations. The observation of "magic numbers" in these deviations, which coincide with sharp changes in the nuclear radius and nucleon separation energies, led to the development of the nuclear shell model, which separates

the neutrons and protons into well-defined orbital shells. The shell model is found to accurately predict the properties of nuclei in low mass regions and around shell closures where the strong binding of the nucleus inhibits collective motion. In the model, the protons and neutrons within the nucleus each have both orbital (**l**) and intrinsic (**s**) angular momentum. To differentiate it from the total atomic orbital momentum, **J**, the total nuclear angular momentum is conventionally denoted with **I** and is referred to as the 'nuclear spin'. The energy levels of the nuclear shell model can be calculated by solving the Schrödinger equation for the Woods-Saxon potential and spin-orbit coupling term. The Woods-Saxon potential and spin-orbit coupling term are given by,

$$V(r) = \frac{-V_0}{1 + \exp(\frac{r-R}{a})} + V_{SO}\ \mathbf{l} \cdot \mathbf{s}$$

where $V_0$ is the potential depth, $R$ is the mean radius, $a$ is the diffusivity of the nuclear surface and $V_{SO}$ is the spin-orbit coupling term [18].

The spin-orbit term arises due to the strong coupling of the nucleon orbital and intrinsic angular momenta, resulting in them jj-coupling to a total angular momentum ($\mathbf{j} = \mathbf{l} + \mathbf{s}$) and total nuclear spin ($\mathbf{I} = \mathbf{j_1} + \mathbf{j_2} + ...$). The nuclear spin-orbit term is inverted in comparison to the atomic spin-orbit coupling, therefore inverting the ordering of the split energy levels resulting in higher **j** orbitals shifting to lower energies.

The spherical single-particle nuclear shell model provides estimates for the nuclear magnetic dipole (known as Schmidt estimates) and electric quadrupole moments. The magnetic dipole moment is given by,

$$\frac{< \mu >_{l+1/2}}{\mu_N} = \left(j - \frac{1}{2}\right) g_l + \frac{1}{2} g_s$$

for nuclear orbitals of $\mathbf{j} = \mathbf{l} + \frac{1}{2}$ and,

$$\frac{<\mu>_{l-1/2}}{\mu_N} = \frac{j(j+\frac{3}{2})}{(j+1)} g_l - \frac{1}{2(j+1)} g_s$$

for nuclear orbitals of $\mathbf{j} = \mathbf{l} - \frac{1}{2}$, where $\mu_N$ is the nuclear magneton and $g_l$ and $g_s$ are g-factors. The g-factors, $g_l$ and $g_s$, are 1 and 5.586 for protons and 0 and -3.826 for neutrons respectively.

The electric quadrupole moments produced by a single valence proton, $< Q^{s.p.} >$, and that for $n$ protons in the same sub-shell, $< Q >$, are,

$$< Q^{s.p.} >= -\frac{j-\frac{1}{2}}{(j+1)} < r^2 >$$
$$< Q >=< Q^{s.p.} > \left(1 - 2\frac{n-1}{2j-1}\right).$$

Large deviations between the estimates of the quadrupole moment and experimental values led to the development of collective models, which describe the nucleus in terms of macroscopic effects such as the deformation of the nucleus and allow the possibility of vibrational and rotational excitations [18]. A simple liquid drop model can also be used to approximate the binding energies of nuclei, using the semi-empirical mass formula, and has been used to model the fission process [19]. The incompressible drop and rigid rotor models can be used to describe the vibrational and rotational states, the latter dominating in heavy nuclei and in areas far from shell closures.

The need to combine the shell model with the deformation of the nucleus led to the creation of the Nilsson model (deformed shell model) [20]. The Nilsson model describes the orbits of unpaired valence nucleons in the potential created by a deformed nuclear core [21]. States degenerate at sphericity are observed to split with increasing quadrupole deformation, $|\beta_2|$, depending on the projection of their magnetic sub-states onto the deformation/symmetry axis, $K$ (or $\Omega$ if the orbit is only weakly coupled to the symmetry axis), shown in Figure 2.1. The quadrupole deformation parameter, $\beta_2$, is positive for prolate deformations and negative for oblate

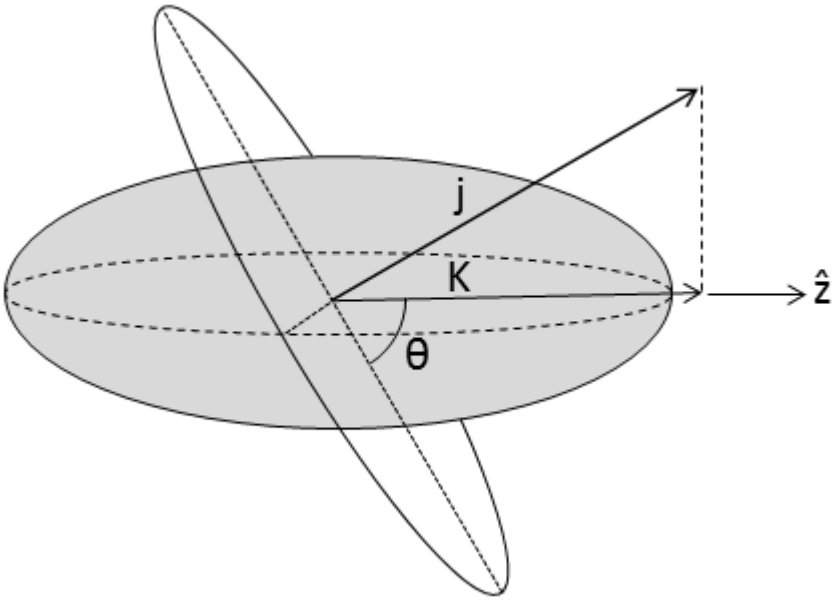


**Figure 2.1:** Projection of the angular momentum of a valence nucleon sub-state onto the deformation axis of a prolate nucleus.

deformations. The form of the $K$-splitting is dependent on the angle of their orbits with respect to the symmetry axis, $\theta$, which is classically given by $\sin^{-1}(j/K)$, with high $K$ orbits rising and lowering in energy for prolate and oblate deformations, respectively, due to their decreased or increased overlap with the core nucleons. An example of a Nilsson diagram is shown in Figure 2.2.

Nilsson orbitals are denoted by the asymptotic Nilsson quantum numbers, $K^{\pi}$ $[Nn_z\Lambda]$, where $\pi$ is the parity of the state, $N$ is the principal quantum number, $n_z$ is the number of nodes the wave-function of the state has along the symmetry axis and $\Lambda$ is the projection of the orbital angular momentum onto the symmetry axis (so that $K = \Lambda + \Sigma$, where $\Sigma$ is the projection of the intrinsic spin). The $n_z$ and $\Lambda$ components are related to $N$ (and therefore the parity of the state) such that $n_z + \Lambda$ is even if $N$ is even and odd if $N$ is odd.

State mixing can occur between states of similar $K^{\pi}$ and spin orientation. The degree of mixing is dependent on the $K$-values involved and the energy separation between the states. State mixing increases as energy separation decreases, however, as no two states with the same quantum number and parity can overlap, they instead

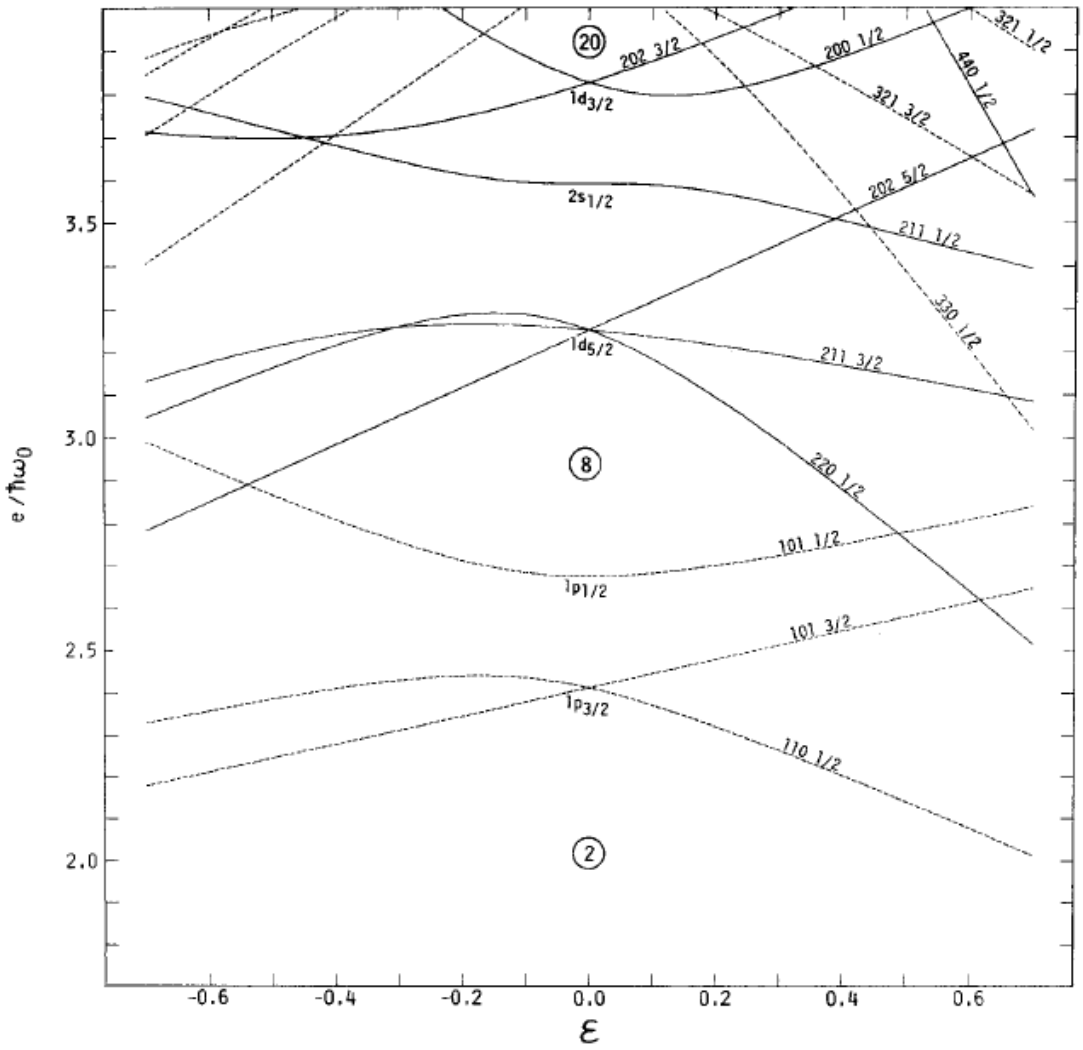


**Figure 2.2:** Nilsson diagram for A=25 nuclei as a function of the deformation parameter $\varepsilon$, where $\varepsilon \simeq 0.95\beta_2$. Positive and negative parity states are marked by solid and dotted lines, respectively, and spherical shell gaps are indicated [22].

form a 'pseudo-crossing'. The degree of mixing between the two states inverts at the inflection point, the states effectively swap principle wave-function components ($N$, $n_z$ and $\Lambda$) and exchange characteristics. Intruder states, that have had their energies shifted into a lower shell band by the spin-orbit interaction and are therefore surrounded by states of opposite parity, can exist unperturbed to large deformations.

The radius of a deformed nucleus can be calculated using the droplet model, which considers protons and neutrons separately and allows for the charge distribution and neutron skin thickness to be determined [23]. The matter radius can be

expressed as an expansion of spherical harmonics, $Y_{kq}(\theta)$:

$$R(\theta) = R(1 + \sum_{i\geq 2} \beta_i Y_{i0}(\theta))$$

where $\beta_i$ are multipole deformation parameters and $R$ is a normalisation factor that ensures the nuclear volume stays constant and therefore independent of $\beta_i$. The mean-square charge radius is then given by,

$$< r^2 > =< r^2 >_{sph} \left(1 + \frac{5}{4\pi} \sum_i < \beta_i^2 >\right) + 3\sigma^2 \tag{2.1}$$

where $< r^2 >_{sph}$ is the mean-squared charge radius for a spherical nucleus of equal volume. The $\sigma$ term is the surface diffusiveness and is considered constant along an isotope chain [23, 24].

The quadrupole deformation most often dominates and the shape expansion can itself be expressed in terms of static and dynamic contributions [25, 26]:

$$< \beta_2^2 > =< \beta_2 >^2 +(< \beta_2^2 > - < \beta_2 >^2) =< \beta_2^s >^2 + < \beta_2^d >^2 .$$

The static term gives a measure of the permanent deformation of the nucleus and the dynamic term gives a measure of the time-averaged fluctuations around this shape.

If the quadrupole term is assumed to exhaust the expansion in Equation 2.1, then the $< \beta_2^2 >$ term can be acquired from the change in nuclear mean-square charge radius:

$$\delta < r^2 > = \delta < r^2 >_{sph} + \frac{5}{4\pi} < r^2 >_{sph} \delta < \beta_2^2 > .$$

The change in mean-square charge radius can be extracted from isotope shifts (Section 2.3.3) and the spherical radius can be calculated from theory [23].

The term $< \beta_2^s >$ can be simultaneously determined from the intrinsic quadrupole

moment, evaluated from the electric quadrupole shift of the hyperfine structure (Section 2.3.2), using,

$$Q_0 = \frac{5}{\sqrt{5\pi}} Z < r^2 >_{sph} < \beta_2^s > (1 + 0.36 < \beta_2^s >).$$

While both prolate and oblate states exist in nuclei, experiments have shown that the ground states of the vast majority of medium-to-heavy deformed nuclei are prolate with oblate nuclear ground states appearing near shell closures. The dominance of the prolate deformation has been attributed to the Coulomb repulsion between protons favouring an elongated nucleus and the abundance of low-K Nilsson orbitals that become energetically favourable with greater prolate deformation (compared to the high-K orbitals favoured by oblate deformations) [21].

In this work regions where nuclei change between prolate and oblate deformations, and the shape coexistence that can occur in transitional regions, are of great interest. One such region, of particular interest, is around Z∼40, N∼60 where changes in mean-square charge radius and two-neutron separation energies indicate a sudden onset of a saturated deformation (at N=60). The magnitude of the shape change is greatest for yttrium (Z=39), reduces in magnitude in adjacent elements and is almost unobserved in molybdenum (Z=42) and krypton (Z=36), which instead show a steady increase in deformation [27]. In Chapter 6, measurements of the mean-square charge radius of molybdenum and yttrium are presented and theoretical predictions of deformations in the region are discussed.

## 2.2 Atomic theory

An atom consists of a central nucleus surrounded by an electron cloud. The periodicity in the properties of the elements, which gave rise to the Periodic Table, can be successfully described using the atomic shell model. The atomic shell model

describes electron states of an atom producing well-defined orbital shells, sub-shells and degenerate sub-states, and attributes the periodicity of the elements to the filling of these orbital shells [28].

Each unique state in the shell model can be described by a set of quantum numbers. The principal quantum number, $n$, is a positive integer number that describes the gross shell structure of the atom, with electrons in higher shells being less tightly bound than those in lower orbits. The principal quantum shells are then split into sub-shells which are described by their orbital angular-momentum, denoted by $\mathbf{l}$. The orbital angular momentum quantum number, $\mathbf{l}$, can take positive integer values, and zero, which are conventionally denoted by the letters s, p, d, f for $\mathbf{l} = 0, 1, 2, 3$ respectively with orbitals beyond $\mathbf{l} = 3$ progressing alphabetically (skipping 'j') [29]. These orbital sub-shells appear in those principal shells where $\mathbf{l} \leq n - 1$.

As well as their orbital angular momentum, each electron has an intrinsic spin of a half, denoted by $\mathbf{s}$. The relative strength of the coupling between the intrinsic spin and the orbital angular momentum of the orbiting electron, in comparison to the residual electrostatic interaction, determines whether the state of the atom is best described by LS-coupling or jj-coupling. This interaction involves the coupling of the magnetic moment created by the intrinsic spin of the electron and the magnetic field created by the moving electron cloud [28].

In low Z atoms the spin-orbit interaction is relatively weak and they can be described well by coupling the intrinsic spins and angular momenta of the electrons separately into total spin, $\mathbf{S}$, and total angular momentum, $\mathbf{L}$. These total spin and orbital values then couple to give the total angular momentum, $\mathbf{J}$:

$$\mathbf{J} = \mathbf{L} + \mathbf{S}$$

and is called LS-coupling (or Russell-Saunders coupling). In high Z or highly-charged

atoms, where the interaction is stronger, the intrinsic spin and angular momenta of the individual electrons couple to give each of them a total angular momentum, $\mathbf{j}$, which then couple together to give the total angular momentum, $\mathbf{J}$:

$$\mathbf{J} = \mathbf{j_1} + \mathbf{j_2} + ...$$

and is called jj-coupling (this coupling scheme is also applicable in the nuclear shell model).

The energy shift produced by the spin-orbit interaction, known as fine structure, is given by,

$$E_{FS} = -\boldsymbol{\mu}_\mathbf{s} \cdot \mathbf{B_J}$$

where $\boldsymbol{\mu}_\mathbf{s}$ is the magnetic dipole moment of the electron, and $\mathbf{B_J}$ is the magnetic field experienced by the electron due to its orbit. The magnetic dipole moment of the electron is defined as,

$$\boldsymbol{\mu}_\mathbf{s} = -g_s \mu_B \frac{\mathbf{s}}{\hbar}.$$

The orbital shells have degenerate sub-states that can have their degeneracy lifted according to their geometry, such as their projection onto a defined axis. For LS-coupling these states are represented by $m_l$, the magnetic quantum number, which ranges in integer steps between $-\mathbf{l}$ and $+\mathbf{l}$ (eg: $\mathbf{l} = 1 \rightarrow m_l = -1, 0, +1$). Each of these states can contain two electrons with opposite spin projections, denoted by the spin-projection quantum number, $m_s$, where $m_s = \pm\frac{1}{2}$. Thus each unique state can be described by the quantum numbers $n, l, m_l$ and $m_s$.

In jj-coupling the orbital shells are split into sub-shells according to their total angular momentum, $\mathbf{j}$, where the sub-shells are $\mathbf{j} = \mathbf{l} + \mathbf{s}$ and $\mathbf{j} = |\mathbf{l} - \mathbf{s}|$ (eg: a p-shell is split into the $\frac{1}{2}$ and $\frac{3}{2}$ sub-shells). The s-orbital is not split as it can only couple into a $\mathbf{j} = \frac{1}{2}$ state. These sub-shells have sub-states that are represented by

the magnetic quantum number, $m_j$, which can also be used to describe LS-coupled states. These sub-states range in integer steps between $-\mathbf{j}$ and $+\mathbf{j}$ similar to an LS-coupled shell. Thus each unique state can be described by the quantum numbers $n, l, j$ and $m_j$.

The simple, but extreme, shell model assumes that the properties of the atom are determined solely by the valence electrons surrounding an inert core. The total angular momentum of the atom is then given by the coupling of the angular momenta of each valence electron and is often described using the notation,

$$^{2S+1}L_J$$

where $2S + 1$ is the multiplicity, $L$ is the total orbital angular momentum of the atom and $J$ is the total angular momentum ($\mathbf{J} = \mathbf{L} + \mathbf{S}$).

The hyperfine structure splitting, described in Section 2.3, is typically three or four orders of magnitude smaller than fine structure, thus each state can be considered isolated and can be observed without interference from others ($2^{nd}$ order hyperfine splittings are considered negligible in this work).

## 2.3 First-order hyperfine structure and the isotope shift

The hyperfine structure (HFS) of an atomic state arises from the interaction of the nucleus with the atomic electron cloud and can be expanded in terms of electric and magnetic multipole moments of the nucleus, with odd electric and even magnetic terms vanishing due to symmetry arguments. The three dominating terms are the electric monopole term, giving rise to the gross structure and isotope shift, the magnetic dipole interaction and the electric quadrupole interaction.

### 2.3.1 Magnetic dipole moments and hyperfine anomalies

Usually the largest contribution to HFS comes from the interaction of the magnetic dipole moment of the nucleus, acquired from the multipole expansion of the vector potential [18],

$$A(r) = \frac{\mu_0}{4\pi} \int \frac{\mathbf{j_c}(\mathbf{r}')\, d\tau'}{\mid \mathbf{r} - \mathbf{r}' \mid} \tag{2.2}$$

with the magnetic field created by the electron cloud. In Equation 2.2 $\mathbf{r}$ is the position vector for the observation point, $\mathbf{r}'$ is a vector in the current distribution, $\mathbf{j_c}(\mathbf{r}')$, and $\tau$ represents the volume of the nucleus. The first non-vanishing term in the series expansion of this integral, when expanded in terms of Legendre polynomials, gives the magnetic dipole moment.

The interaction of the nuclear magnetic dipole moment with the magnetic field arising from the motion of the electron cloud is similar to fine structure (Section 2.2). The energy shift produced by this interaction is given by,

$$E_{M1} = -\boldsymbol{\mu}_\mathbf{I} \cdot \mathbf{B_J}$$

where $E_{M1}$ is the energy shift, the $\boldsymbol{\mu}_\mathbf{I}$ term is the magnetic dipole moment of the nucleus and $\mathbf{B_J}$ is the magnetic field from the electron cloud orbital motion.

The dipole moment of the nucleus is proportional to its spin, $\mathbf{I}$, and the magnetic field produced by the electron cloud is proportional to the total electronic angular momentum, $\mathbf{J}$, therefore the energy perturbation can be expressed in terms of the total nuclear and atomic angular momenta:

$$E_{M1} = A\, \mathbf{I} \cdot \mathbf{J} \tag{2.3}$$

where $A$ is the hyperfine dipole coefficient and is defined as [30],

$$A = \frac{g_I \mu_N B_J}{\sqrt{J(J+1)}}. \tag{2.4}$$

It follows from Equation 2.3 that if either $I$ or $J$ is zero then no magnetic HFS splitting is observed. In Equation 2.4 the $g_I$ term is the g-factor and $\mu_N$ is the nuclear magneton.

A simple relationship for the expectation value of $\mathbf{I}\cdot\mathbf{J}$, in terms of good quantum numbers, can be obtained by squaring the total angular momentum of the atom ($\mathbf{F} = \mathbf{I} + \mathbf{J}$), to give,

$$< \mathbf{F^2} > =< \mathbf{I^2} > + < \mathbf{J^2} > +2 < \mathbf{I}\cdot\mathbf{J} > .$$

After expanding the quantum terms, this becomes,

$$\begin{aligned} E_{M1} &= \frac{A}{2}(F(F+1) - I(I+1) - J(J+1)) \\ &= \frac{A}{2}C \end{aligned} \tag{2.5}$$

which can be used to calculate the energy shifts for each individual $F$ state (where $|I-J| < F < I+J$ in integer steps).

Each set of HFS multiplets has a different value for the dipole coefficient, $A$, and the number of levels within a multiplet is $2I+1$ if $I < J$ or $2J+1$ if $J < I$. In multiplets produced only by the magnetic dipole moment the separation between states can be calculated using the Landé interval rule [30]:

$$E_F - E_{F-1} = AF.$$

As $B_{1/2} \propto |\psi(0)|^2$, large magnetic splittings are found in states with wavefunctions that have high probability densities at the nucleus, such as those in unpaired s-orbitals.

Theoretically, measuring the hyperfine dipole coefficient, $A$, would mean one

could calculate the magnetic dipole moment, $\mu_I$. However this would assume precise knowledge of the magnetic field caused by the electrons, $B_J$. The electronic magnetic field may be calculated accurately for low Z elements where there are few valence electrons, but the problem becomes rapidly more complex for larger, multi-electron systems. Taking ratios between isotopes removes the need to know $B_J$ (under the assumption it stays constant across the isotope chain), therefore, as long as the magnetic dipole moment of one of the isotopes is known, the dipole moments of the entire isotope chain can be determined. This simple relationship is given by [18],

$$\frac{A_1}{A_2} = \frac{(\mu_I/I)_1}{(\mu_I/I)_2} \tag{2.6}$$

where the subscripts identify the different isotopes [31].

Equation 2.6 assumes the uniform distribution of magnetisation in the nucleus, which is not the case. The finite size of the nucleus results in changes in the nuclear radius, the distribution of the magnetisation and in changes in the electron wavefunction across the nuclear volume between isotopes, therefore causing so called hyperfine anomalies in experimental calculations [32]. These are usually $< 1\%$ but can reach a few percent in some cases. Hyperfine anomalies can arise from two components, given by,

$$A_{finite} = (1 + \epsilon_{BCRS})(1 + \epsilon_{BW})A_{point} \tag{2.7}$$

and are a modification of the dipole constant for a point nucleus [33]:

$$A_{point} = \frac{16\pi}{3}\frac{\mu_0}{4\pi h} g_I \mu_N \mu_B \mid \psi(0) \mid^2 f_R. \tag{2.8}$$

In Equation 2.8 the $\psi(0)$ is the electronic wavefunction at the nucleus, $\mu_B$ is the Bohr magneton and $f_R$ is a relativistic enhancement [34]. The $\epsilon_{BCRS}$ (Breit-Crawford-Rosenthal-Schawlow) anomaly is due to the change in electric potential close to the nucleus due to the change in its radius. The $\epsilon_{BW}$ (Bohr-Weisskopf)

[32] anomaly is due to the change in the distribution of the magnetisation in the nucleus and only affects s-orbitals as other orbital wave-functions vanish at the nucleus (except for in heavy atoms where relativistic effects make the $p_{1/2}$ orbital wavefunctions non-vanishing at the nucleus). The terms in Equation 2.7 can be combined and applied to Equation 2.6 to produce,

$$\frac{A_1}{A_2}(1+\Delta^{1,2}) = \frac{(\mu_I/I)_1}{(\mu_I/I)_2}$$

where $\Delta^{1,2}$ is the combination of the shifts in both anomalies between the isotopes.

### 2.3.2 Electric quadrupole moments

The electric quadrupole interaction is the second-order term of the electric multipole expansion and represents the degree of quadrupole deformation, $Q$, of the nucleus. The nucleus is spherical if $Q = 0$, prolate if $Q > 0$ and oblate if $Q < 0$. The energy shift of the quadrupole interaction is given by,

$$E_{E2} = \frac{1}{4}eQ\overline{\left(\frac{\delta^2 V(0)}{\delta z^2}\right)}\left(\frac{3}{2}\cos^2\theta - \frac{1}{2}\right) \tag{2.9}$$

where $V(0)$ is the electric potential at the nucleus due to the electron cloud and $\theta$ is the angle between the axis of symmetry of the electronic potential and the nucleus. The magnitude of the quadrupole term can become comparable to the dipole term in heavily deformed nuclei.

The relationship between the electric quadrupole in the laboratory frame, $Q$, and in the intrinsic frame of the nucleus, $Q_0$, in terms of the nuclear angular momentum, $I$, and its projection onto the nuclear symmetry axis, $K$, is given by,

$$Q = Q_0\frac{3K^2 - I(I+1)}{(I+1)(2I+3)}$$

where $K = I$ is the 'stretched' case. This assumes the deformation of the nucleus is axially symmetric and that the nuclear spin is coupled to the deformation axis.

The calculation of the intrinsic quadrupole moment is given by,

$$eQ_0 = \int_\tau (3z^2 - r^2)\rho(r)\, d\tau$$

where $z$ is taken as the axis of symmetry.

Expressing the angular part of Equation 2.9 in terms of angular momentum quantum numbers gives [35],

$$E_{E2} = B\left(\frac{\frac{3}{16}C(C+1) - \frac{1}{4}I(I+1)J(J+1)}{I(I-\frac{1}{2})J(J-\frac{1}{2})}\right)$$

where,

$$B = eQ\left(\frac{\delta^2 V(0)}{\delta z^2}\right).$$

If $I, J < 1$ then the hyperfine quadrupole constant, $B$, is zero (spherical symmetry). In theory one could again calculate the quadrupole moment, $Q$, if $B$ was known, however this would require detailed knowledge of the electronic potential. Thus, similar to the hyperfine dipole constants, the ratio of the hyperfine quadrupole constants is used instead. This assumes that $V(0)$ is constant across an isotope chain and gives the simple relationship:

$$\frac{B_1}{B_2} = \frac{Q_1}{Q_2}$$

where the subscripts indicate the different isotopes.

### 2.3.3 Optical isotope shift

The optical isotope shift is the difference between the centroids of a transition line in different isotopes and is defined as,

$$\delta\nu_i^{A,A'} = \nu_i^{A'} - \nu_i^{A}$$

where $\nu$ is the frequency of the transition, $A$ and $A'$ are the mass numbers of the two isotopes and the subscript denotes the transition line.

There are two contributions to the isotope shift; the mass shift (MS) and the field shift (FS). The mass shift dominates in lighter atoms and the field shift in heavier atoms. The mass shift further divides into two components; the normal mass shift (NMS) and the specific mass shift (SMS). The total isotope shift is the sum of these three terms [36],

$$\delta\nu_i^{A,A'} = \delta\nu_{NMS,i}^{A,A'} + \delta\nu_{SMS,i}^{A,A'} + \delta\nu_{FS,i}^{A,A'}.$$

The mass shift is due to the change in reduced mass of the nucleus and from the different recoils it has with the electron momenta. The frequency shift due to the NMS is defined as,

$$\delta\nu_{NMS,i}^{M,M'} = \frac{m_e(M'-M)}{M(M'+m_e)}\nu_i$$

where $m_e$ is the electron mass, the $M$ terms are the nuclear masses with $M' > M$ and $\nu_i$ is the frequency of the transition in the lighter nucleus. This is often approximated and simplified to,

$$\begin{aligned}\delta\nu_{NMS,i}^{A,A'} &= \frac{m_e\nu_i}{m_N}\frac{(A'-A)}{AA'} \\ &= N_i\frac{A'-A}{AA'}\end{aligned}$$

which gives the NMS in terms of the nuclear mass numbers and the normal mass shift constant, $N_i$.

The specific mass shift is due to the correlated motion of the electrons and can be derived from the expansion of the nuclear kinetic energy in terms of the orbiting electron momenta. This is done using the relation $\mathbf{p_N} = -\sum_m \mathbf{p_m}$, where $\mathbf{p_N}$ is the momentum of the nucleus and $\mathbf{p_m}$ is the momentum of the $m$-th electron:

$$\begin{aligned}\mathcal{H}_{kinetic} &= \frac{\mathbf{p_N}^2}{2M} + \frac{1}{2m_e}\sum_m \mathbf{p_m}^2 \\ &= \frac{1}{2M}\left(\sum_m \mathbf{p_m}^2 + \sum_{m\neq n} \mathbf{p_m}\cdot\mathbf{p_n}\right) + \frac{1}{2m_e}\sum_m \mathbf{p_m}^2.\end{aligned}$$

The shift in frequency due to the SMS is then,

$$\begin{aligned}\delta\nu^{A,A'}_{SMS,i} &= \frac{(A'-A)}{AA'}\frac{1}{m_N}\sum_{m>n}\mathbf{p_m}\cdot\mathbf{p_n} \\ &= S_i\frac{A'-A}{AA'}\end{aligned}$$

where the sum over $\mathbf{p_m}\cdot\mathbf{p_n}$ is the mass polarisation parameter and $S_i$ is the specific mass shift constant.

The field shift is due to the change in nuclear charge distribution and is given by,

$$\delta\nu^{A,A'}_{FS,i} = F_i\lambda^{A,A'}$$

where $\lambda$ is the expansion of the nuclear radius in terms of radial multipole moments and $F$ is the electronic factor. The expansion of the $\lambda$ term is,

$$\lambda^{A,A'} = \delta < r^2 >^{A,A'} + \frac{C_2}{C_1}\delta < r^4 >^{A,A'} + \frac{C_3}{C_1}\delta < r^6 >^{A,A'} + ...$$

where the $C_k$ values are constant and have been tabulated for a range of nuclei [37]. For low-Z nuclei the $\lambda$ term is typically equal to the change in mean-square charge radius, $\delta < r^2 >^{A,A'}$, within a few percent, as the electronic wave-functions are approximately constant across the nucleus (and therefore higher order multipoles vanish). The electronic factor is defined as,

$$F_i = \pi a_0^3\ \Delta\psi(0)_i^2\ f(Z)$$

where $\Delta\psi(0)_i^2$ is the change in electron charge density at a point nucleus and $f(Z)$

is the form factor that accounts for relativistic corrections and corrects for the finite size of the nucleus [34, 38].

The total isotope shift is thus,

$$\begin{aligned}\delta\nu_i^{A,A'} &= (N_i + S_i)\frac{A' - A}{AA'} + F_i\delta < r^2 >^{A,A'} \\ &= M_i\frac{A' - A}{AA'} + F_i\delta < r^2 >^{A,A'} \end{aligned} \tag{2.10}$$

and shows that by measuring the mass shift factor, $M_i$, and electronic factor, $F_i$, it is possible to calculate the change in nuclear mean-squared charge radius [24].

#### 2.3.3.1 King plot

If the isotope shift for two transition lines in at least three isotope pairs are measured then they can be plotted against each other in a so-called King plot [39]. The slope and intercept of the straight line ($y = mx + c$) produced in the King plot gives a relationship between the electronic factors, $F_{x,y}$, and mass shift factors, $M_{x,y}$, of the two transitions plotted. The slope, $m_{King}$, is defined as,

$$m_{King} = F_y/F_x$$

and gives the ratio between the electronic factors. The intercept, $c_{King}$, is defined as,

$$c_{King} = M_y - \frac{F_y}{F_x}M_x$$

and gives the difference between the mass factors (with one mass factor multiplied by $m_{King}$).

If the change in mean-squared charge radius has been measured (from other experiments such as electron scattering and electronic/muonic X-rays) for at least three isotope pairs then a modified King plot can be used to calibrate the electronic factor and mass shift factor for a single transition line. A modified King plot is

made by multiplying the isotope shift (Equation 2.10) by $\mu$, which is defined as,

$$\mu = \frac{A'A}{(A' - A)}$$

where $A$ and $A'$ are precise mass measurements. The isotope shift can thus be plotted in a linear form:

$$\begin{aligned} \mu\delta\nu_i^{A,A'} = \delta\nu_{mod,i}^{A,A'} &= F_i\mu\delta < r^2 >^{A,A'} + M_i \\ &= F_i\delta < r^2 >_{mod,i}^{A,A'} + M_i \end{aligned}$$

where $\delta\nu_{mod,i}^{A,A'}$ is plotted on the y-axis and $\delta < r^2 >_{mod,i}^{A,A'}$ is plotted on the x-axis. The slope of the modified King plot gives the electronic factor for the transition and the intercept gives the mass shift factor. The electronic and mass shift factors can then be used to calculate the change in mean-square charge radius from isotope shifts of the same transition in other isotopes in the isotope chain.

The modified isotope shift equation is often divided by a constant reference pair of isotopes, $\mu_{\text{ref}}$, to provide modified mean-square charge radii and isotope shifts on a scale with the mass shift for easier analysis.

## 2.4 Lasers

A laser may be constructed by creating a cavity in which a light beam repeatedly passes through a gain medium and is amplified by stimulated emission. The emitted photons have the same wavelength, phase and direction as the ones that stimulated their production, thus a coherent monochrome beam propagates in the cavity. Stimulated absorption and emission have the same probability of occurring and therefore a population inversion towards the upper state is required if there is to be any gain. This population inversion can be achieved in the solid state by an electric current creating electron-hole pairs over a band-gap and their recombination results in the

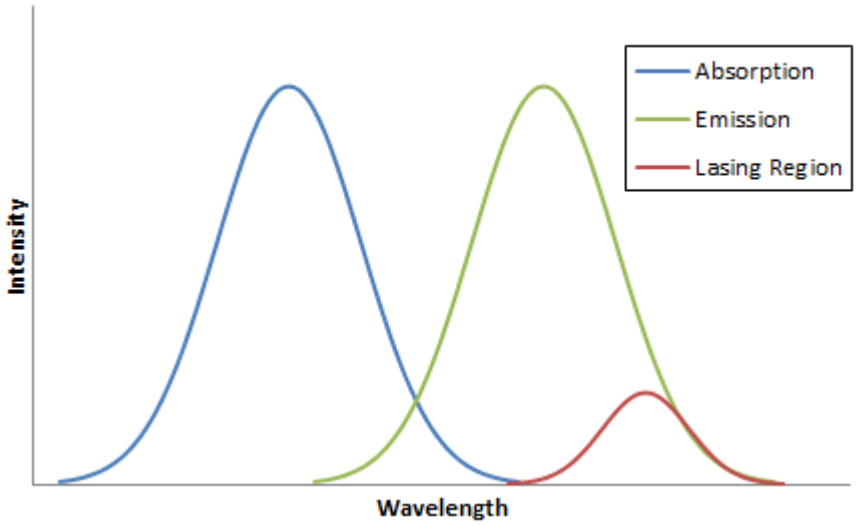


**Figure 2.3:** Absorption and emission requirements for lasing to occur.

release of photons. Alternatively optical pumping, where the population inversion is achieved by exciting the gain medium with photons (from potentially another laser), may be used. In the case of the dye laser, the dye molecules are excited into an upper ro-vibrational band, decay non-radiatively to the band-head before decaying via photon emission to the ground state excited ro-vibrational band. The molecules then decay non-radiatively back to the ground state band-head and may be re-excited. The emitted photon has less energy than that needed to excite the molecule from the ground state and thus is able to lase as the stimulated emissions are not re-absorbed into the gain medium. Figure 2.3 illustrates this requirement of different wavelengths for lasing to occur.

### 2.4.1 Frequency stabilised dye laser

A typical dye laser set-up is illustrated in Figure 2.4.

The dye (Rhodamine 6G in this work) is optically pumped with a solid-state laser (CW Nd:YAG laser, frequency doubled to 532 nm with up to 5 W power available at the IGISOL facility). The circulating dye jet pressure ($\sim$ 85 psi) is selected to prevent saturation of the dye and to achieve laminar flow to prevent surface

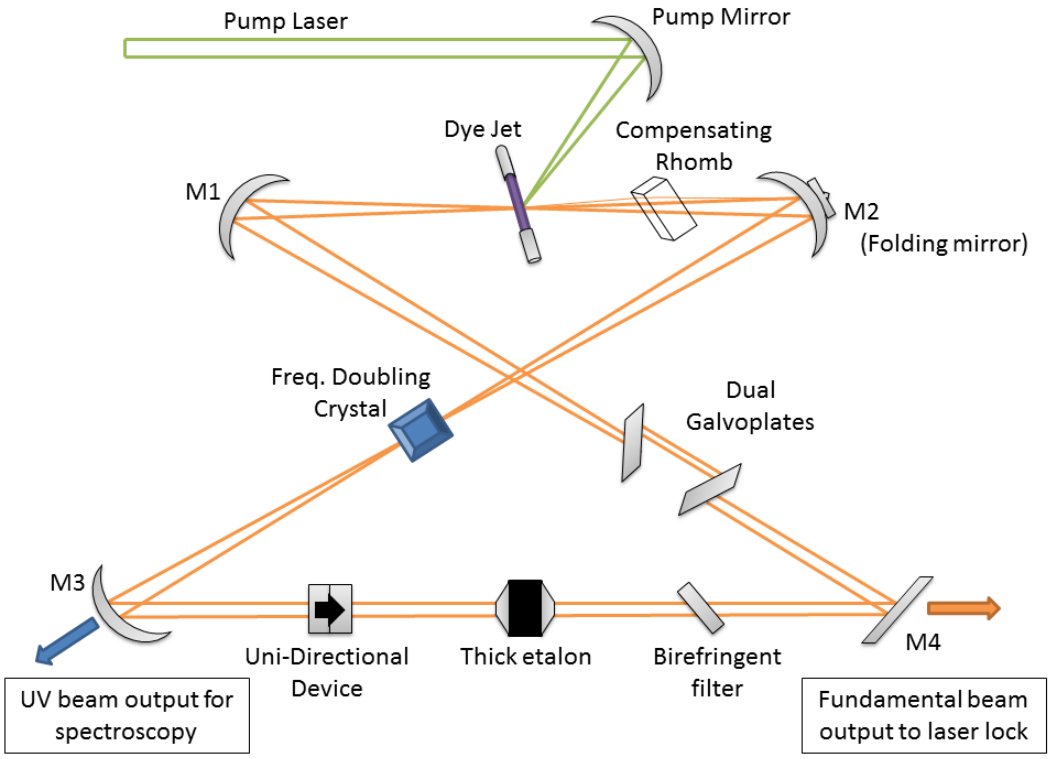


**Figure 2.4:** Dye laser setup.

distortion effects. A compensating rhomb is placed after the dye jet to correct for astigmatism aberrations. The birefringent filter and thick etalon are used to acquire a single-mode beam and the unidirectional device prevents the laser propagating in both directions. The dual galvoplates are used to change the cavity length, therefore altering the available modes of operation. The fundamental beam output goes to a laser lock to keep the light at a specific frequency (Section 3.1.1) and a frequency doubling crystal ($\beta$-barium borate (BBO)) creates vertically polarised UV light that passes through the dichroic M3 mirror window for use in the experiment.

#### 2.4.1.1 Fundamental beam

The number of available modes in the laser cavity is determined by the path length of the cavity, $L$. The available modes are given by,

$$\nu(n) = n\frac{c}{L}$$

where $n$ is an integer and the boundary $n = 1$ is where the wavelength of the laser beam equals the path length of the cavity ($\lambda(n) = \frac{c}{\nu(n)} = \frac{L}{n}$). For the 380 ring dye laser used at the IGISOL facility this gives a spacing between the modes of $\sim$ 230 MHz.

Each component is positioned at Brewster's angle for horizontally polarised light to prevent losses in the fundamental beam at each reflection and inhibiting the transmission of other polarisations within the laser cavity. The birefringent filter is used as a coarse tuner for the laser mode and consists of three quartz plates that rotate the plane of polarisation of light that passes through them. The light passing through the filter is polarised differently according to its frequency and those frequencies polarised by non-integers of $\pi$ will suffer losses at each Brewster surface, thus reducing the range of allowed modes ($\sim$0.5 nm transmission range). The unidirectional device consists of a Faraday rotator and an optically-active quartz plate. The quartz plate polarises light depending on the direction of propagation, while the Faraday rotator polarises independently of direction. The combination of the two result in light traveling in the desired direction leaving the rotator unaltered, whilst light traveling in the opposite direction leaves with a rotated plane of polarisation and suffers losses at each Brewster surface.

The thick etalon is used to select the cavity mode at which the laser operates and consists of two reflecting surfaces separated by an air gap. The two surfaces are connected by a piezoelectric material that is used to tune the size of the gap. The thick etalon restricts the cavity modes to those that constructively interfere with themselves upon reflection inside the etalon, with the mode that suffers the least amount of losses from the birefringent filter dominating in the laser cavity. The thick etalon has a free spectral range of 75 GHz, giving $\sim$0.1 nm separation between transmission peaks in the optical region. The dual galvoplates are used to change the path length of the cavity. This is achieved by altering the angles

of the galvoplates, with respect to the beam axis, and therefore changing the path length the beam takes through them. The thick etalon and dual galvoplates are synchronized to avoid mode hops during tuning.

#### 2.4.1.2 Frequency doubling

The frequency doubling crystal allows the range of the high resolution, tunable dye laser to extend into the UV region. The creation of UV light in the frequency-doubling crystal is due to the non-linear response of the (uniaxial, birefringent) crystal with the electric field of the incident light, as shown by,

$$\mathbf{P} = \epsilon_0(\chi_1\mathbf{E} + \chi_2\mathbf{E}^2 + \chi_3\mathbf{E}^3 + ...)$$

where $\chi_n$ is the electric susceptibility [40].

The second-order term can be expanded for two incident electric fields ($\mathbf{E} = \mathbf{E_1}\sin(\omega_1 t) + \mathbf{E_2}\sin(\omega_2 t)$) into,

$$\begin{aligned}\mathbf{P_2} =& \epsilon_0\chi_2\Bigg[\frac{1}{2}\mathbf{E_1^2}(1-\cos(2\omega_1 t)) + \frac{1}{2}\mathbf{E_2^2}(1-\cos(2\omega_2 t)) \\ &+ \mathbf{E_1}\cdot\mathbf{E_2}(\cos((\omega_1-\omega_2)t) - \cos((\omega_1+\omega_2)t))\Bigg]\end{aligned}$$

which shows the direct and alternating current generated by the individual electric fields as well as oscillations at the difference and sum of the two fields. The sum and difference terms give rise to frequency mixing in the crystal and, in the special case of both photons originating from the same laser source, simplifies the second order term into,

$$\mathbf{P_2} = 2\epsilon_0\chi_2\mathbf{E^2}(1-\cos(2\omega t)).$$

This second-harmonic generation (SHG) results in the creation of a photon at double the frequency. The incident beam continues through the non-linear crystal as the ordinary ray, while the frequency-doubled photons propagate as the extraordinary

ray.

To ensure the UV photons are in phase with each other upon creation, and therefore interfere constructively, it is essential for the refractive index of the crystal to be the same for both the ordinary and extraordinary rays so that they both propagate through the crystal at the same speed. This requires the incident beam to be tuned to the correct angle with respect to the optical axis of the birefringent crystal.

# CHAPTER 3

# Experimental techniques

Between 2010 and 2012, the IGISOL (Ion Guide Isotope Separator On-Line) was dismantled, moved and reconstructed at a new laboratory. The new facility has several upgrades including a dedicated cyclotron, an extensive high-voltage (low energy) region and an electrostatic ion trap. The new facility is referred to as IGISOL 4; the previous set-up was IGISOL 3. The layouts of the IGISOL 3 and 4 are compared in Figures 3.1 and 3.2 respectively.

Radioactive ions are produced at the IGISOL facility in nuclear reactions induced by impinging a primary proton/deuteron beam from a cyclotron (Section 3.2) onto a target placed inside a gas-filled ion guide, itself housed within the IGISOL target chamber (Section 3.3). The new laboratory has a dedicated MCC30/15 cyclotron, which will provide 6000+ hours of run time per annum once optimised, and is still capable of receiving beams from the K130 cyclotron used by IGISOL 3. Stable ion beams can also be produced using cathode sputtering, either using the new stable isotope production facility or by an ion-discharge struck inside the IGISOL target chamber (the technique used at IGISOL 3, Section 3.4). A two-stage SextuPole Ion Guide ("double-SPIG") is used to extract ions from the IGISOL and separate them from buffer gas and neutral background before acceleration to 30 keV (Section 3.5). Extracted ions are then mass separated in a dipole magnet and injected into the Cooler-Buncher, before being released into a high-voltage (low energy) region (Sec-


**Figure 3.1:** Diagram illustrating the set-up of the IGISOL 3 beam-line: (1) target chamber and ion guide, (2) K130 cyclotron beam-line, (3) beam dump, (4) extraction and acceleration chambers, (5) dipole magnet, (6) beam switchyard, (7) RFQ trap (Cooler-Buncher), (8) JYFLTRAP, (9) quadrupole deflector, (10) electrostatic deflector to $1^{st}$ floor laser spectroscopy set-up, (11) beam-lines for experimental setups [41].

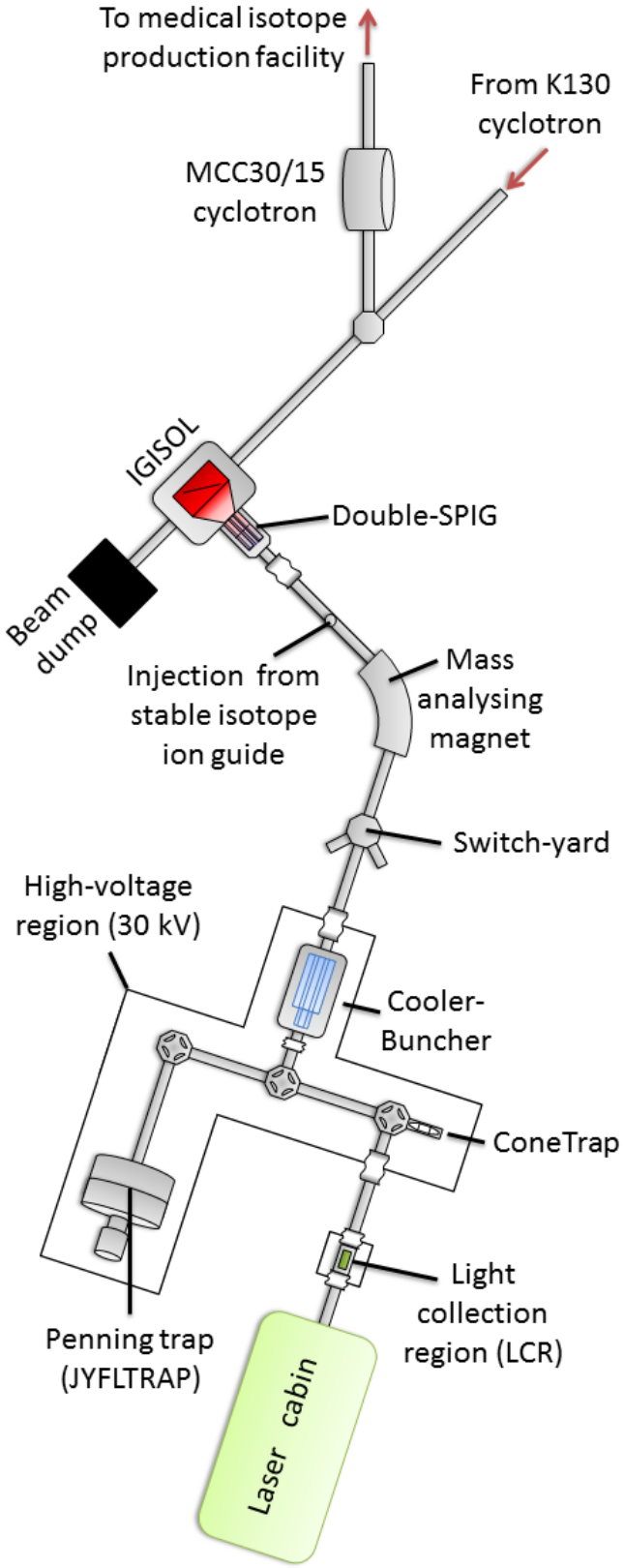


**Figure 3.2:** Layout of the IGISOL 4 facility.

tion 3.6). The ion ensembles are then transported towards either the light-collection region for spectroscopy (Section 3.7) or the JYFLTRAP for mass measurements.

This chapter discusses the operation of the facility and the improvements made from IGISOL 3 to 4, focusing on a line dedicated to collinear laser spectroscopy.

## 3.1 Collinear laser spectroscopy

One of the two main branches of the IGISOL facility uses collinear laser spectroscopy to measure the hyperfine structure of atomic transitions. Measurements of the hyperfine structure (the peak positions and relative intensities) may be used to determine the intrinsic spin, I, magnetic dipole moment, $\mu$, and electric quadrupole moment, Q, of the nucleus. The shift in atomic transition frequency between isotopes is referred to as the isotope shift and is used to determine changes in mean-squared charge radius between the nuclei (as presented in Chapter 2).

"Standard" collinear laser spectroscopy involves the overlap of a fast ion beam with a co- or counter-propagating laser beam and the detection of the resultant fluorescent photons to determine resonant frequencies [5]. The ions are accelerated to reduce their velocity spread, as shown by,

$$\begin{aligned} v &= \sqrt{\frac{2E}{m}} \\ \delta v &= \frac{1}{\sqrt{2mE}}\delta E \end{aligned} \tag{3.1}$$

and illustrated in Figure 3.3, therefore reducing the Doppler broadening of their spectral lines and making them comparable to their natural line widths, thus making it possible to observe the individual components of the hyperfine structure with a suitable laser light source. Equation 3.1 shows how the velocity spread, $\delta v$, changes with kinetic energy, $E$, where $m$ is the ion mass.

Currently the IGISOL uses a single-mode dye laser, locked to a chosen frequency

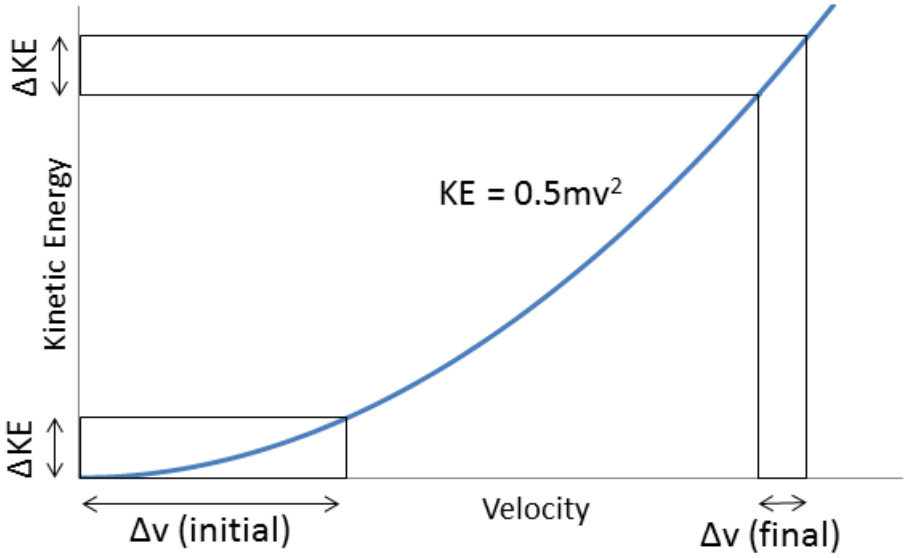


**Figure 3.3:** Graph showing the reduction in velocity spread as kinetic energy is increased.

(see Section 3.1.1). The required acceleration voltage has been reduced since the installation of the Cooler-Buncher (Section 4.1.1) due to the smaller energy spread of the cooled ions.

### 3.1.1 Laser frequency stabilisation

Laser stabilisation is achieved using a combination of a reference etalon, a slave etalon and an iodine absorption reference to lock the laser at a specific wavelength. Figure 3.4 shows the zero-crossing locking technique used by a reference etalon compensating for fast fluctuations in the laser frequency, due to thermal and sonic vibrations, and slave etalon compensating for cavity mode hops . The laser is locked to the side of these transmission peaks and changes in observed transmission/voltage are then used to drive the laser frequency back to the required value. The fast frequency compensation is achieved by moving the piezo-mounted M2 mirror, thus readjusting the cavity phase length, and the slow compensation is achieved by adjusting the thick etalon and dual galvoplates. The thick etalon and dual galvoplates are both used and synchronised for slow compensation of the laser frequency to track

the mode of the laser with the transmission maximum of the etalon. The reference and slave etalon make up the "Stabilok$^{TM}$" system, which itself is locked to an iodine reference.

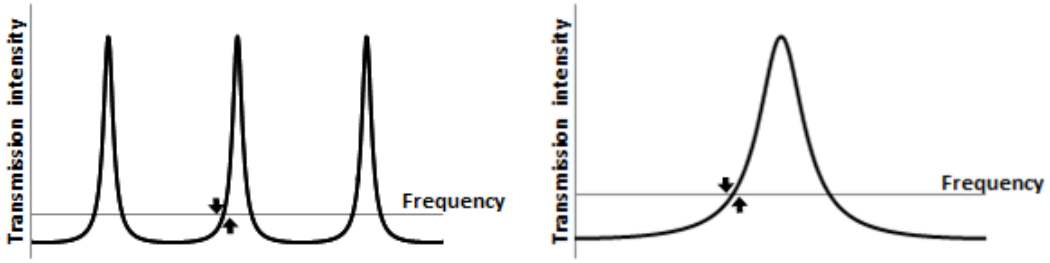


(a) Fast compensation from reference etalon, with a free-spectral-range of 500 MHz.

(b) Slow compensation from slave etalon, with a free-spectral range of ~8 GHz.

**Figure 3.4:** Fast and slow compensation provided by the reference and slave etalons.

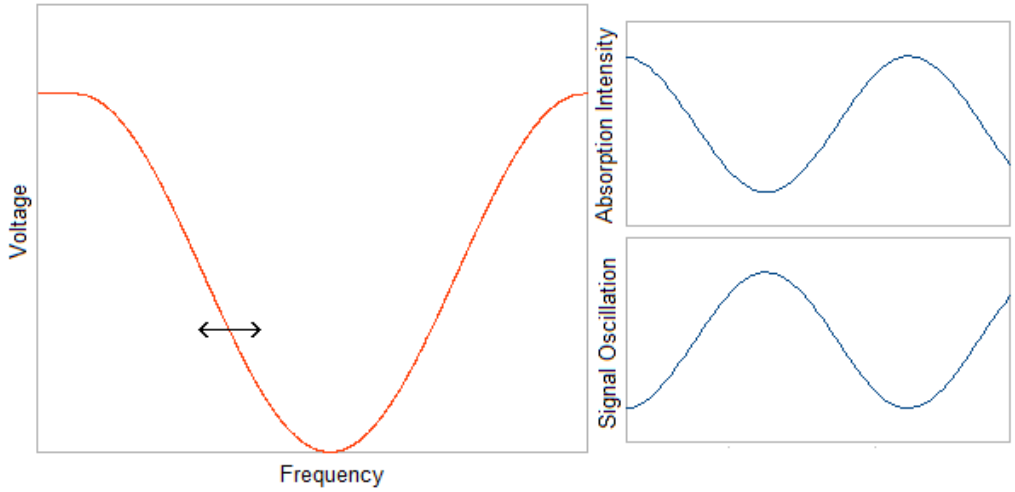


**Figure 3.5:** Figure illustrating the iodine absorption reference and the oscillation of the reference signal around the $I_2$ ro-vibrational absorption peak. The Figure shows the change in phase between the signal dither and the absorption intensity that is used to determine the direction of any drift compensation (in a phase-locked loop).

The iodine reference is used to compensate for any departure in absolute frequency due to changes in temperature affecting the etalons. The reference point lies at the bottom of an iodine absorption peak (ro-vibrational states) and the laser frequency is intentionally dithered to create oscillations in the absorption of the iodine. It is the change in phase between the laser oscillations and the change in absorption

intensity that indicates the direction of divergence (Figure 3.5). The iodine reference is used for its ability to provide an absolute reference point and because the iodine molecule has a wide range of precisely known ro-vibrational absorption resonances. The laser lock maintains the laser frequency to within $\sim 2$ MHz ($< 1$ in $10^9$).

## 3.2 Primary ion beams

The primary beam is supplied by one of two cyclotrons, the K130 or the MCC30/15. The K130 cyclotron can accelerate ions up to 130 $q^2/A$ MeV and the MCC30/15 can accelerate protons and deuterons up to 30 MeV and 15 MeV respectively.

A cyclotron [18] consists of a cylindrical chamber split into two D-shaped electrodes connected to an alternating voltage combined with a magnetic field normal to the plane of the cylindrical chamber. Ions are injected near the center of the cylinder and the magnetic field causes them to move in an orbital motion. The frequency of the alternating voltage of the D-electrodes matches the cyclotron frequency of the ions so that the ions are accelerated as they pass between them. The faster ions have a larger orbital radius, thus the combination of the magnetic field and the D-electrode accelerations result in the ions spiraling outwards from the centre of the cyclotron. The ions are then extracted at the outer edge of the cyclotron. A fixed-frequency cyclotron is illustrated in Figure 3.6 and the cyclotron frequency is given by,

$$f = \frac{qB}{2\pi m} \tag{3.2}$$

where $f$ is the cyclotron frequency, $q$ and $m$ are the ions' charge and mass respectively, and $B$ is the magnetic field strength perpendicular to the ion motion.

Both the MCC30/15 and K130 cyclotron can accelerate negative hydrogen and deuteron ions ($H^-$ and $D^-$). The negative ions are passed through a thin car-

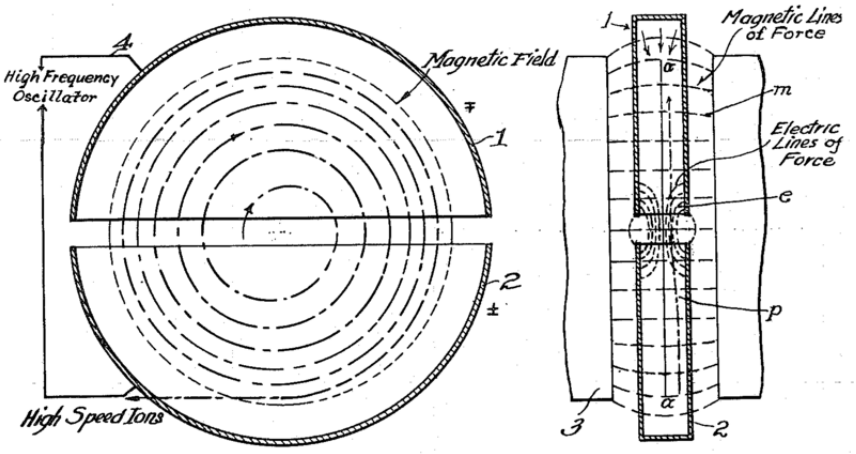


**Figure 3.6:** Diagram of a cyclotron: (1 and 2) D-shaped electrodes, referred to as "Dee's", in opposite phase, (3) magnet, (4) alternating voltage circuit to change Dee potentials. [42]

bon stripper foil at extraction from the cyclotron and converted to singly-charged, positive ions before being transported towards the IGISOL target chamber. The stripping of the $H^-$ and $D^-$ ions facilitates their extraction as they are repelled from the cyclotron, resulting in an increase in efficiency in comparison to when positive ions were used ($\sim 100\%$ compared to $\sim 50 - 70\%$). Using negative ions also avoids activation of the cyclotron from lost protons; less activation means less cool down time before maintenance of the cyclotron can take place.

### 3.2.1 Negative ion sources

The negative ions are created using multi-cusp ion sources. This is the LIISA ($H^-$ Light Ion Source) for the K130 cyclotron and a conventional filament-driven multi-cusp ion source that was delivered with the MCC30/15 cyclotron. These ion sources operate by providing free electrons from a filament discharge or RF-discharge source. These electrons (and the plasma they produce) are axially confined by the multi-cusp magnet assembly and accelerated away from the discharge source by a potential gradient. The now fast electrons collide with molecules of hydrogen in the hydrogen gas pumped into the chamber, thereby exciting them into a vibrational state:

$$e(E > 10eV) + H_2(\upsilon) \rightarrow H_2(\omega) + e.$$

Slow electrons attach to the excited hydrogen molecules and cause them to dissociate, resulting in a negative and a neutral hydrogen atom [43]:

$$e(E < 2eV) + H_2(\omega) \rightarrow H^- + H.$$

The conventional multi-cusp source delivered with the MCC30/15 cyclotron can provide 1 mA of $H^-$ for $\sim$ 130 hours and it takes around 12 hours to replace the filament due to the cyclotron cool-down time. For this reason an alternative negative ion source is currently in production for the MCC30/15; a CW 13.56 MHz Radio-frequency Ion Source (RADIS). The RADIS is aimed to provide at least 1 mA of CW $H^-$ and 500 $\mu$A of CW $D^-$ beams at the cyclotron injection energy of 25 keV, with a minimum maintenance interval of one month [44].

### 3.2.2 MCC30/15 cyclotron

The MCC30/15 cyclotron is designed to provide up to 100 $\mu$A of 18-30 MeV protons and 50 $\mu$A of 9-15 MeV deuterons (although recent tests of the cyclotron have provided currents of 200 $\mu$A of protons and 60 $\mu$A of deuterons [16]). This level of current is too large for direct use at the IGISOL. The high-current cyclotron beam can, however, be impinged on a neutron converter to produce a neutron beam.

#### 3.2.2.1 Neutron converter

A neutron converter is currently being designed for the IGISOL [45]. The neutron beam acquired using the converter can be used for neutron-induced fission. A colder fission can be achieved using a neutron beam rather than a proton beam as protons require extra energy to overcome the Coulomb barrier. The advantage of colder fissions is that their products have less energy for neutron evaporation and thus

provide greater yields of neutron rich isotopes. Using a neutron beam will allow further exploration of the neutron rich side of the chart of nuclides [46].

### 3.2.3 K130 cyclotron

The K130 cyclotron has access to a negative light ion source (LIISA) and two electron cyclotron resonance ion sources (6.4 GHz and 14 GHz ECRIS) for heavy ions. It can provide a proton beam ($H_2^+$) with a current of up to 20 $\mu$A.

#### 3.2.3.1 Electron Cyclotron Resonance Ion Sources (ECRIS)

An Electron Cyclotron Resonance Ion Source (ECRIS) [47, 48] creates positive ions inside a magnetically confined plasma. Neutral gas or metal vapour atoms collide with electrons in the plasma and are multiply ionised to an incrementally higher charge state. Higher charge states are required for heavier ions for them to be efficiently accelerated in the cyclotron as the K130 cyclotron extraction energy is proportional to $\frac{q^2}{A}$.

Two solenoid magnets are used for axial confinement of the plasma and hexapole magnets are used for radial confinement (via magnetic mirror effect), creating a minimum in the B-field at the center. For the atoms to be ionised, the electrons in the plasma need to have energies larger than the ionisation energy of the atom (or ion for higher charge states), such that $E_e > I_n$ where $E_e$ is the electron energy and $I_n$ is the energy required to remove the $n^{th}$ electron from the atom or ion. A RF-electric field accelerates the electrons using electron cyclotron resonance (Equation 3.2). The frequency of the electron cyclotron motion in the inhomogeneous B-field only matches the frequency of the RF-electric field in a thin layer or 'shell'. Multiple transitions of the electrons through this 'shell', as they orbit back and forth in the ion source, results in their heating. An ECRIS can be designed to provide a continuous wave of ions or to provide ion pulses.

The K130 cyclotron has access to a 6.4-GHz ECRIS, which was installed in 1991, and a 14-GHz upgraded ECRIS for heavier isotopes and higher charges (installed in 2000) [49].

## 3.3 Radioactive ion beam

The primary beam is injected into a differentially pumped target chamber containing an ion guide. The ion guides contain the target material the primary beam is impinged on and are filled with a helium buffer gas to thermalise the reaction products. The ion-gas mixture is extracted from the ion guide by a pressure gradient and the primary beam carries on towards the beam dump. Different ions guides have been designed for light-ion fusion-evaporation (Section 3.3.1), light-ion fission (Section 3.3.2) and heavy-ion fusion-evaporation reactions (Section 3.3.3).

The beam dump consists of a water cooled, electrically isolated aluminium beam stop, surrounded by radiation shielding made from layers of iron, then borated paraffin, and finally concrete. Aluminium is used as the beam dump due to its short-lived reaction products so the beam dump retains little radioactivity. Fast neutrons are moderated in the paraffin before they are captured by boron atoms [41].

The helium buffer gas is purified to lower than ppm contamination by being passed through a liquid-nitrogen-cooled activated-charcoal matrix, which itself has been baked. The purified helium gas thermalises the reaction products inside the ion guide and reduces their charge down to $1^+$. In theory, most reaction products should end as $2^+$ ions as the $1^{st}$ ionisation energy of He is higher than most $2^{nd}$ ionisation energies of other elements. Experimentally, however, only a few parts per thousand remain as $2^+$ ions and $\sim$0.1-10% are observed to remain at $1^+$ [7]. Losses arise from neutralisation and molecular formation with contaminants (primarily $H_2O$, $O_2$, $H_2$ and $N_2$ [50]) in the buffer gas, which have been ionised by the primary beam or by

collisions with fission fragments. The gas pressure within the ion guide is usually between 100 and 200 mbar.

A potential gradient, created by the curvature of the front-end electrode of the ion guides, funnels ions out of the target chamber and into a SextuPole Ion Guide (SPIG). The pressure gradient is created using a set of three Roots blowers connected to a backing pump. The vacuum pumps also ensure the pressure levels are high enough or low enough to avoid sparking in the extraction region, where ion mean-free paths are either too short to gain enough energy to ionise the background gas, or are long enough for ions to escape the region. The extraction time from the target chamber is of the order of 1 ms [7].

### 3.3.1 Light-ion fusion ion guide

The light-ion fusion guide (shown in Figure 3.7) [50] is used for p, n, d, $^3$He and $\alpha$ induced fusion-evaporation reactions to provide neutron-deficient isotopes that are not created in fission reactions.

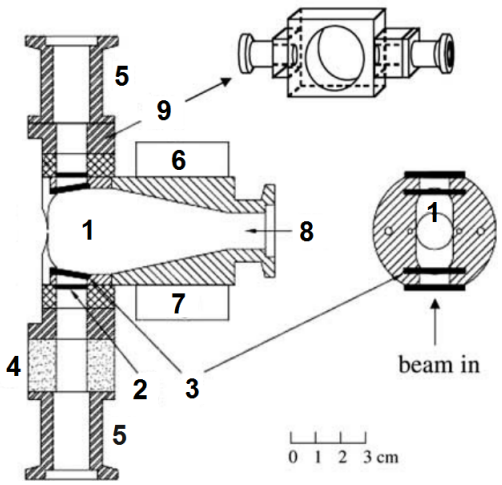


**Figure 3.7:** Fusion ion guide (adapted from reference [50]): (1) stopping volume, (2) Havar windows, (3) targets, (4) graphite collimator [10 mm diameter], (5) primary beam tube, (6) cooling block, (7) heating block, (8) helium input, (9) aluminium frame.

The primary beam passes through a collimator to ensure primary ions do not

impact on the ion-guide walls, then passes through a Havar window and impinges on the target before exiting through a second Havar window on the other side. The Havar windows and beam pipe separate the primary beam from the gas volume of the target chamber, thereby avoiding ionising effects outside the ion guide. The reaction products are stopped (within a 1 cm by 3 cm volume) and thermalised inside the ion guide by the helium buffer gas. A smaller chamber is required to thermalise the reaction products of the light-ion fusion reactions, compared to those of the fission reactions, due to their lower recoil energy. The ionising effect of the primary beam on the buffer gas inside the stopping volume is the main limit to the efficiency of the fusion guide.

The light-ion fusion guide can contain two targets and the ion guide rotated to switch between them, thus allowing fast change of targets while avoiding breaking vacuum. One of the targets is often a material that has been previously studied and is used to optimise the guide parameters.

The fusion guide is bake-able inside the target chamber and is actively cooled during experiments to remove beam heating effects.

### 3.3.2 Fission ion guide

The fission guide (shown in Figure 3.8) is designed for light-ion induced fission reactions and is used to study various neutron-rich fission products [51]. The fission target is usually natural uranium or thorium.

The light-ion fission guide separates the plasma volume, that the primary beam passes through, and the stopping volume with a thin foil. The thin foil allows the high-energy fission products to pass through while preventing the plasma, caused by primary beam ionisation, from entering the stopping volume and causing losses through neutralisation and space-charge effects. Using a neutron beam instead of a proton beam (Section 3.2.2.1) will result in reduced ionisation of the buffer gas.

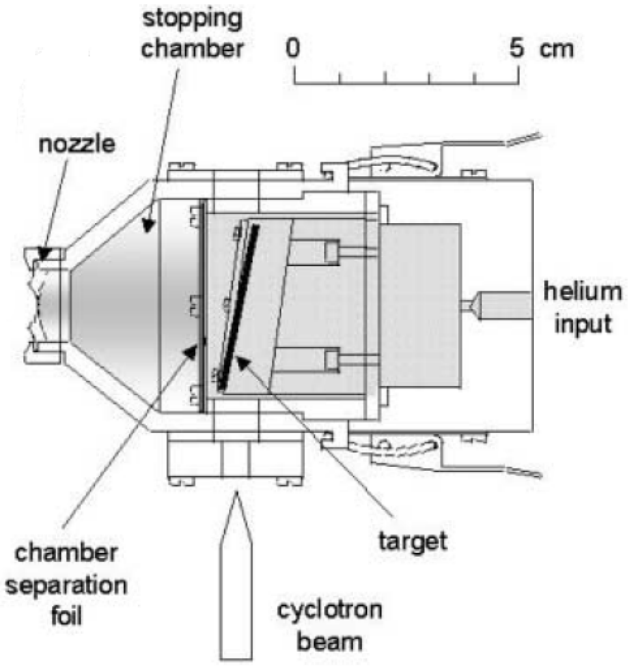


**Figure 3.8:** Fission ion guide (adapted from reference [52])

The primary beam, in a similar manner to the fusion ion guide, passes through a Havar window and impinges on the target inside the plasma volume before exiting through another window. The target is positioned at an angle (7°) to increase the effective thickness of the target that the primary beam passes through. The fission fragments are emitted isotropically, some passing through the separator foil and into the stopping volume. The stopping distance of the fission products is larger than that of the fusion products in the light-ion fusion guide due to their higher recoil energy, therefore a physically larger ion-guide is required.

### 3.3.3 Heavy-ion fusion ion guide (HIGISOL)

The heavy-ion fusion ion guide, shown in Figure 3.9, is used for heavy-ion induced fusion-evaporation reactions [50, 53].

Heavy ions have a much larger ionising effect than lighter ions and the HIGISOL has been designed to remove the primary heavy-ion beam from the stopping gas volume. The design takes advantage of the larger angular spread of the reaction

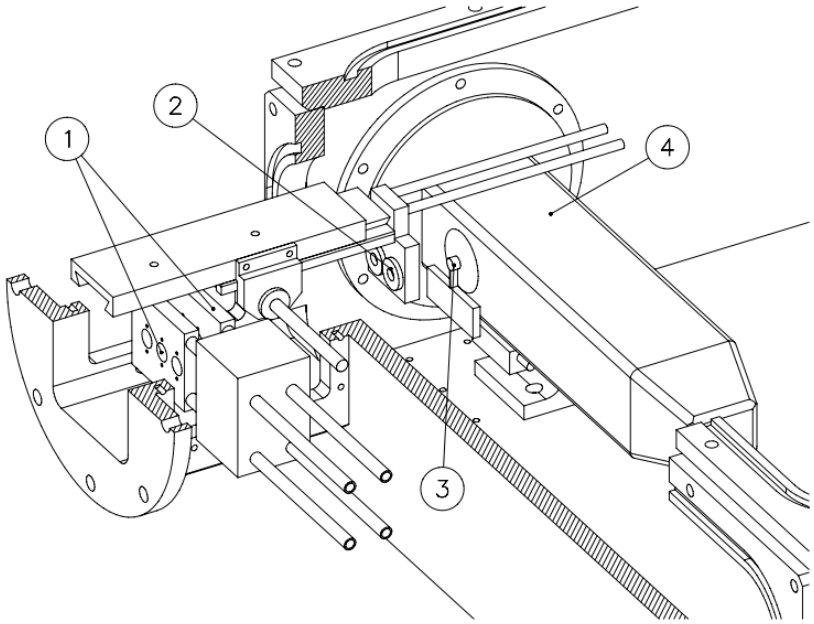


**Figure 3.9:** Heavy-ion fusion guide (HIGISOL): (1) degrader foils, (2) targets, (3) mini beam-stop, and (4) stopping chamber (adapted from reference [50]).

products, due to their lower energy compared to the primary beam, while removing the central region occupied by the cyclotron beam; referred to as the shadow technique [53].

The primary beam impinges on the target and is then dumped onto a mini beam-stop. Reaction products are emitted at a forward angle, with some passing by the beam-stop and entering the stopping volume through a Havar window. A large volume is required to stop and thermalise the high-energy reaction products [50].

The primary beam can be passed through degrader foils to alter the beam energy before impact on the target [50]. Two degrader foil frames are used, each with three circular holes; two filled and one left empty for non-degraded beams. Two targets are held in a removable target frame allowing the quick change of target material and allowing the replacement or changing of the targets without breaking vacuum. The target frame can be moved externally to alter the distance between it and the Havar window, thereby changing the recoil angles that are accepted into the ion guide (between 7° and 63°). Both the degrader frames and the target frame are

water cooled during experiments.

## 3.4 Production of stable isotopes

Stable ion beams can be provided by an electric-discharge cell inside the target chamber or injected into the beam line, just before the magnetic dipole, from the stable isotope production facility. The electric discharge method involves placing a cathode material (typically at −300 to −500 V) inside a grounded cell. Electron showers from the cathode to the cell walls ionise the buffer gas inside the cell, the buffer gas ions are then drawn towards and impact on the cathode. These impacts sputter neutral atoms off the cathode. Sputtered atoms are then ionised inside the target chamber by the plasma and transported out by pressure and potential gradients. The sputtered ions are screened from the potential of the cathode by the surrounding plasma cloud.

Stable beams can also be acquired from discharge off the SPIG or sputtered from the partition foil in the fission ion guide, thereby allowing stable and radioactive ions to be created simultaneously. Having access to both radioactive and stable beams allows the beam-line apparatus to be optimised during on-line experiments and provides critical reference systems for isotope shift measurements.

## 3.5 Extraction

Upon exiting the target chamber, ions enter a two-stage SextuPole Ion Guide ("double-SPIG"), which transports the ions towards the extraction electrodes whilst allowing the neutral gas out the sides. The SPIG, and a previously-used skimmer electrode, separate the ions from the neutral gas so that they may be accelerated in high vacuum without the collisions a neutral gas background would cause. The ion energies in this region are typically of a few 100 eV and the ion density means space-charge

effects must be considered. Upon exiting the SPIG, the ions are extracted by a 20 kV (relative to 30 kV platform) extraction electrode and a grounded extraction electrode, and then transported towards the dipole magnet for mass separation.

### 3.5.1 SextuPole Ion Guide (SPIG)

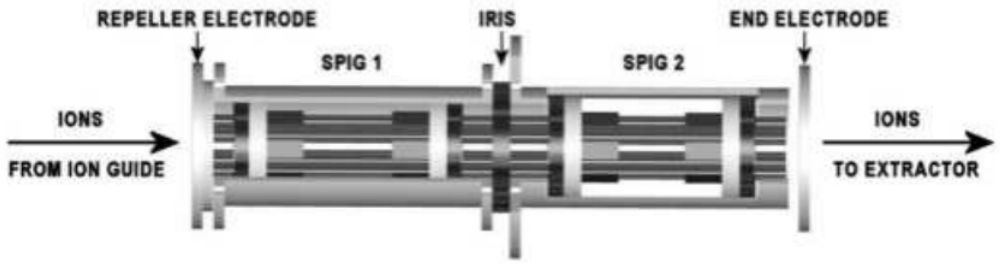


**Figure 3.10:** Diagram showing the double-SPIG (SextuPole Ion Guide) [54].

The SPIG consists of six electrode rods, running parallel to the beam axis, that have a DC voltage imposed on radio-frequency oscillations (adjacent rods being of opposite phase). The device acts to focus the ions onto the central axis and transports them downstream using a small potential gradient. The device is of an open design to ensure the neutral gas is evacuated out the sides. The alignment of the ion transition into the SPIG is less critical than that of the previously used skimmer electrode. A sextupole, rather than a quadrupole, was chosen as it provides a pseudo-potential that has a broader minimum and that is steeper near the rods, thus allowing greater intensity currents through as space-charge effects are less of a problem in the wider potential trough [55]. The pseudo-potential created by the $n^{th}$ multipoles (n=2 for quadrupoles, n=3 for sextupole, n=4 for octupoles, etc...) is given by,

$$V_r^* = \frac{q^2 U_{RF}^2 n^2}{4m\omega^2 r_\circ^2} \left(\frac{r}{r_\circ}\right)^{2n-2}$$

where $q$ and $m$ are the ion charge and mass respectively, $U_{RF}$ and $\omega$ are the amplitude and angular frequency of the RF signal respectively, and $r$ and $r_\circ$ are the radial

distance of the ion from the central axis and the distance from the central axis to the multipole rods respectively.

The SPIG was found to provide a greater yield than the skimmer electrode by ∼7-8 times for the light-ion fusion ion guide and ∼ 5 times for the fission guide [55]. The greater gas flow also provides some ion transport beyond that provided by the potential gradient and has a slight cooling effect as buffer gas atoms collide with the ions. The main limitation of the SPIG are the space-charge effects that increase with beam current, resulting in a reduced penetration depth of the RF-electric field.

### 3.5.2 Laser Ion Source Trap (LIST)

The double-SPIG can also be used as a Laser Ion Source Trap (LIST) [55], where ions, instead of being transported into the SPIG, are repelled back by a positive potential (repeller electrode in Figure 3.10) and only neutral atoms are transported into the device. The neutral atoms can then be selectively ionised inside the SPIG to provide an elementally pure beam. The elementally pure beam is then mass separated to provide an isotopically pure beam.

It was found that the gas jet coming out of the ion guide exit is narrower for higher pressures in the $1^{st}$ SPIG, therefore providing a greater overlap with the ionising laser beams. The $1^{st}$ SPIG is enclosed by a metal cylinder to intentionally create this high pressure, which is controlled by the iris connecting the two SPIG sections. The laser light is tuned to selectively ionise the atoms of interest in the $1^{st}$ SPIG section and the neutral gas is then pumped out in the $2^{nd}$ SPIG. The pressure in the $1^{st}$ SPIG, the $2^{nd}$ SPIG and the extraction electrode is $\sim 0.1$, $\sim 10^{-4}$ and $\sim 10^{-5}$ mbar respectively.

An advantage of the LIST method is the reduced charge density in the double-SPIG, therefore reducing problems from space-charge effects. Also neutralisation losses in the ion guide become part of the process and can be encouraged. This

is especially useful when using the fission guide where a major loss is the plasma inside the stopping volume, caused by collisions between the high-energy reaction products and the buffer gas, neutralising ions before they are extracted.

#### 3.5.2.1 Fast Universal Resonant laser IOn Source (FURIOS)

The FURIOS facility [56, 57] consists of a laser cabin containing two laser systems. Together they provide a universal coverage of optical ionisation schemes across the periodic table. Laser beams can be injected directly into the ion guide, through the back and side, or through the dipole magnet for LIST experiments. The set-up for LIST experiments using FURIOS is shown in Figure 3.11.

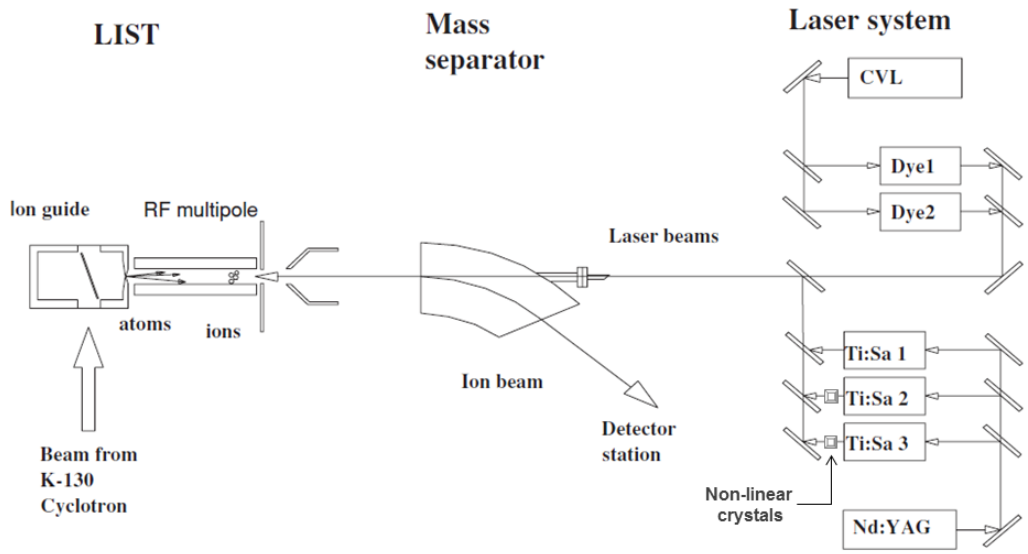


**Figure 3.11:** Schematic of the FURIOS twin laser system pumping through the dipole magnet for LIST experiments. Adapted from [56].

The first laser system is an all solid-state laser set-up that uses a high-repetition rate (10 kHz) diode-pumped 532 nm Nd:YAG laser (up to 100 W) to pump three tunable titanium sapphire, TiSa, lasers. Non-linear crystals are used to double and triple the frequencies of two of the TiSa laser beams and the set-up can produce laser light with wavelengths between $\sim$ 280 (UV)$-$900 (IR) nm. Each TiSa laser can provide laser pulses of 30$-$50 ns with 2 W fundamental beam power.

The second laser system uses a high-repetition rate (10 kHz) copper vapour laser (up to 50 W) to pump a pulsed dye laser and pulsed dye amplifier. The set-up can provide laser beams of wavelengths between 520−850 nm, depending on the dye used, in pulse lengths of the order of a few ns. The pulsed dye amplifier is a gain medium that amplifies the primary laser beam passing through it, thus providing a boost to the beam power while retaining the line width.

In this work the TiSa lasers are used to optically pump ions in the Cooler-Buncher for spectroscopy experiments.

## 3.6 Mass-separation, cooling and optical pumping

Upon extraction, ions are transported towards the dipole magnet for mass separation. Unlike the electrostatic fields used throughout the rest of the beam-line, an ion's interaction with the magnetic field created by the dipole magnet depends on its charge and its velocity. By varying the strength of the magnetic field it is possible to separate different isotopes according to $\frac{m}{q}$ and acquire an isobaric beam. The mass resolving power ($\Delta M/M$) of the IGISOL dipole magnet was typically a few hundred when a skimmer extraction electrode was used [8]. Replacing the skimmer extraction electrode with the SPIG improved this to around 1100 due to the reduced energy spread [10]. After the dipole magnet, the beam enters the switch yard where it carries on towards the Cooler-Buncher or can be deflected to either side, such as towards a silicon or germanium detector station. The silicon and germanium detectors are used to detect beta and gamma radiation, respectively, which are used to optimise the yield of the isobaric beam. The pressure beyond the extraction electrodes and throughout the dipole magnet and switch yard is $\sim 10^{-6}$ mbar.

Following mass separation, the ions are injected into, and stopped inside, the Cooler-Buncher (described in Section 4.1.1), which is mounted on a high voltage platform at 30kV. The ions are cooled to an energy spread of $< 1$ eV and released

in a bunch of typically $\sim$ 10 $\mu$s size [10, 58]. If desired, light from the titanium-sapphire lasers from the FURIOS facility can be used to optically pump ions into metastable states while trapped inside the Cooler-Buncher [14]. In the future, ions may be resonantly ionised to the doubly-charged state inside the Cooler-Buncher so they may be separated from singly-charged contaminants upon release.

Before the installation of the Cooler-Buncher the intensity and energy spread of extracted IGISOL beams were observed to increase with skimmer voltage. Thus a compromise had to be found between intensity and line width, with optimal conditions typically giving an energy spread of up to 150 eV. The Cooler-Buncher acts to reduce this spread and thus decouples the beam properties from that of the ion guide (allowing the optimisation of the beam current). Furthermore, it also reduces the emittance and energy spread of the ions to below 1 eV, increasing the efficiency and resolution of the spectroscopy experiments due to the reduced broadening of the spectral lines and increased overlap with the laser beam at the light collection region. The device also allows the ions to be optically pumped in a low-energy region (800 eV), where the decreased emittance results in a slow but less divergent beam .

The bunching of the ions allows photon detection to be gated to when the ions pass through the detection set-up, therefore reducing background from laser scatter by up to three or four orders of magnitude. The pressure inside the Cooler-Buncher is $\sim$0.1 mbar, with lower pressures used in bunching mode to reduce losses from molecular formation.

Upon release from the Cooler-Buncher, the ion bunch is accelerated to 800 eV into the low energy region (relative to a 29.2 kV platform) and is then diverted towards either the Penning trap or towards the laser spectroscopy station. At IGISOL 3 the Penning trap was placed immediately downstream from the Cooler-Buncher, with a quadrupole deflector in between to redirect the released ion bunches towards the laser spectroscopy station (Figure 3.1). This set-up thus required the Penning trap

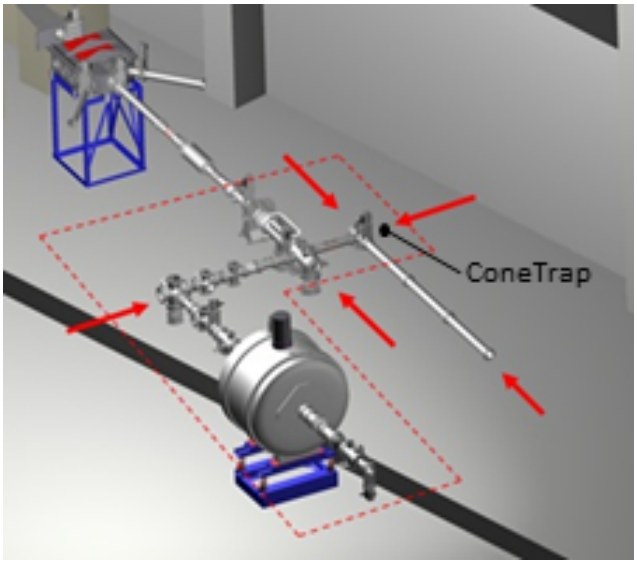


**Figure 3.12:** Laser access to high-voltage region for optical pumping of trapped and slow moving ions.

to be disconnected to provide access for optical pumping. The IGISOL 4 has a "hammerhead" delivery system (Figure 3.2) after the Cooler-Buncher where the ions are directed by a quadrupole deflector towards either the Penning trap or the laser interaction region. The new layout allows access for the optical pumping of ions in the Cooler-Buncher and in the low energy region

Optical pumping is used to increase the population of a desired metastable state if the transitions from the ground state are too weak or if it has no suitable transitions in range of the high resolution dye lasers used for spectroscopy. A problem with laser pumping in the Cooler-Buncher is that high-lying states (>1 eV) can be de-excited by collisions, thus laser pumping in a high vacuum is desirable to avoid this. Inside the low-energy region, the slow velocities of the ions make efficient in-flight laser pumping, in vacuum, possible.

Laser access for pumping is possible in several locations in the low-energy region (indicated in Figure 3.12), including inside an electrostatic ion trap (ConeTrap) where the ions can be trapped, and laser pumped, for up to a few seconds in high vacuum. The pressure in the post Cooler-Buncher sections are $\sim 10^{-7}$ mbar, produced using several turbo-molecular and oil-free scroll pumps.

## 3.7 Spectroscopy

Figure 3.13 illustrates the light collection region (LCR) of the IGISOL 4 laser-line [7, 59].

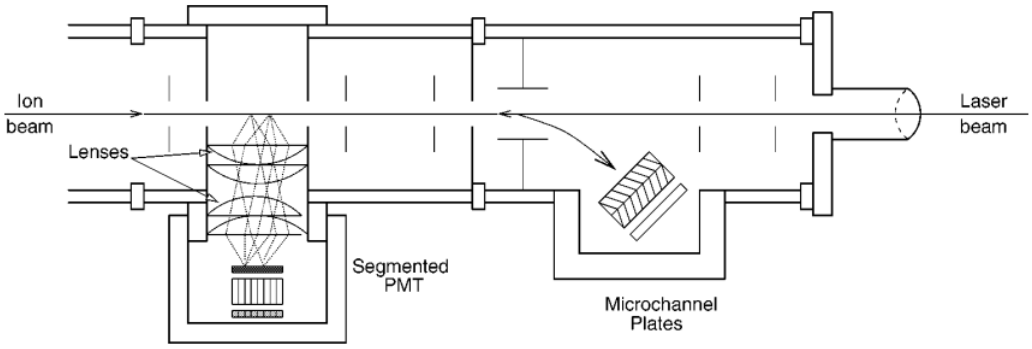


**Figure 3.13:** Light collection region

The LCR houses a lensing system, consisting of a quartet of fused silica lenses, that focuses the fluorescent photons emitted by the illuminated ions onto a 16-fold segmented photomultiplier tube (PMT). The LCR is held at a potential that can be precisely tuned to alter the local Doppler shift of the ions, thus scanning the effective frequency of the laser light. The frequency of the laser light in the reference frame of the ions is given by,

$$\nu = \nu_0 \frac{1+\beta}{1-\beta}$$

where $\nu$ is the frequency, $\nu_0$ is the laser frequency in the laboratory frame and $\beta$ is defined as,

$$\beta = \sqrt{1 - \frac{1}{(1+\frac{eU}{mc^2})^2}}$$

where $U$ and $m$ are the total acceleration and the ion mass respectively.

The LCR voltage can be incrementally changed to sweep over a transition frequency and resonantly-scattered photons are individually counted to determine res-

onances within the hyperfine structure. The incrementation of the LCR voltage is used as it is more stable and reproducible than changing the dye laser frequency. The dye laser frequency is instead kept constant using the locking system described in Section 2.4.1.

A variety of apertures inside the LCR, including a 1-mm aperture, are used to ensure overlap of the ion beam and the laser beam (a 6-mm aperture situated ∼3 m upstream is used to ensure low angular divergence of the ion beam).

Beyond the LCR, fast-switching beam deflectors and microchannel plates (MCP) are used to measure the current of the ion beam both for diagnostics and for photon-ion coincidence measurements (Section 3.7.2). Typical bunched ionic ensembles are, however, of too high a current for the MCP and therefore the MCP can only be used with continuous beams.

### 3.7.1 Bunched beam spectroscopy

The use of bunched ions allows the counting of photons to be gated to when the ion bunch is passing through the LCR [12]. This suppresses the background from random laser scatter (which is $\sim$ 200 photons per second per mW) by the ratio between the accumulation time in the Cooler-Buncher ($10 - 400$ ms) and the gate width (typically ∼15 $\mu$s); usually by a factor of around $10^4$.

Timing apparatus is used to determine whether detected photons originated from ions at the front or back of the bunch, therefore determining the velocity of the ions and the Doppler shift of the laser light in their reference frame. This can then be used to improve the resolution of the spectra provided by the incremented LCR voltage (Figures 3.14(a) and 3.14(c)); this difference between ion Doppler shifts within the bunch is illustrated in Figure 3.14(b) where the photon counts from ions with two different arrival times are presented.

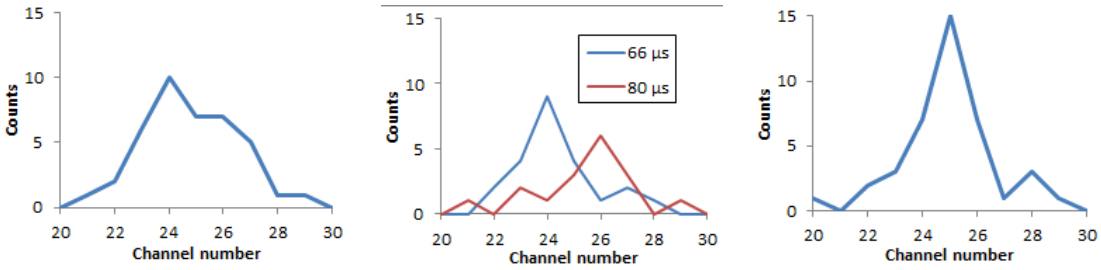


(a) Combined, raw counts. (b) Comparing photons counts at 66 $\mu$s and 80 $\mu$s arrival times. (c) Adjusted data set.

**Figure 3.14:** Improvement of data collected for ions with time-of flights of 66 $\mu$s and 80 $\mu$s; illustrated by previous data taken at IGISOL 3.

### 3.7.2 Photon-ion coincidence

Prior to the installation of the Cooler-Buncher and the use of bunched beams, delayed photon-ion coincidence was the most sensitive method of reducing spectroscopic background that the laser IGISOL group had achieved [7, 59]. This technique involved scattered photons, detected in the PMT, triggering a delayed window to accept signals caused by ion impacts on the MCP [60]. The PMT segmentation allows the time resolution to be reduced to $\lesssim$20 ns.

The critical problem with the delayed photon-ion coincidence method is that contaminant ions in the bunch trigger false acceptances, thus creating background.

### 3.7.3 Charge exchange cell (CEC)

Immediately upstream of the LCR, a separate high-voltage platform contains a charge exchange cell (CEC) that can be used to neutralise the ions through charge exchange interactions with a buffer gas (usually an alkali metal vapour). The buffer gas is held at a constant vapour pressure, where the mean-free path of the ions through the CEC is equivalent to the cell length. At this pressure each ion will collide, on average, with a buffer gas molecule only once, thus providing charge exchange without significant increase in beam divergence.

Spectroscopy of atomic species is favourable as the electrons in a neutral atom

are less tightly bound than in a positive ion, therefore transition energies decrease upon neutralisation; this may be required if no transition in the ion is within range of the dye laser. When in operation, the CEC high-voltage platform is tuned to scan the effective frequency of the laser light rather than tuning the voltage at the LCR.

Charge exchange may also be exploited as a spectroscopic tool. State-dependent charge exchange, where the neutralisation cross-section of ions increase when optically pumped into a metastable state [61], can be used to increase the neutralisation rate of ions in the CEC. This can be used to increase the neutralised yield for collinear laser spectroscopy, or the effective frequency of the laser light can be scanned over the hyperfine structure and the ions and atoms counted to determine resonances.

There is the possibility of populating particular states of interest upon neutralisation. This 'state-selective neutralisation' occurs due to the difference in ionisation energy of the neutralised atom and the buffer gas, as shown by,

$$M^+ + G \rightarrow M + G^+ + \Delta E \rightarrow M^* + G^+$$

where M is the isotope in the beam and G is the buffer gas. For state-selective CEC to succeed the ionisation difference has to be resonant with the required state energy, both of which are purely chemical properties of the elements. Slightly off-resonant entrance channels will result in the population of many different states at the expense of the population of the desired state.

## 3.8 Beam-line simulation

The electrostatic elements of the IGISOL 4 beam-line, post Cooler-Buncher, were mapped out in the ion-optics simulation program, SIMION (described in Section 5.1). Figure 3.15 shows the simulation of the beam-line and the installation point of the ConeTrap (Chapter 5). The simulation of the beam-line was used to determine

the parameters required to optimise beam transport, points for diagnostics and strategies for tuning of the beam-line components.

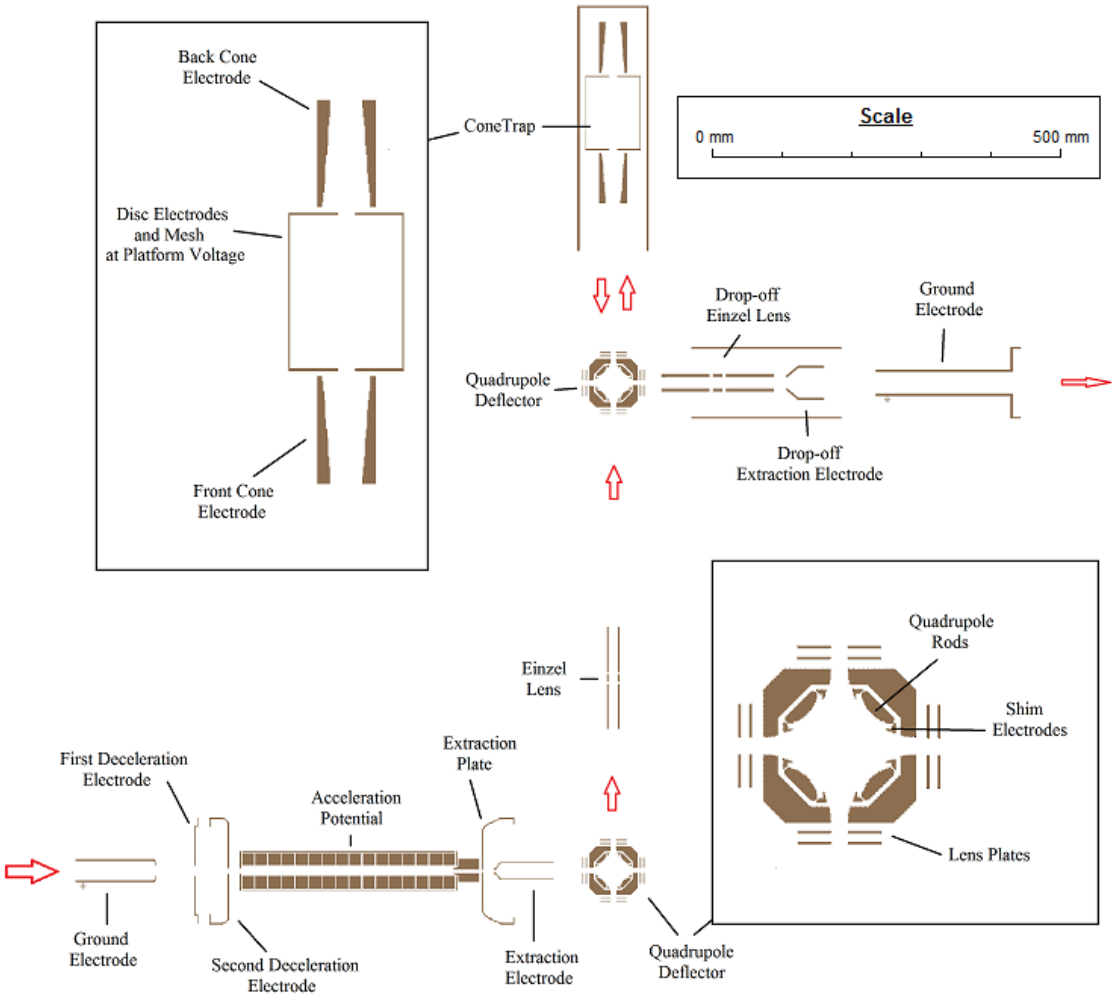


**Figure 3.15:** Simulation of the beam-line after the Cooler-Buncher. Shown are the electrode structure of the Cooler-Buncher, the two quadrupole deflectors used to divert the ion bunches after the Cooler-Buncher and towards the laser cabin, the Einzel lens used to transport the ion bunches between the two quadrupole deflectors, the Drop-off from the HV region and the installed ConeTrap.

After the Cooler-Buncher, ions enter the low energy region, which sits at ~800 V below the Cooler-Buncher platform voltage of 30 kV. Ion ensembles released from the Cooler-Buncher were simulated using 1000 ions of 100 u mass and 800 eV kinetic energy, flown separately within a 10 $\mu$s uniform bunch length. An emittance of 3 $\pi$ mm mrad was simulated by randomly emitting the ions within a 1-mm radius

and a 0.135° half-angle spread.

The first quadrupole deflector redirects the ions towards either the laser spectroscopy station or the JYFLTRAP (not included in these simulations). An Einzel lens (discussed in Section 3.8.2) was designed to focus the ions into the second quadrupole deflector, to redirect ions towards the light collection region (LCR), or into the ConeTrap. A Faraday cup was chosen to be placed beyond the ConeTrap to determine the optimal parameters for the first quadrupole deflector and the Einzel lens. The potentials required on the quadrupole deflectors, to redirect the ions by 90°, are discussed in Section 3.8.1.

When the ConeTrap is in use the second quadrupole deflector voltage has to be switched from ground, to allow ions to pass through to the ConeTrap, to a voltage that redirects the ions towards the LCR upon release from the ConeTrap. The timing required for this voltage switch is discussed in Section 3.8.3.

After they are redirected towards the LCR, the ions drop off the high-voltage platform and are accelerated to 30 keV.

### 3.8.1 Quadrupole deflectors

Quadrupole deflectors use a combination of so-called 'rod' and 'shim' electrodes to create a hyperbolic electrostatic potential that is capable of bending incoming ions by ±90° and allowing atoms, laser light and ions (when inactive) to pass through [62]. In the idealised operation of the quadrupole deflectors, all rod and shim electrodes have an applied potential and each shares the same respective voltage in magnitude, with only the polarities of adjacent poles being opposite. The combination of the rod and shim electrodes reflects the fact that a pure hyperbolic electrode results in ions colliding with the inner electrode and a purely circular electrode only provides a hyperbolic field within the central region. The different voltages on the rod and shim electrodes and the properties of the input beam determine the profile of the

output beam. Figure 3.16(a) shows a quadrupole deflector redirecting a parallel beam of ions and the typical increase in divergence of the deflected ions. Focusing elements are therefore essential and Einzel Lens plates, added on all sides of the quadrupole deflector, can be used to focus the ions on entrance or exit from the deflector.

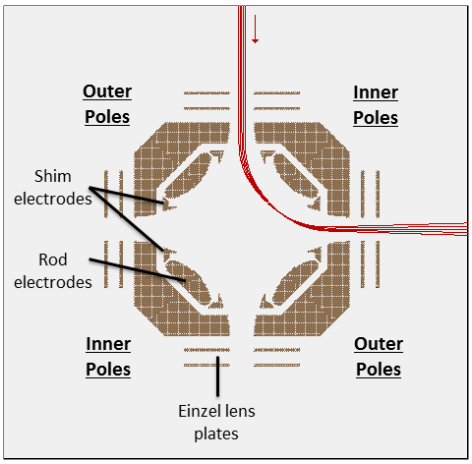


(a) Diagram showing a quadrupole deflector diverting a parallel ion beam by 90° (and the subsequent diverging effect of the bend). The rod and shim electrodes referred to as the inner- and outer-poles are shown.

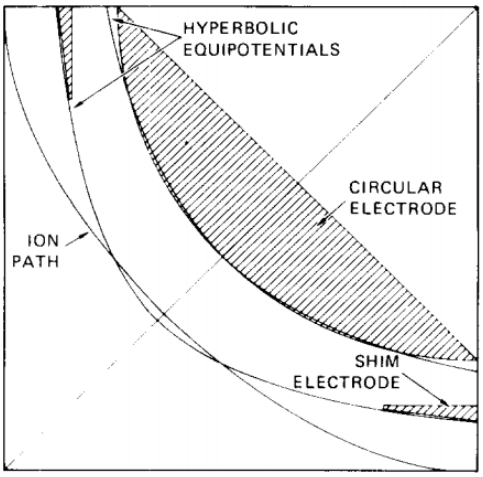


(b) Close up of an ions trajectory through a quadrupole deflector. The figure shows the electrostatic field created by the circular electrode deviating from that of a hyperbolic field at the edges and the ion path colliding with the hyperbolic equipotential created by the shim electrodes [62].

**Figure 3.16:** Quadrupole deflector diagrams.

Figures 3.17(a) and 3.17(b) show the angular deviation from 90° and the offset from the central axis respectively for a beam exiting the quadrupole deflector using all rod and shim electrodes; henceforth referred to as an "idealised" quadrupole deflector. The figures clearly indicate two forms of stable region; a long, narrow region of low axial deviation and a curved region that produces 90° deflection but with an offset to the exit beam. The two regions intersect to form a wider area that provides a stable, ∼90° deflection around $V_{rod} \sim 400$ V and $V_{shim} \sim 1100$ V. The axis-aligned region is linear for the majority of its locus and (neglecting deviations at the edges) can be described by,

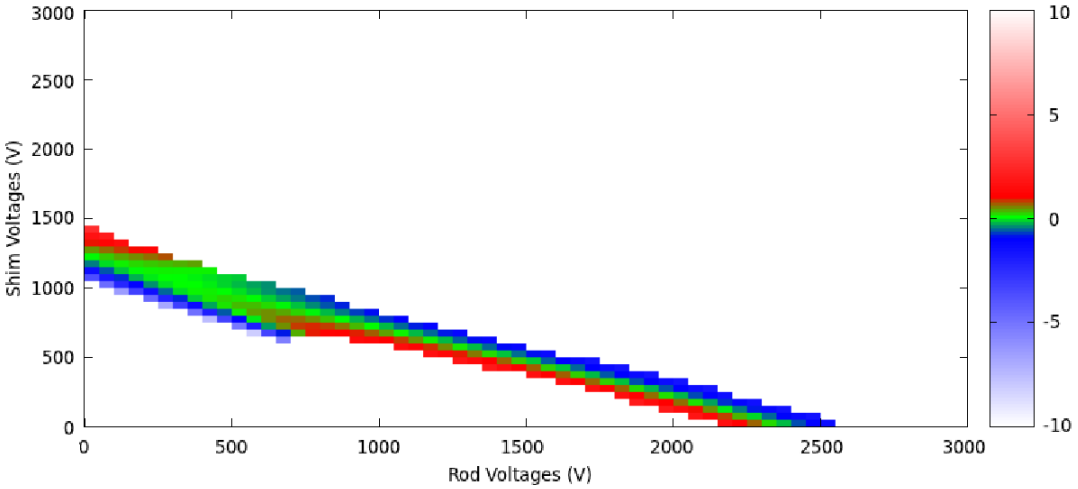


(a) Angular deviations from 90 degree deflection in degrees.

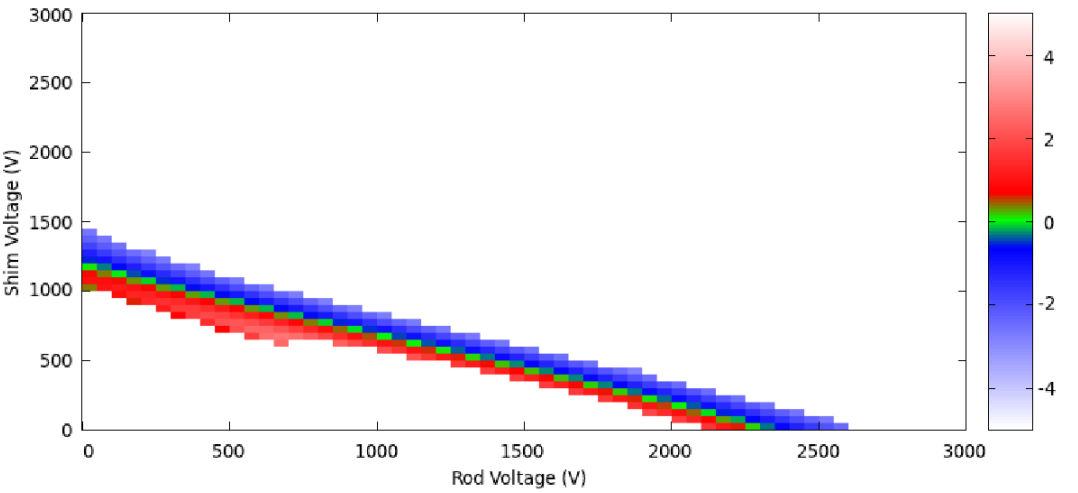


(b) Offset from central axis in mm.

**Figure 3.17:** Angular deviation from 90° and offset from central axis for beams exiting an "idealised" quadrupole deflector. Angular deviations and offsets are measured with respect to the incoming beam axis, where negative angles deviate towards the source and offsets are measured where the beam passes through the exit Einzel plates. The voltages are magnitudes only, with inner poles at negative polarity.

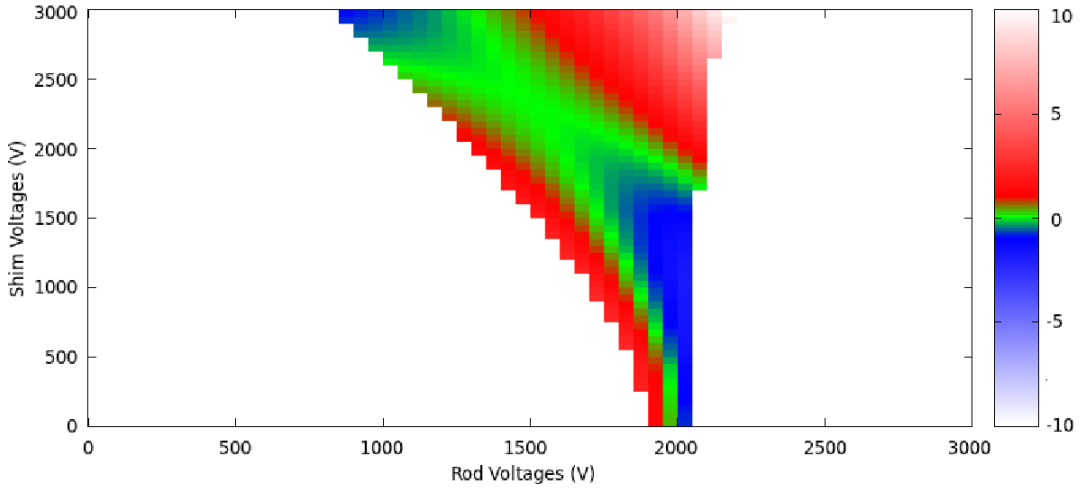


(a) Angular deviations from 90 degree deflection in degrees.

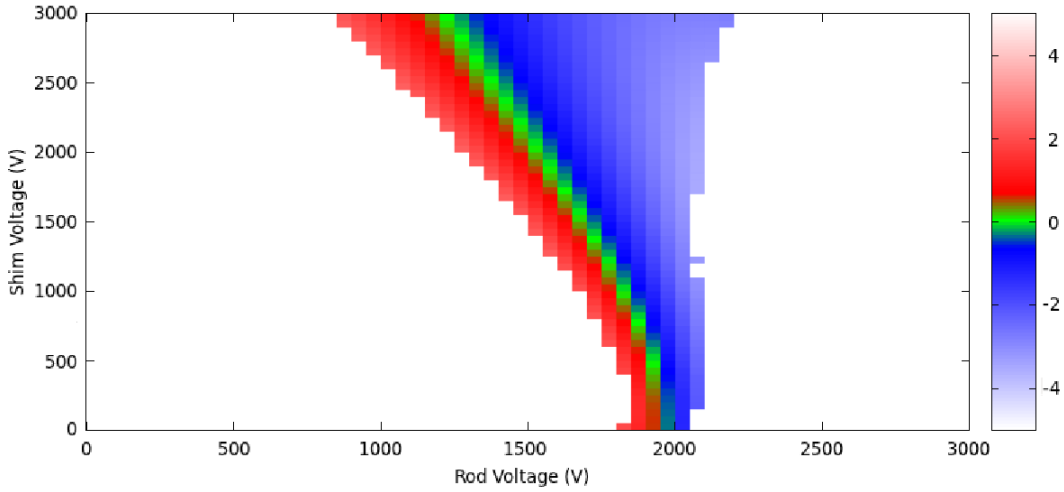


(b) Offset from central axis in mm.

**Figure 3.18:** Angular deviation from 90° and offset from central axis for beams exiting a quadrupole deflector using typical IGISOL 3 experimental settings. Angular deviations and offsets are measured with respect to the incoming beam axis, where negative angles deviate towards the source and offsets are measured where the beam passes through the exit Einzel plates. The voltages are magnitudes only, with inner poles at negative polarity.

$$|V_{shim}| = -0.487|V_{rod}| + 1.5E_{ion}$$

for all ion energies, $E_{ion}$.

When optimised experimentally, the quadrupole deflectors at the IGISOL 3 facility were found to efficiently operate with only the inner shim electrodes and the outer rod electrodes in operation. This simplifies their use and reduces the number of required voltage supplies. Figures 3.18(a) and 3.18(b) show the angular deviation from 90° and the offset from the central axis, respectively, for a beam exiting an 'IGISOL 3' set quadrupole deflector. The figures show much wider stability for the deflection of ions by 90°, thus improving the transport efficiency of the quadrupole deflectors and making them easier to deploy. The aligned region for an 'IGISOL' quadrupole deflector is also approximately linear and can be described by,

$$|V_{shim}| = -3.465|V_{rod}| + 9.42E_{ion}.$$

Figure 3.19 shows a simplified comparison of the aligned and offset 90° deflection regions for both the 'idealised' and 'IGISOL' set quadrupole deflectors. The 'idealised' quadrupole deflector has potential gradients that change quickly with voltage, resulting in the narrow bending regions, while the 'IGISOL' settings have gradients that change slowly with voltage due to the grounded electrodes, resulting in the wider bending regions.

The offset region in an 'idealised' quadrupole deflector is greatly affected by changes in the shim electrode voltages, with multiple solutions existing for some rod voltages. This is due to the fringe fields created by the shim electrodes and the grounded deflector box affecting the ion trajectories as they leave the quadrupole. The offset region in an 'IGISOL' deflector changes less rapidly with shim voltage due to the loss of the outer shim electrode potentials. The relationship between the offset regions and the rod and shim electrode voltages for the two deflector settings

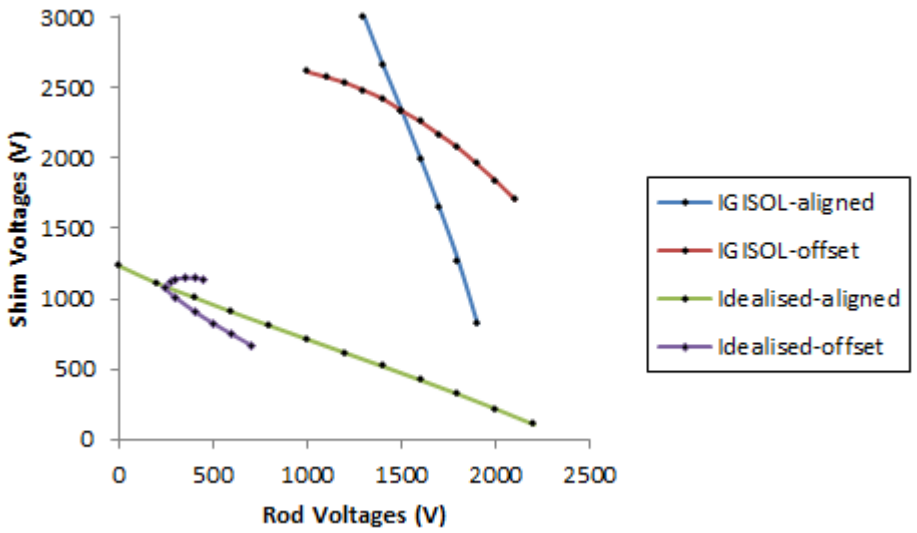


**Figure 3.19:** Aligned and offset 90° deflection voltages for the 'idealised' and 'IGISOL' settings of the quadrupole deflector.

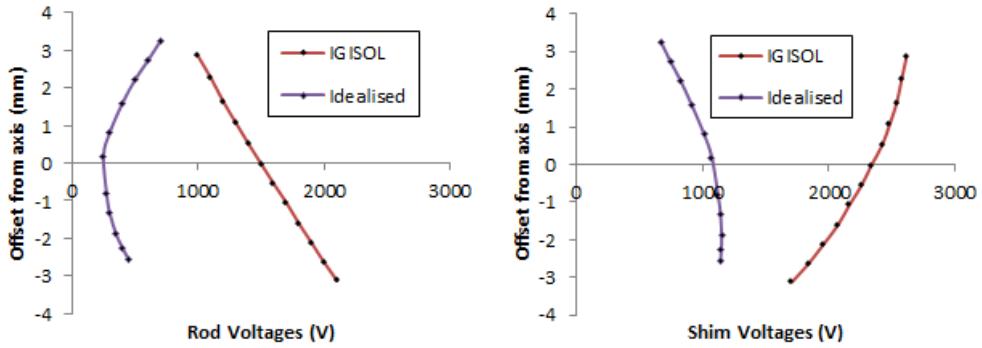


(a) Offset in relation to the rod voltages. (b) Offset in relation to the shim voltages.

**Figure 3.20:** Offset from central axis for the 'idealised' and 'IGISOL' quadrupole deflectors.

are shown in Figures 3.20(a) and 3.20(b) respectively.

The voltages found to work at the IGISOL 4 facility were $V_{rod} = 1650$ V, $V_{shim} = 1200$ V for the first deflector, suggesting the Cooler-Buncher provides an offset to the released ions, and $V_{rod} = V_{shim} \simeq 1700$ V for the second quadrupole deflector.

### 3.8.2 Hammerhead beam transport

An Einzel lens and a quadrupole triplet were both considered for the purpose of transporting ions between the two quadrupole deflectors to avoid losses from diver-

gence. The quadrupole triplet was considered due to its versatility in manipulating the beam profile and trajectory, however the Einzel lens was explored for its simplicity due to the reduction in required power supplies compared to a quadrupole triplet. Both are illustrated in Figure 3.21 and their dimensions described in the caption. The Einzel lens has been built and is currently in use at IGISOL 4.

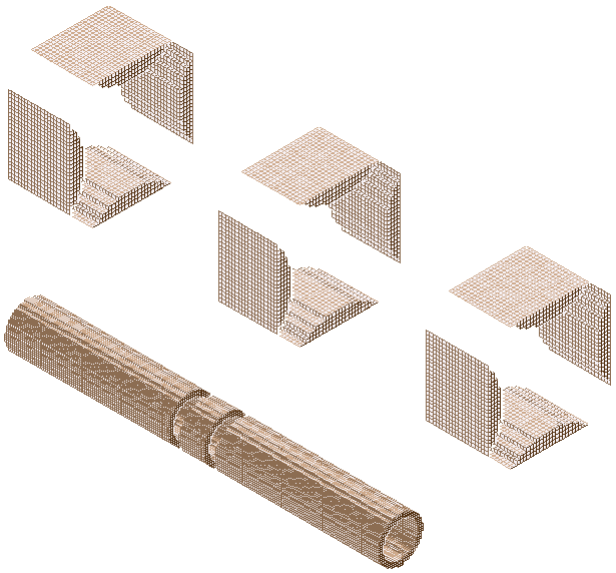

**Figure 3.21:** The possible hammerhead beam transport optics: (top) a quadrupole triplet (17.2mm radius rod curvature, 20mm long with 30mm between opposing electrodes and 45mm gaps) and (bottom) an Einzel lens (outer electrodes 70mm long, inner electrode 14mm long, 10mm inner radius and 5mm gaps between electrodes).

### 3.8.3 Voltage-switch timing for ConeTrap operation

When the ConeTrap (Chapter 5) is in use, the voltages of both the injection-extraction cone electrode and the second quadrupole deflector must be rapidly switched to trap and release the ions and to divert them towards the light collection region. The timing for this operation is shown in Figure 3.22. The timing for raising and lowering the injection-extraction cone electrode voltage is identified as critical for efficient trapping of the ion bunch (and to avoid losses due to the "drift tube" effect) and is required to be $<\mu$s. The circuitry designed for this rapid

switch is discussed in Section 5.3.2. The quadrupole deflector can, by virtue of the ConeTrap storage time, be slowly switched on a time scale of milliseconds.

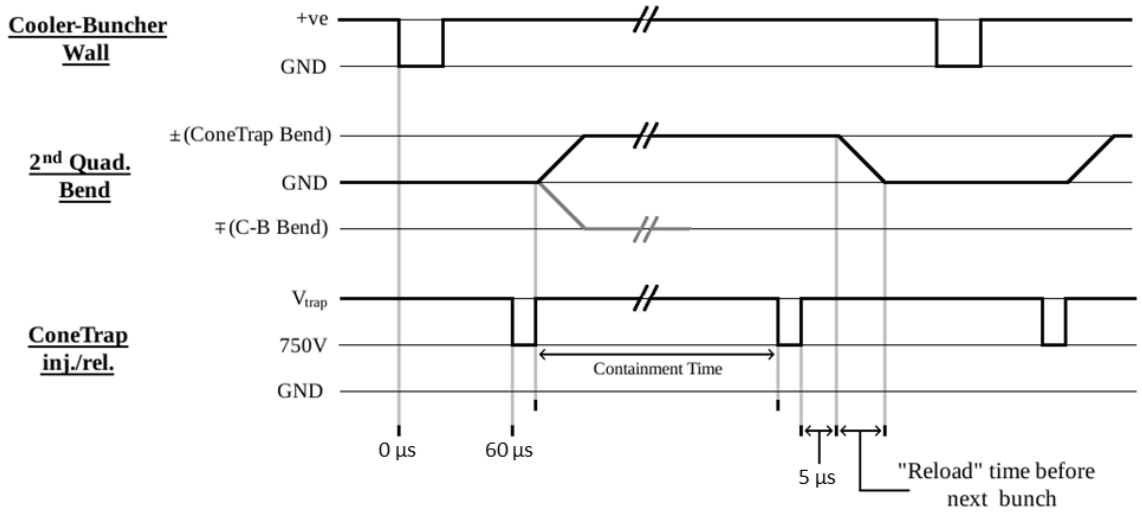


**Figure 3.22:** Voltage switch timing when using the ConeTrap. The Cooler-Buncher releases the ions by dropping the potential wall, the second quadrupole deflector is at platform potential to allow the ions to pass through to the ConeTrap and then redirects them towards the light collection region (LCR) upon release (the dark grey line indicates the voltage setting to deflect ions coming from the Cooler-Buncher). The injection-extraction cone electrode voltage has to change at the appropriate time (∼60 $\mu$s delay after the Cooler-Buncher release signal) to efficiently trap the ions after they are released from the Cooler-Buncher. The second quadrupole deflector cannot be switched to ground until the released ion bunch has been redirected towards the LCR (∼5 $\mu$s transport time).

A 160 $\mu$s propagation delay occurs between a micro-controller sending the signal to raise the quadrupole deflector voltage and the voltage actually switching. The switch time for the quadrupole deflector is ∼1 ms and the delay given to allow ions to be transported through the deflector was arbitrarily set to 1 ms.

The circuitry required to coordinate the voltage switches of the quadrupole deflector and ConeTrap according to the Cooler-Buncher release signal, combined with appropriate delays, has been designed in this work (Section 5.3.2).

## 3.9 Data acquisition (DAQ)

The existing data acquisition method involves incrementing the light collection region voltage to Doppler shift the effective frequency of the laser light and scan over the hyperfine structure (HFS). A histogram is plotted of the photon counts in bins of well-determined, stepped acceleration voltages, which can then be used to determine the effective frequency of observed resonances. The photons' arrival times are recorded to improve the resolution of the measured spectrum (as discussed in Section 3.7.1). Two methods of improving this data acquisition technique at IGISOL 4, developed outside of this work, are currently under consideration and are described below.

One method under consideration is to only count when two photons are received close together within the same bunch. The probability of two background photons being detected in close proximity is minimal, thus "burst" counting could greatly reduce background from random laser scatter. A second method is to increase the amount of time spent on resonance. This can be achieved by increasing the 'dwell' time according to how many photons have been detected at that voltage during either the previous or current scan. This results in an exponential increase in the amount of time spent on resonance. The spectra obtained using this technique are then normalised according to the amount of time spent at each voltage increment.

# CHAPTER 4

# Ion traps

This chapter discusses the theory behind and technical design of the ion traps already in use at the IGISOL facility. First, the theoretical quadrupole (or Paul) traps are described followed by the details of the linear rf-quadrupole trap implemented on the IGISOL beam-line (the Cooler-Buncher). A theoretical discussion of the Penning Trap and a brief description of the double Penning trap (used at the facility for precision mass measurements) is then presented.

## 4.1 Quadrupole traps

Quadrupole (Paul) traps [63] confine ions by exploiting the strong focusing effect of rf-oscillating quadrupole (RFQ) fields. Such a quadrupole field may be produced using hyperboloid electrodes or rods, with adjacent rods at anti-phased AC potentials. Cylindrical rods may be used if their radii are suitable to provide the same effect in the central region (equal to $1.15r_0$, where $r_0$ is the distance from the central axis to the rods). Point-like confinement may be achieved in a 3D quadrupole trap, which consists of a ring electrode and two hyperbolic endcaps, and linear confinement may be achieved using a 2D quadrupole trap, which consists of four hyperboloid or cylindrical rods confining the ions to the central axis. A linear quadrupole trap can be used as a mass filter, if an axial DC potential is applied to the rods, or, if a DC

gradient is applied, as an ion guide.

The equation of motion for an ion in a linear quadrupole trap is,

$$\ddot{x}_i \pm \frac{q}{mr_0^2}(U + V\cos\omega t)x_i = 0$$

where $x_i$ is the ions coordinates relative to the central axis, $q$ and $m$ are the ion charge and mass respectively and $\omega$ is the oscillation frequency. The amplitudes of the DC voltage and rf-voltage are $U$ and $V$, respectively.

This category of differential equation is commonly referred to as a Mathieu equation and is usually rewritten in the form,

$$\frac{d^2x_i}{d\tau^2} \pm (a + 2q\cos 2\tau)x_i = 0$$

where,

$$a = \frac{4eU}{mr_0^2\omega^2}\ ,\ q = \frac{2eV}{mr_0^2\omega^2} \text{ and } \tau = \frac{\omega t}{2}.$$

The three dimensional Mathieu equations have stable solutions, where ions oscillate with finite amplitude in the transverse directions and are confined to the central axis, and unstable solutions, where the oscillation amplitudes increase exponentially. The stable and unstable regions for confining ions to the y-axis are shown in Figure 4.1, here the x-axis is defined as positive going in the Mathieu equation and the z-axis is defined as negative going.

The ratio $a/q$ is equal to $2U/V$ and is independent of mass, this is shown as the "operation line" in Figure 4.2. At constant $a/q$ ratio all masses lie on this operation line, with heavier masses lying closer to the origin ($m_3 > m_2 > m_1$). On altering $U$ and $V$, but keeping the ratio $a/q$ constant, the locations of the mass loci move along the operation line and through a stability region. Changing the range of masses that are confined allows the linear quadrupole trap to be used, in a popular mode, as a mass filter. Increasing the DC voltage, and therefore the ratio of $a/q$, decreases the

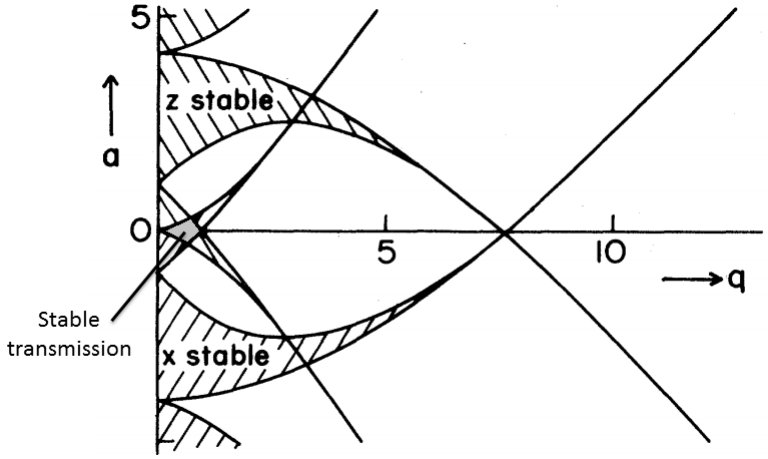


**Figure 4.1:** Stable regions of a quadrupole trap determined using the Mathieu equations. Confinement is achieved when both transverse directions (x and z in this case) are stable [63].

range of confined masses and provides better mass resolution as the operation line moves towards the tip of the stable region. If, however, no DC voltage is applied, $a = 0$, then the operation line lies on the q-axis and is stable between $0 < q < q_{max}$. The linear quadrupole trap is thus stable for masses $m > m_{min}$ and acts as an ion guide (or a high-pass mass filter) [63].

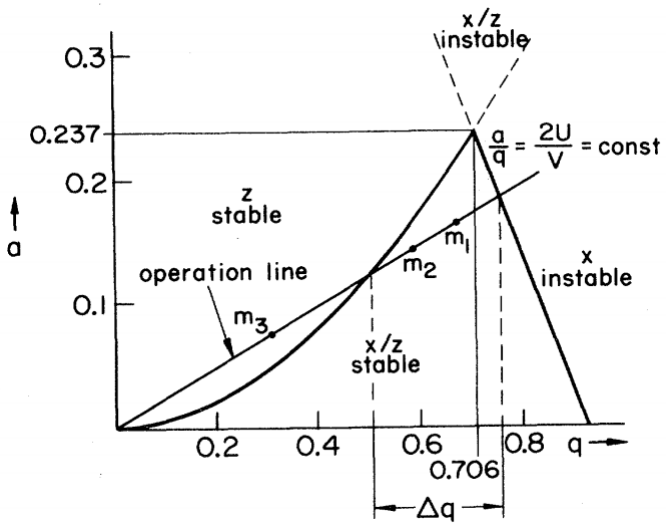


**Figure 4.2:** Operation of a quadrupole trap as a mass filter and the transmission range according to the Mathieu equations. Different masses lie on the operation line, those that fall outside the stable region are lost in collisions with the trap walls [63].

### 4.1.1 The IGISOL Cooler-Buncher

The Cooler-Buncher [11] is a gas-filled variant of a linear quadrupole trap, which is mounted on a high voltage platform (Figure 4.3). Incoming ions with energies close to, but higher than, the platform potential are decelerated and injected into the Cooler-Buncher by use of an electrostatic lens system. The quadrupole trap consists of four stainless steel rods of radius 1.15 cm (1 cm from central axis) that are split into 16 segments and separated by 0.5 mm to a total length of 40 cm. The segmented quadrupole rods create a potential gradient that transport ions to the exit (within 1 ms), where they can be continuously released or confined and bunched behind a potential wall provided by the end plate (Figure 4.4). The potential wall is removed to extract the ion bunch or can be switched to ground to run in continuous mode.

Upon extraction the ions are guided through a mini-RFQ to separate them from the background gas and avoid collisions upon re-acceleration. The mini-RFQ has a central radius of 1.5mm and consists of four 5 cm long plates, with 6 mm of the plates inside the larger RFQ to avoid field distortion within the transition region. The plates have the same phase and frequency as their larger RFQ counterparts, but have a smaller amplitude given by,

$$V' = \frac{r_0'^2}{r_0^2} V$$

where $r_0$ and $V$ are the large RFQ rod radii and voltage amplitude and the primed variables are the equivalent mini-RFQ properties.

Inside the Cooler-Buncher the ions are thermalised in a helium buffer gas by viscous interactions (primarily induced dipoles in the buffer gas) thus reducing their energy spread and emittance. The energy spread of trapped ensembles reduces to less than 1 eV, but is limited by the stability of the HV-platform and the time

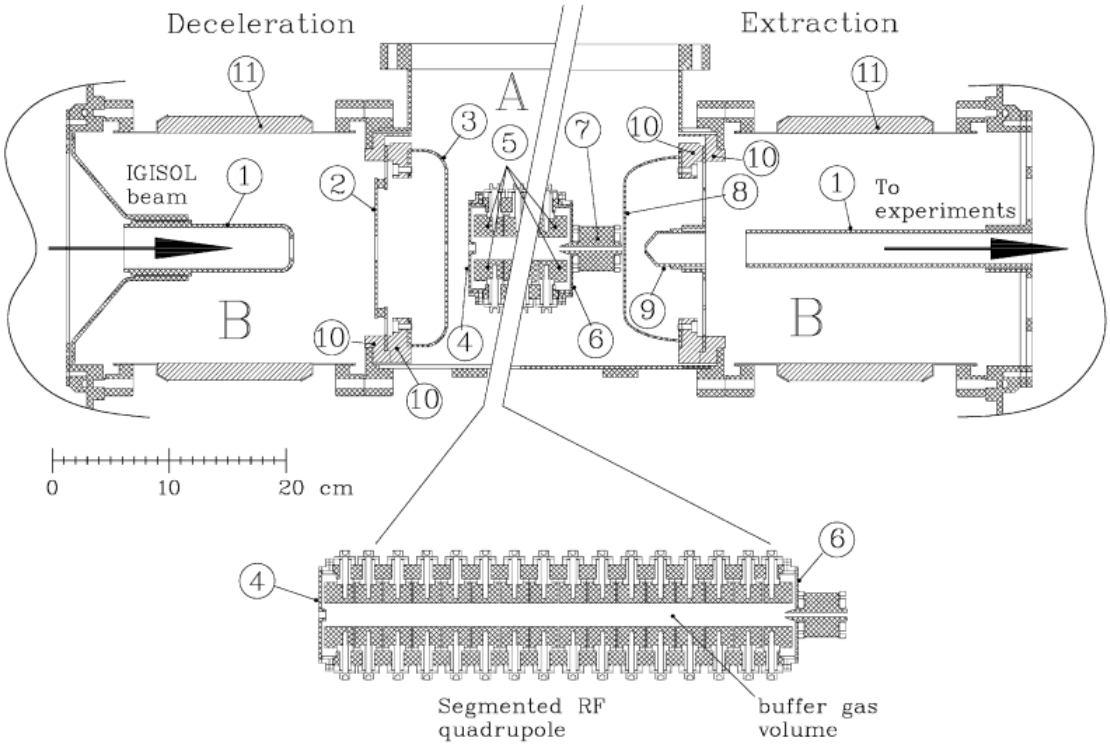


**Figure 4.3:** Electrode configuration of the Cooler-Buncher and the low and high vacuum regions (A and B): (1) ground electrode, (2) first deceleration electrode, (3) second deceleration electrode, (4) third deceleration electrode, (5) RF quadrupole rod segments, (6) end plate, (7) mini-quadrupole rods, (8) extraction plate, (9) extraction electrode, (10) insulator rings, (11) high voltage insulators [11].

taken for the potential wall to drop upon extraction. The released ions have kinetic energies lower than that with which they entered the Cooler-Buncher due to net energy lost during the cooling process.

At IGISOL 3 the Cooler-Buncher was initially tested with and without the mini-RFQ, where the end-plate aperture was used as a skimmer electrode when the mini-RFQ was removed. The bunch length without the mini-RFQ was $\sim$2.2 $\mu$s compared to $\sim$5.1 $\mu$s (FWHM), however this was only achieved at the cost of a greater energy spread of up to 10 eV. The transport time through the mini-RFQ added an extra 30 $\mu$s to the time of flight of the ion bunch (95 $\mu$s total), compared to the 65 $\mu$s time of flight without it (Figure 4.5).

The optimum helium pressure required in the Cooler-Buncher depends on whether

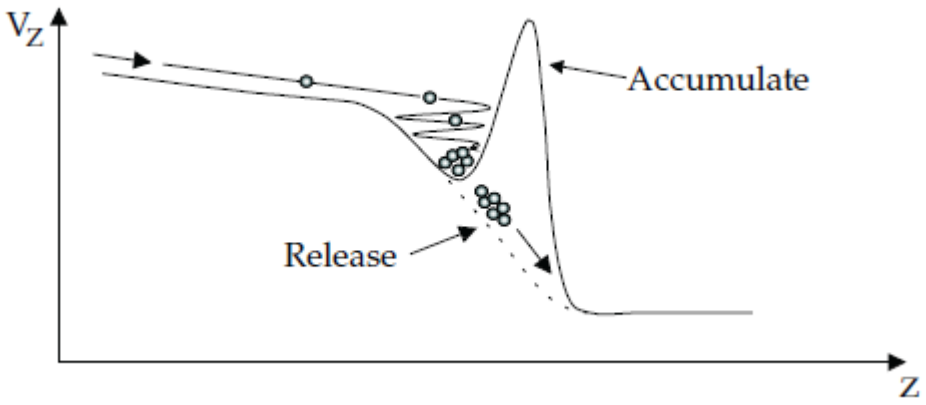


**Figure 4.4:** Diagram illustrating the axial potential inside the Cooler-Buncher and the bunching of the ions before release.

it is in continuous or bunching mode. During ion bunching, a low pressure is required due to the increased interaction time and the need to reduce molecular formation. The typical injection vessel pressures for the bunching and continuous modes are $\sim 0.1 - 1$ mbar and $\sim 2 - 3$ mbar respectively.

## 4.2 Penning trap

The confinement volume of a Penning trap [64, 65] is formed of an axial electrostatic quadrupole field and a linear magnetic field. Confined ions in a Penning trap oscillate axially due to the axial component of the quadrupole field and the combination of the magnetron motion, caused by the radial repulsion of the electrostatic quadrupole, and the cyclotron motion, caused by the linear magnetic field. The resultant motion confines the ions radially in a epitrochoid motion about the traps centre.

Buffer gas cooling in a Penning trap [66] can be used to damp the amplitude of the axial oscillation and the radius of the cyclotron motion. However, the radius of the magnetron motion is increased due to the repulsion of the electrostatic quadrupole (Figure 4.6(a)). Application of a small rf-oscillation at the ions cyclotron frequency counteracts this effect and permits a reduction in the magnetron radius with cooling

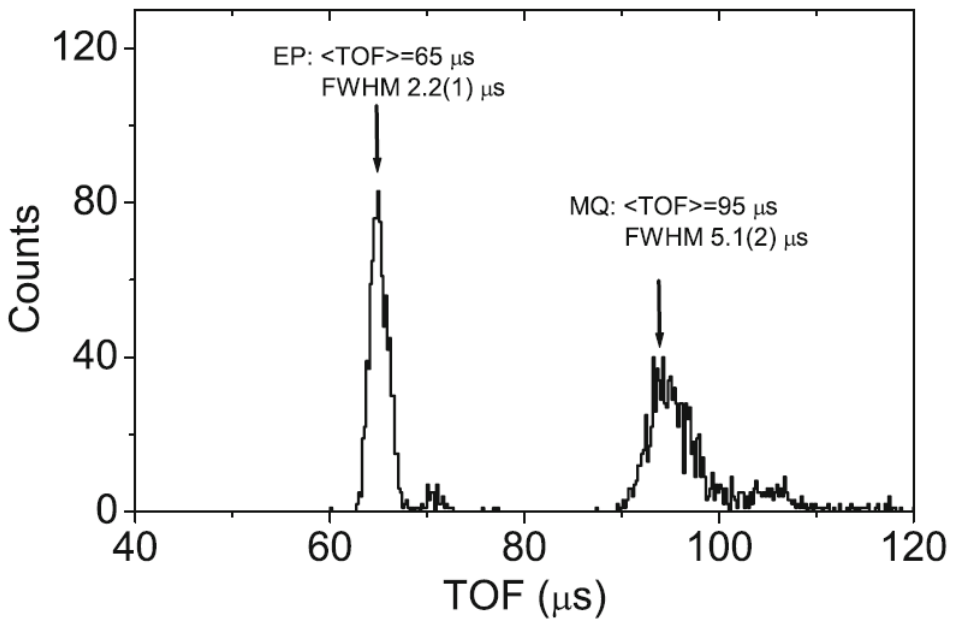


**Figure 4.5:** Bunch lengths upon release from Cooler-Buncher. Secondary peaks are from delayed ions that have formed molecules with contaminants in the Cooler-Buncher buffer gas. Ions were extracted using the end plate (EP) as a skimmer electrode or with the mini-RFQ (MQ) [58].

(albeit with the cyclotron radius reducing at a decreased rate, Figure 4.6(b)).

As the cyclotron frequency is mass dependent, only ions of a particular mass are drawn towards the center, while others move to increasingly larger radii. The Penning Trap can therefore be used to mass separate ions and provide both mass measurements and pure beams for spectroscopy experiments. The Cooler-Buncher cools ions prior to injection into the Penning trap and therefore buffer-gas cooling is not required for the IGISOL Penning trap. All ions are instead kept at a larger, fixed radius before the isotopes of the correct mass are guided towards the center using the rf-oscillations.

### 4.2.1 JYFLTRAP

The double Penning trap at the IGISOL facility [67–69] uses one Penning trap for mass separation, with a mass resolving power of $\frac{M}{\Delta M} = 10^5$, and the other for precise mass measurements ($> 10^6$ resolving power). Ion bunches from the Cooler-Buncher

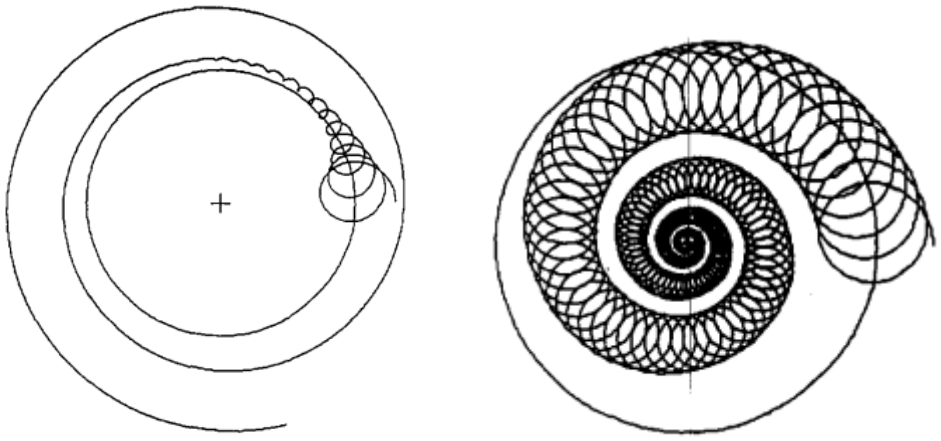

(a) Magnetron radius increase and cyclotron radius decrease due to cooling of ions.

(b) Magnetron and cyclotron radius reduction due to an applied rf-oscillation.

**Figure 4.6:** Buffer gas cooling and rf-oscillations of ions in a Penning Trap. [66]

are injected into the Penning Trap by the lowering and raising of the injection trapping potential. The central electrode is azimuthally segmented so that the ions can be excited into larger orbits, after which the rf-quadrupole field is applied and the ions of the desired mass are drawn towards the center for extraction or mass measurement [67]. The pressure in the JYFLTRAP is maintained at $\sim 10^{-8}$ mbar.

# CHAPTER 5

# ConeTrap

The ConeTrap is an electrostatic ion trap originally developed by the group of Henning Schmidt at Stockholm University [70, 71]. The use of conical containment electrodes can be traced earlier to, for example, Knight [72]. In all cases ions are reflected back and forth between two cone shaped electrodes (Figure 5.1). The potential within a conical electrode is harmonic both axially and radially and therefore guides ions back into the trap and towards the central axis, thus containing the ions. Ions are dynamically trapped and injected into the ConeTrap by the lowering and raising of one of the cone electrode voltages. Whilst a central chamber is not a requirement for trapping, the electrode discs in front of the cone electrodes are essential to form the harmonic potentials and to screen the trap from the changing cone electrode potentials and prevent them from affecting the ion kinetic energies upon injection or extraction (drift-tube effect). A potential can also be applied to the central chamber to reduce the mean velocity of the contained ions. This is useful for tuning the acceptance time of the ConeTrap or Doppler shifting the ions into resonance with an axial laser beam. Slower ions will, however, diverge more in the ConeTrap due to the emittance of the injected beam (see Appendix A). The ConeTrap is of interest to the laser-IGISOL group as a means of trapping the ions in vacuum for optical studies (as suggested by Schmidt et al. [71]). The great advantage of the ConeTrap compared to other ion traps is its simplicity, compact nature

and accessibility for "line of sight" optical spectroscopy.

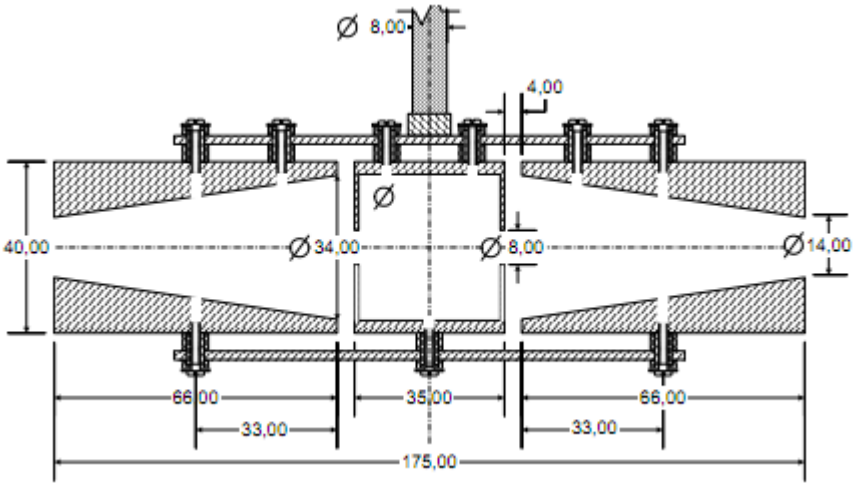


**Figure 5.1:** Original ConeTrap used by A. Fardi. All dimensions are in mm [70].

The operation parameters of the IGISOL require that the ConeTrap have an acceptance time of at least 10 $\mu$s. The spectroscopic application requires an extensive, well-defined central region for optical pumping. Generally, experimental considerations require close to 100% injection and extraction efficiency and containment times of order $\sim$ 10 ms. These parameters were investigated using an ion-optical design and simulation program, SIMION.

## 5.1 Simulation Program: SIMION

To investigate the feasibility of using a ConeTrap on the IGISOL line the charged-particle optics simulation program SIMION [73] was used. SIMION calculates charged-particle trajectories through electromagnetic fields. With respect to the terminology used in the package, the desired electric and magnetic components are modeled in potential arrays (PA), instances of which are placed inside an ion optics workbench (an .IOB file) to form the complete experimental set-up or beam-line.

Electric and magnetic PAs are created separately, however magnetic PAs were not required for these studies. The PAs are created using 2D or 3D grids with

plotted electrode and non-electrode points. Planar and axially symmetric PAs can be automatically constructed; essential for 2D electrode maps. The potentials at each non-electrode point are calculated by solving the Laplace equation using finite-difference methods; referred to as "refining" the potential array. There are two types of potential array electrode maps; $.PA$ and $.PA\#$. In $.PA$ files the potentials are calculated for the voltages specified in the electrode map. In $.PA\#$ files the electrodes are labeled numerically and solutions are calculated for each separately. The total potential at each non-electrode point is then a linear combination of these solutions, thus allowing the electrode potentials to be adjusted during simulations. A scaling factor can be applied to the PAs when loaded into the workbench to acquire instances at different resolutions, allowing more complex or sensitive areas to be calculated with greater accuracy.

When running a simulation, the entire workbench is kept in the computer memory, regardless of what instances are being used. For this reason the SIMION package can be RAM intensive which can lead to slower simulations. There are several methods that can be used to reduce the RAM usage. Symmetry can be used to reduce the size of PA files, several instances of the same PA can be loaded into the workbench, and larger, less complex or sensitive PAs can be created at lower resolution. Also, an instance from a $.PA$ file is less RAM intensive than one from a "fast-adjustable" $.PA\#$ file, at the cost of flexibility.

User programs can be used to change electrode potentials, ion properties and to collect data during simulations. The files have the same name as the relevant PA or workbench they apply to and consist of several segments. Figure 5.2 shows a simplified flow chart of the order of the SIMION user program segments when ions are released. The figure shows that all ions are created together, then flown consecutively, and then terminated. This grouping of the ion segments allows data to be collected for all ions in each stage, but increases the demand on the RAM.

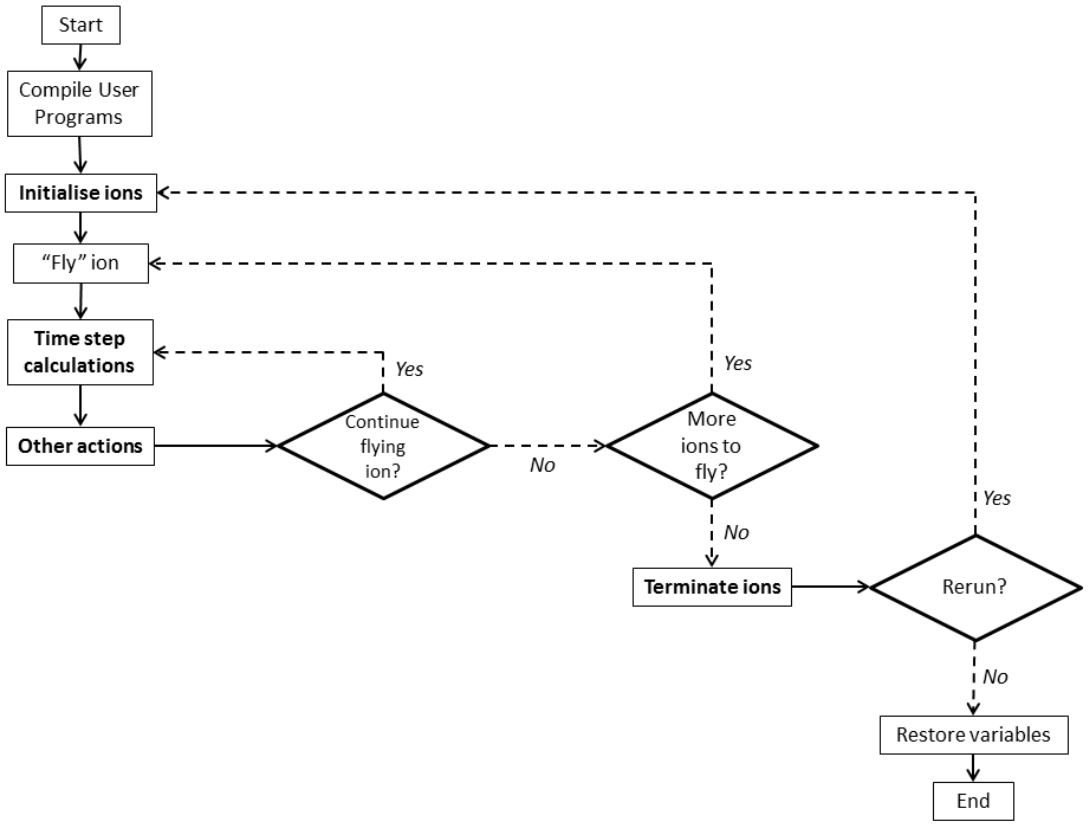


**Figure 5.2:** Simplified SIMION segment order. Sections in bold are segments in which user programs can be called.

The ConeTrap modeling has, throughout this chapter, been acquired in simulations using 800-eV ions with 100-u mass and at a 10-$\mu$s uniform bunch length. The ConeTrap modeled has the same dimensions (shown later in Figure 5.17(b)) unless otherwise stated. The IGISOL ion bunch, upon exiting the first quadrupole deflector, has been simulated using 1000 ions, flown separately, randomly emitted within a 1-mm radius and 0.135-degree half-angle spread (giving an emittance of $3\pi$ mm mrad). This ensemble is then focused, onto the approximate position of the Faraday cup in the real beam-line (Section 3.8), by the Einzel lens detailed in Section 3.8.2. All ions contained for at least 1 ms were counted as stable in the trap and a 'test bunch', with three times the radius and angular divergence of the simulated IGISOL beam, was used to observe in greater detail the stable regions of the various ConeTrap designs.

## 5.2 ConeTrap design

This section details the simulations which formed the design of the IGISOL ConeTrap. The properties of the stable regions are discussed and the benefits of using a ConeTrap with asymmetric potentials presented. Explanations for the form of the stable regions are then given, followed by the design of the ConeTrap with considerations for the injection and extraction of ions, the required acceptance time and the formation of an extensive central region of uniform potential (for optical pumping).

### 5.2.1 Stable regions

Symmetric ConeTraps, where both cone electrodes have the same voltage, have two stable regions; the low voltage (LV) and high voltage (HV) modes (shown in Figure 5.3(a), with a more detailed plot of the LV stable mode shown in Figure 5.3(b)).

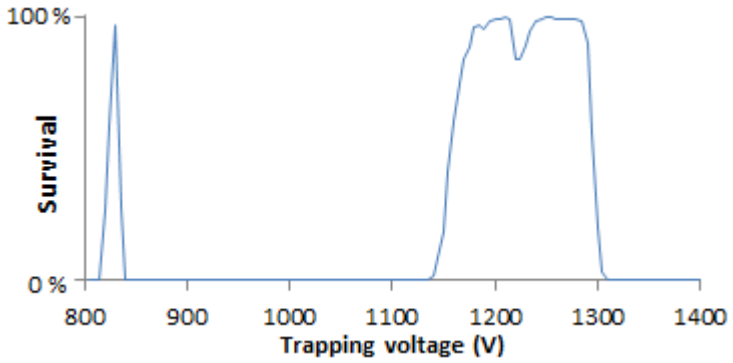


(a) Both the LV and HV stable regions.

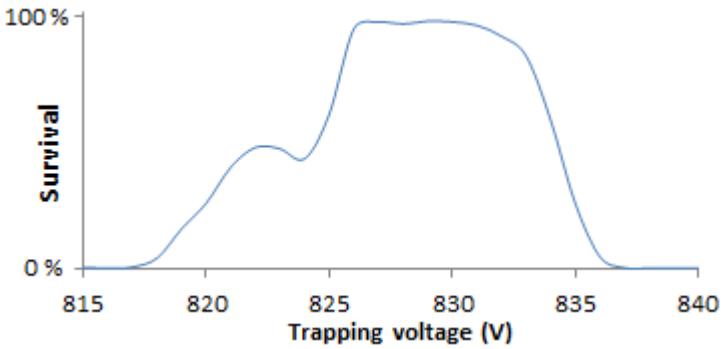


(b) Higher resolution plot of the LV stability region.

**Figure 5.3:** Symmetric ConeTrap stable regions for the 'test' simulated ion bunch.

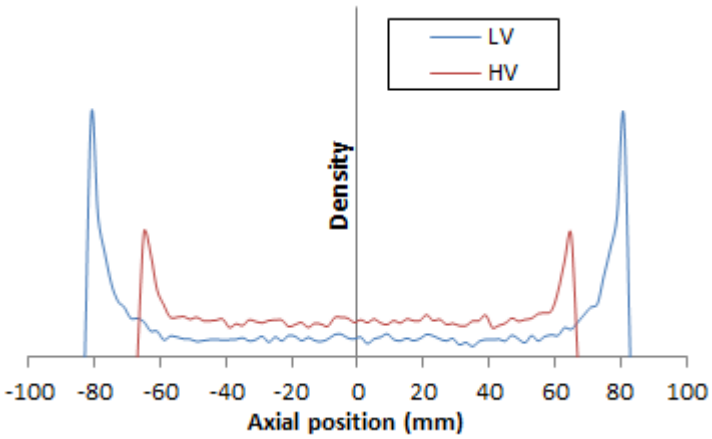


**Figure 5.4:** ConeTrap axial position densities for symmetric LV (830 V) and HV (1250 V) ConeTraps. Simulations used 10,000 ions.

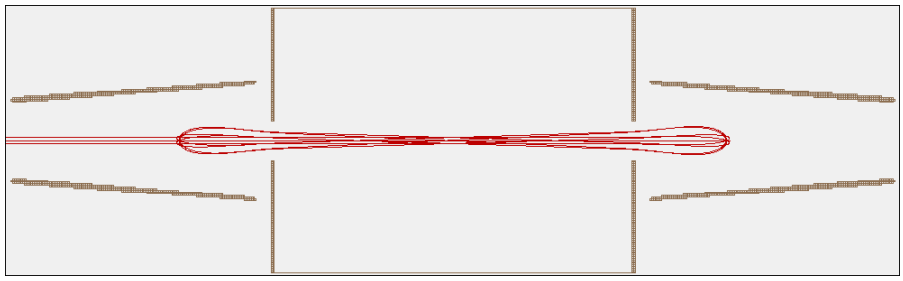

(a) LV ConeTrap orbital shape (focused LV potentials).

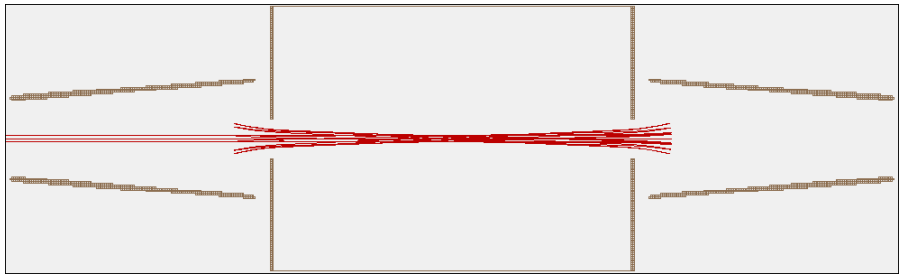

(b) HV ConeTrap orbital shape (focused HV potentials).

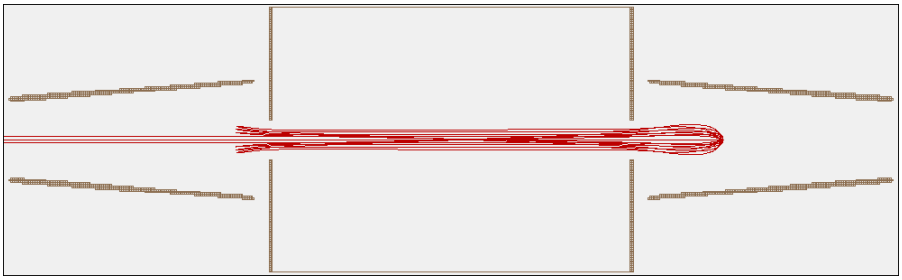

(c) Asymmetric ConeTrap orbital shape (parallel HV and LV potentials).

**Figure 5.5:** Symmetric and Asymmetric ConeTrap orbital shapes.

Ions in an LV ConeTrap move in slow arcs around the inside of the cone electrodes ("soft reflection"), as shown in Figure 5.5(a). The motion results in the ion plume bunching at either end of the ConeTrap, shown by the peaks in axial ion density in Figure 5.4. This bunching is due to the time the ions spend in the cone electrodes and does not result in any time compression upon release of the ions. The path of the ions through the LV cone electrode depends on their energy and entrance trajectory, which causes variations in the reflection times. The position density of the simulated ion bunch was observed to homogenise around the ConeTrap within a few milliseconds.

Ions in an HV ConeTrap are sharply reflected back out of the cone electrodes ("hard reflection"), as shown in Figure 5.5(b), resulting in the ion density being spread more evenly across the ConeTrap than in a LV ConeTrap (Figure 5.4). Due to the low variation in reflection time it takes >10 ms for the simulated IGISOL ion bunch to homogenise around the HV ConeTrap.

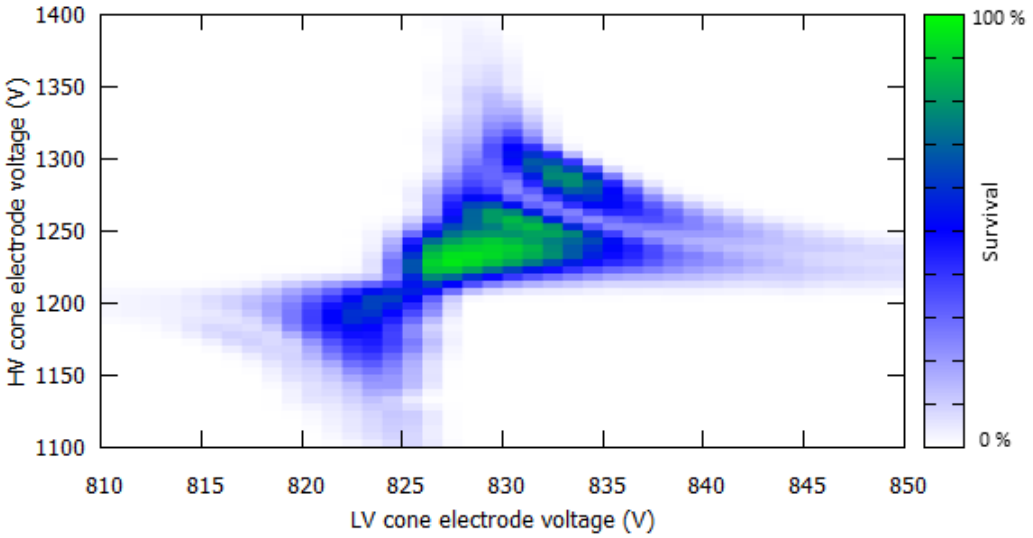


**Figure 5.6:** Asymmetric ConeTrap stable regions for the 'test' simulated ion bunch.

Two known disadvantages with using a symmetric LV ConeTrap are the high ion densities in the LV cone electrodes and the loss of ions upon extraction due to the "drift-tube effect", where the ion energies are altered with the changing poten-

tial. The fast reflection within the HV cone electrode results in a lower ion density and, consequently, reduced ion losses upon extraction. An HV ConeTrap's acceptance, however, is much less than that of an LV ConeTrap due to the time difference between the fast HV reflection and the slow LV reflection (see Table 5.1). An asymmetric ConeTrap that uses the HV cone electrode for *both* injection and extraction takes advantage of the low ion density of the HV reflections and the high acceptance of the LV reflections and is preferable to either symmetric mode. The orbital shape, stable regions and axial ion density of the asymmetric ConeTrap are shown in Figures 5.5(c), 5.6 and 5.7 respectively. For a standard simulation it takes just under 10 ms for the IGISOL beam to homogenise around the asymmetric ConeTrap.

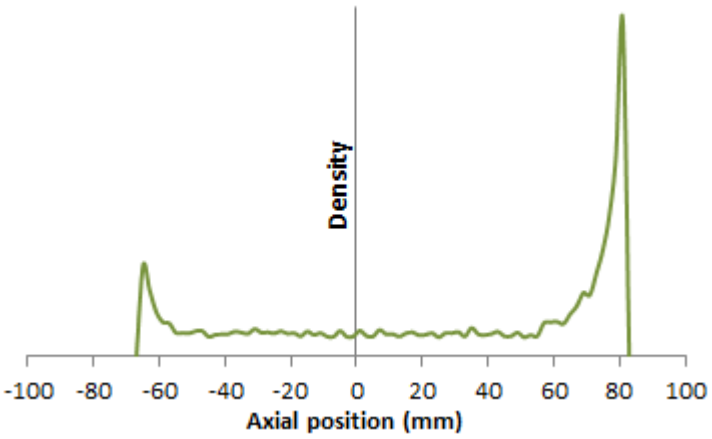


**Figure 5.7:** ConeTrap axial position densities for an asymmetric ConeTrap. Simulations used 10,000 ions and HV and LV cone electrodes of 1250 V and 830 V respectively.

Table 5.1 shows the average time it takes an ion to enter and exit the cone electrodes in the LV and HV ConeTraps. The reflection times are independent of ConeTrap length, however the stable regions contract with increased length and not all voltages provide stable orbits (eg: 815 V is unstable for LV ConeTraps with central chambers of length >60 mm. See Section 5.2.4).

| LV (V) | time ($\mu$s) | HV (V) | time ($\mu$s) |
|---|---|---|---|
| 805 | 13.33 | 1000 | 2.64 |
| 810 | 9.63 | 1050 | 2.41 |
| 815 | 8.01 | 1100 | 2.25 |
| 820 | 7.03 | 1150 | 2.12 |
| 825 | 6.37 | 1200 | 2.02 |
| 830 | 5.87 | 1250 | 1.94 |
| 835 | 5.49 | 1300 | 1.86 |

**Table 5.1:** Average reflection times for the LV and HV cone electrodes. The "reflection time" was taken 15 mm from the aperture of the cone electrode (to uniformly account for fringe field effects).

### 5.2.2 Properties of stable regions

The ConeTrap is a purely electrostatic device and the form of the potentials is determined by the electrode shapes, which do not change. Only the magnitude of the cone electrode potentials determine which values of $E_{ion}/q$ stability will be formed. The change in the type of reflection the ions experience with increasing electrode potential arises from the changing relative magnitudes of the axial and (divergent and convergent) radial forces and the decreasing penetration depth of the ions into the cone.

Figure 5.8(a) shows the relationship between ion axial position and *axial* acceleration. When the cone electrode potentials are in the LV stability region the ions penetrate further into the cone electrode and experience the slow tail end of the peak in axial acceleration. The low axial acceleration in this region combined with the low velocities of the ions at this point results in the ions axially bunching. This gives the LV stability region the high acceptance the asymmetric ConeTrap design exploits. Variations of ion velocities in the low acceleration region results in a larger spread of reflection times and the faster homogenisation of the ion bunch (compared to the HV ConeTrap).

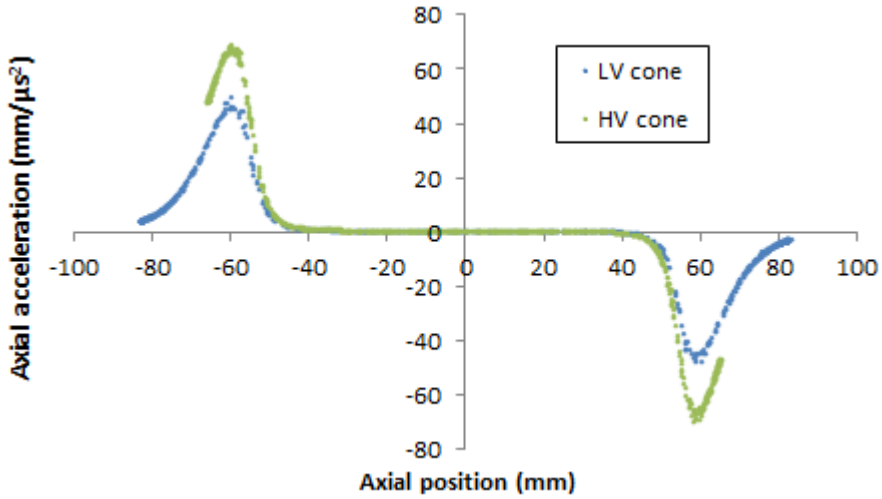


(a) Scatter plot of ion axial positions and accelerations.

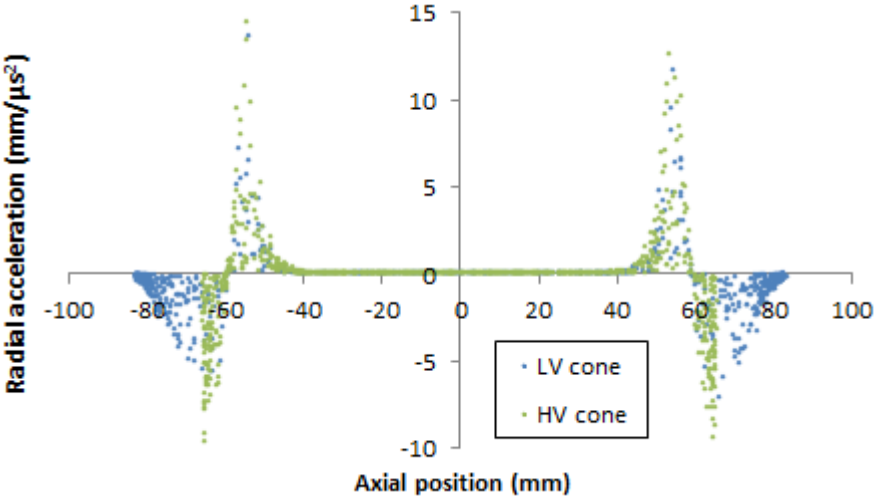


(b) Scatter plot of ion axial positions and radial accelerations.

**Figure 5.8:** Scatter plots of ion axial positions against axial and radial accelerations in typical low voltage (LV) and high voltage (HV) cones.

Figure 5.8(b) shows the relationship between the axial position and *radial* acceleration of ions in the ConeTrap. Ions entering a cone electrode will first experience a radially divergent force due to the fringe fields, followed by a convergent force due to the shape of the (cone) electrodes. The penetration depth in the LV reflection ensures that ions experience more of the convergent radial acceleration. This results in the path of the ions forming the arc shapes shown in Figure 5.5(a). The radial acceleration reduces the further the ions penetrate into the cone and the ensemble

is radially bunched, as well as axially bunched, as the ions pass through the central axis. Ions contained in a HV ConeTrap experience much larger radial forces. Following some divergence from the fringe fields, ions in a HV cone electrode experience a strongly convergent radial force proportional to their radial position and are reflected back in almost exactly the direction in which they entered, as shown in Figure 5.5(b).

The stable regions of the ConeTrap are at those potentials which result in a focused or parallel reflected (output) beam. This is illustrated in Figure 5.9, which shows the change in the output trajectory with increasing cone electrode potential. The ions are divergent upon exiting the cone electrode at potentials slightly above the ion energy (below the LV stability region). As the cone electrode potential is increased (with respect to the ion energy) the path of the ion is folded back through the injection point, becomes parallel with the injection axis and then becomes divergent again. The potentials that provide convergent and parallel ion paths form the LV stability region. Continuing to increase the potential then folds the ion trajectory back towards the injection point to form the HV stability region. The change in output position and angular deviation (emittance) with increasing cone electrode potential for the simulated ion bunch is shown in Figure 5.10.

The density of data points along the locus in Figure 5.10 indicates that the rate of change of the output emittance decreases with increasing cone electrode potential. This is due to the change in penetration depth of ions into the cone electrode. The penetration depth at low potentials changes rapidly, resulting in large shifts in the output trajectories and reflection times (Table 5.1).

The shapes of the stable regions arise from the stability of the focused and parallel output trajectories in the ConeTrap. This is dependent on the geometry of the ConeTrap and results in broad structures in the stability regions; primarily from focused and parallel orbits. Configurations forming parallel orbits are more

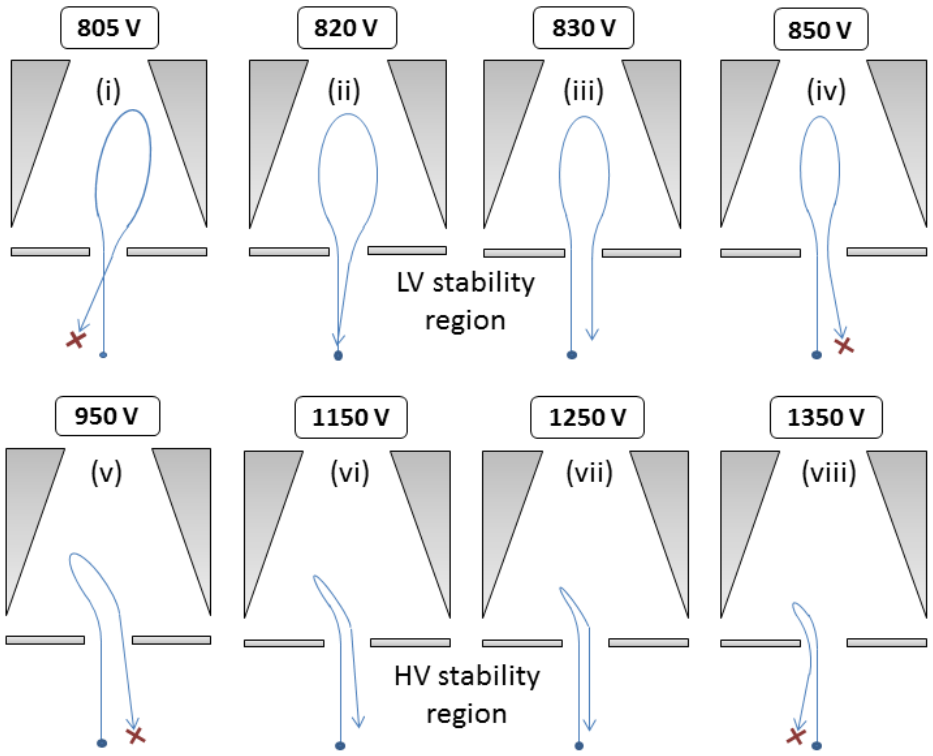


**Figure 5.9:** Illustration of the reflection path of an 800 eV ion by a cone electrode at increasing potentials.

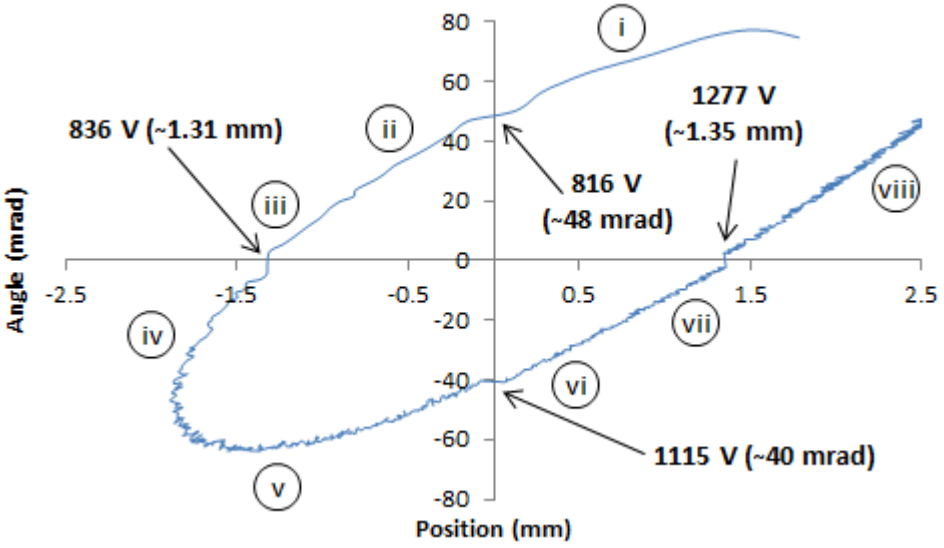


**Figure 5.10:** Variation of output emittance with cone electrode potential. Points were collected 15 mm from the entrance aperture for cone electrode potentials from 805 V upwards in 1 V increments. The initial divergent output beams at ~810 V were taken to be positive with subsequent data points plotted relative to these. The labels indicate the conditions illustrated in Figure 5.9.

stable due to their smaller angular divergence compared to focused orbits. The lower velocity spreads in such orbits act to reduce Doppler broadening in spectral applications and are of particular interest in this work.

The output trajectories of reflected ions differ depending on the input trajectory, with the most desirable input beam being spatially similar to the output beam produced. For an asymmetric ConeTrap to be stable, both the LV and HV cone electrodes are required to provide similar reflections to avoid large variations in the ion orbit around the ConeTrap. This can be achieved by setting the trapping potentials to voltages that are 180° apart on the ellipse shown in Figure 5.10. The emittance of the injected beam also needs to "match" the trapping potential reflections. A beam weakly focused into the back cone electrode is required for the IGISOL ConeTrap and experimentally this is ensured by focusing the beam onto a Faraday cup placed behind the, initially grounded, ConeTrap.

### 5.2.3 Dynamic injection and extraction

When the injection and extraction cone electrode switches between the open and trapping voltages, the change occurs in a finite time period and any ions moving within the cone or experiencing the fringe field will suffer from a "drift-tube effect" and have their kinetic energies altered. It is possible to inject and extract ions using a grounded cone electrode, however, setting the injection-extraction voltage as high as possible reduces the amount of kinetic energy gained or lost upon switching, specifically in the fringe field. A high injection voltage also means a smaller step up to the trapping voltage, which can be done faster than a switch up from ground, and a smaller current passing through the transistor when switching down.

The ion transit through two cone electrode designs, set from ground to the acceleration voltage ($V_{acc} \simeq 800$ V), were modeled to determine the optimal injection voltage. The transmission through these cone electrodes and a 3 mm exit aperture

(that experimentally corresponds to a Faraday cup) is shown in Figure 5.11. An initial focusing of ions is observed at $\sim 0.5V_{acc}$ and, following this maximum, a sharp increase in efficiency is observed above $0.9V_{acc}$. This "injection peak" provides 100% stability for the simulated IGISOL ion bunch, upon injection into the active ConeTrap, and is exploited to minimise the drift tube effect and switching requirements. The form of the transmission efficiency, with increasing cone electrode voltage, can also be used as an important confirmation of the accuracy of the modeling and to provide parameters for commissioning strategies (discussed in Section 5.3.3).

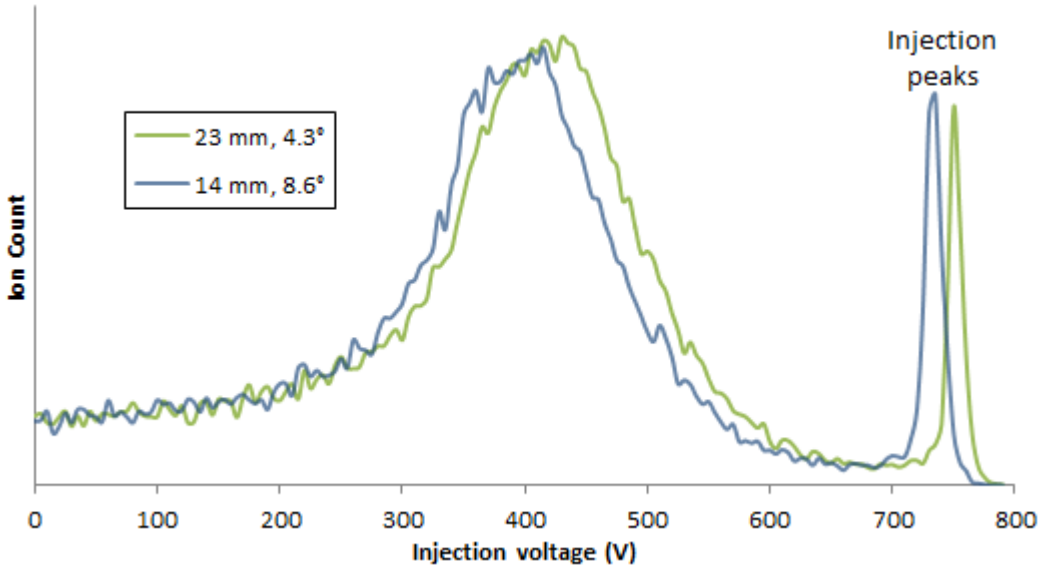


**Figure 5.11:** Injection efficiency for the two simulated cone electrode designs; angles and outer apertures of 8.6°, 14 mm and 4.3°, 23 mm respectively.

The two cone electrode designs have angles and outer apertures of 8.6°, 14 mm and 4.3°, 23 mm respectively. Both designs provide stable injection of the simulated ion bunch, however the latter dimensions were found to provide a smaller average radius for extracted beams (Figure 5.12(a)) and improved the extracted yield by ~2%. The "injection peak" of this cone electrode structure provides 90% extraction efficiency with 80% of all ions surviving with little alteration to their kinetic energy (<0.1 eV).

A grounded housing, including front (and back) disc electrode(s), can be used

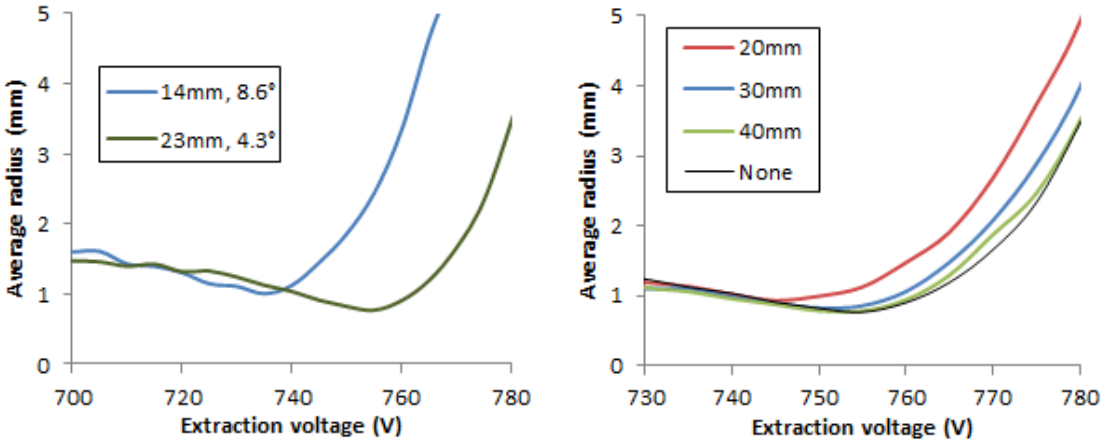


(a) Mean radii of extracted ions for the two cone electrode designs.

(b) Mean radii of extracted ions for different separations of the shield and cone electrodes.

**Figure 5.12:** Average radii of extracted ions for the two simulated cone electrode designs, which have angles and outer apertures of 8.6°, 14mm and 4.3°, 23mm respectively, and for a shielded extraction electrode. Smaller average radii are acquired at the upper edge of the injection efficiency peak.

to avoid the voltage switch affecting ions as they approach or leave the ConeTrap. A disc electrode of 80 mm diameter and 12 mm aperture diameter placed 40 mm from the cone electrode entrance was found to produce only small perturbations compared to an unshielded ConeTrap (Figure 5.12(b)).

### 5.2.4 Acceptance time

The acceptance time of the ConeTrap was defined as the time between an ion exiting the injection cone to reentry following one (partial) orbit of the trap. Over time the ions within the ConeTrap homogenise their orbits and the axial ion position density stabilises. Upon release any ions within the injection-extraction electrode will be lost and the released ion bunch size is thus equivalent to the acceptance time.

The length of the central chamber determines the acceptance time and the efficiency of optical pumping in the ConeTrap. The length of the central region also, however, critically affects the size of the stable regions (Figure 5.13). As the length of the section increases, the lower LV region orbits become unstable and the remain-

ing available potentials result in shorter orbital times (Table 5.1). A 110-mm long central chamber, with a back cone electrode identical to the injection-extraction electrode, was found to provide ∼10-$\mu$s acceptance time.

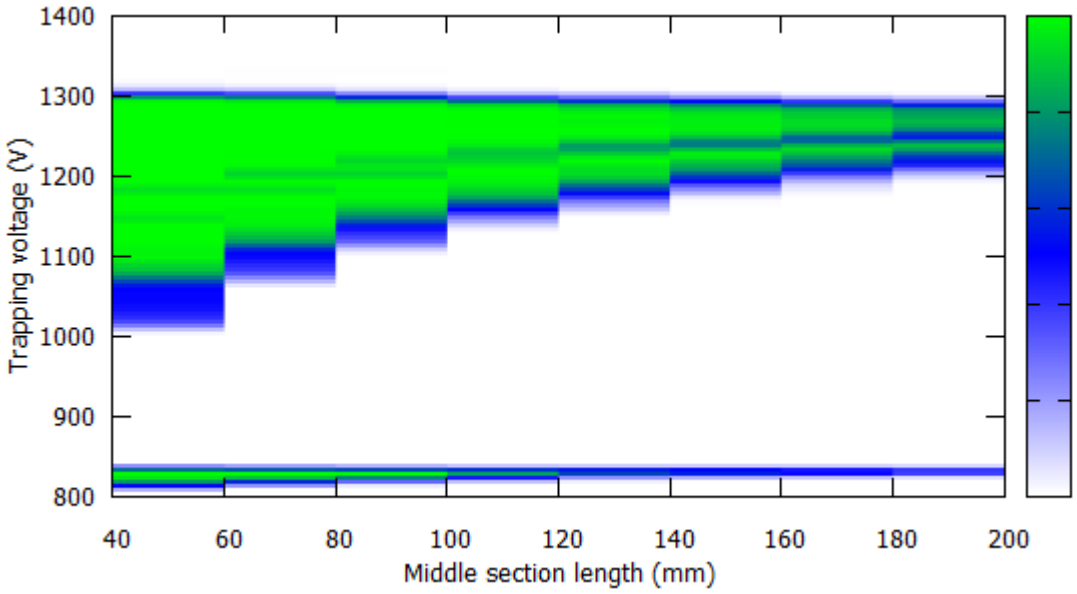


**Figure 5.13:** ConeTrap stability with increasing length of the central section using the 'test' simulated ion bunch.

An alternative way of increasing the acceptance time of the trap is to increase the angle or diameter of the back cone electrode. This increases the penetration depth of the ions into the cone electrode and results in the ensemble experiencing shallower potential gradients, in turn resulting in longer reflection times (and a slight increase in stability due to less divergent output beams). The change in output emittance with cone electrode potential for cone angles of 4.3°, 8.6° and 12.9° are shown in Figure 5.14(a) and their reflections times in Figure 5.14(b). The same increase in reflection time and decrease in angular divergence occurs when increasing the diameter of the cone electrode, however a longer cone electrode is required to maintain the reflecting potential wall at the rear of the cone.

To achieve acceptance times above 20 $\mu$s, a double cone electrode must be constructed. A double cone electrode is used in the design of the (injection-independent) ionisation ConeTrap and is discussed in Section B.2.

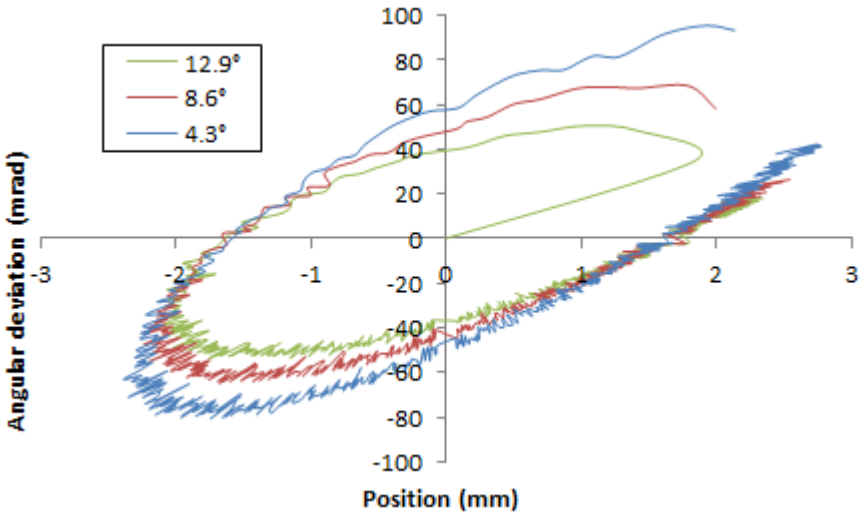


(a) Variation of output emittance.

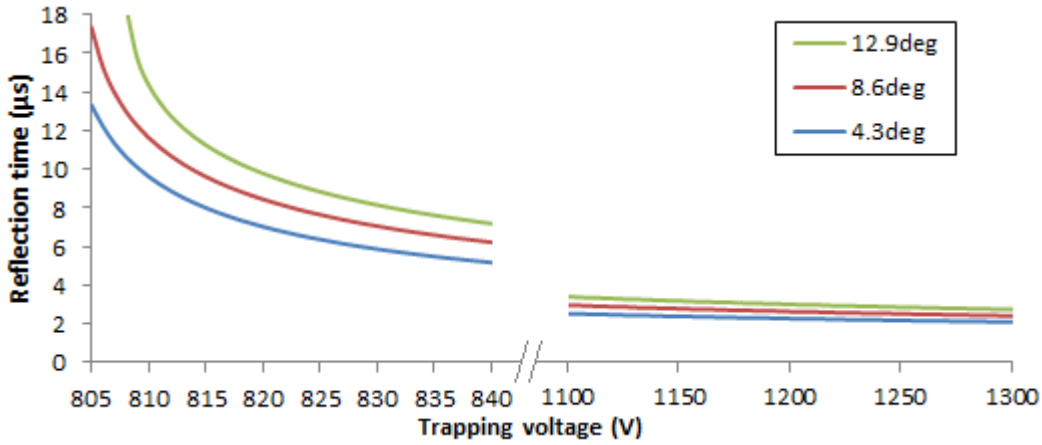


(b) Variation of reflection time.

**Figure 5.14:** Variation of output emittance and reflection time with cone electrode potential for different cone electrode angles. Cone electrode angles were altered by changing the diameter of the cone electrode at the discs.

A ConeTrap using the injection-extraction cone angle of 4.3 degrees and 23-mm outer diameter for both cone electrodes, with a 110-mm central region, has asymmetric stable regions that are 100% stable for the simulated IGISOL beam. In the final design, the required acceptance time was achieved through increased ConeTrap length, therefore providing a larger optical-pumping region, rather than by altering the back cone electrode.

### 5.2.5 Uniform potential region

The fringe fields in the central chamber reduce both the optical-pumping efficiency, as ions are taken off resonance, and the acceptance time, as the field changes upon switching voltage. The extent of the fringe field is determined by the size of the aperture; the smaller the aperture, the less field penetration. The fringe fields can however be rapidly reduced by adding a “lip" to the apertures, shown in Figure 5.15. This small modification allows for greater stability and reduces the effect on the central region.

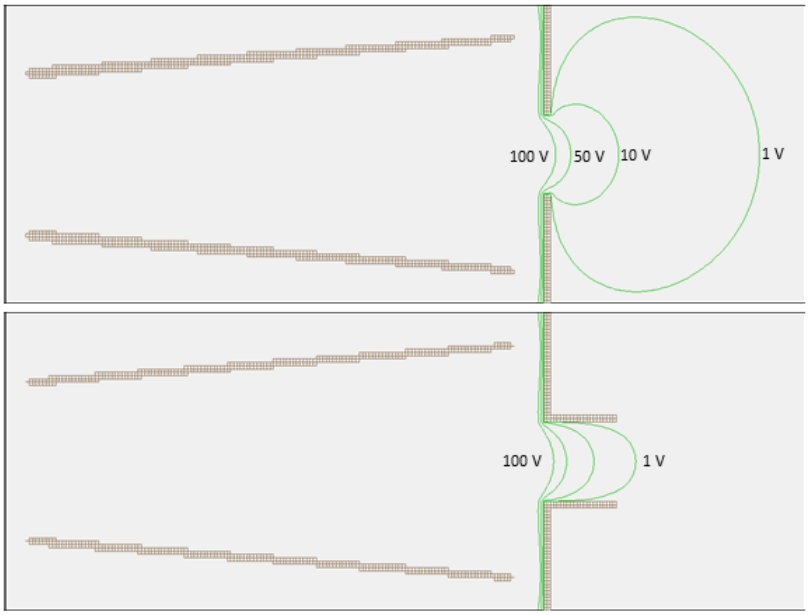


**Figure 5.15:** Fringe field reduction on addition of an aperture lip.

The output emittance of a cone electrode was plotted, with constant input emittance, as a function of trapping potential for different aperture diameters. The plots of the output emittance were identical for each aperture with the only differences being the trapping potential at each point. The stable regions shift upwards with decreasing aperture size and the overall stability of the ConeTrap decreases as divergent ions fail to pass through the smaller apertures. This suggests that the range of stable output emittance profiles is independent of aperture size and is only determined by the input emittance and cone electrode shape. Experimentally larger

apertures will result in a wider orbital waist and a reduced ion density along the central axis due to space charge effects acting to repel ions from one another. This reduction in density results in a loss of axial optical-pumping efficiency (though not an issue if radially pumping), but also has the advantage of a lower ion-ion collision rate and therefore longer containment times.

Aperture diameters of 12 mm were chosen as a compromise between stability and fringe-field penetration. Aperture lips have not been used for the initial IGISOL ConeTrap, but disc replacements are available if smaller apertures or a lip is required (see Section 5.3.1).

## 5.3 Construction and installation considerations

This section describes the construction and commissioning of the IGISOL ConeTrap. The first part discusses the materials chosen for the construction of the ConeTrap, with considerations for strength and vacuum properties, followed by the design of the fast-switch circuitry needed for the dynamic trapping of the ion bunches. The commissioning considerations and results for the IGISOL ConeTrap are then presented, followed by a description of the loss mechanisms within the trap.

### 5.3.1 Physical construction and materials

To facilitate manufacture, the ConeTrap central chamber was made from two discs, with apertures, held together by stainless steel rods and surrounded by a honeycomb mesh. The honeycomb mesh allows laser access to radially pump the ions and the use of discs allows the ConeTrap length to be easily altered (and the discs themselves can be easily replaced to change the apertures). To avoid fringe-field effects the discs were made with as large a diameter as possible (80-mm diameter in a 100-mm diameter pipe). The effect of the disc diameter on the fringe field is shown in Figure

5.16.

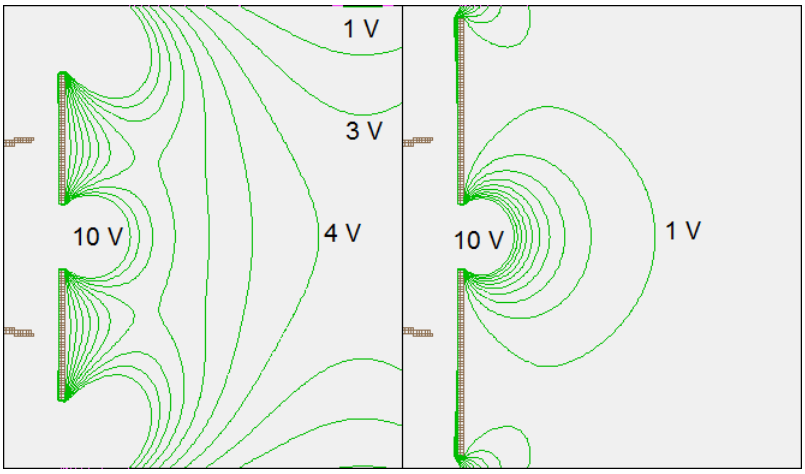


**Figure 5.16:** Fringe fields due to different disc diameters. Shown are the fringe fields created by 1000 V symmetric ConeTraps with 60 mm diameter discs (left) and 80 mm diameter discs (right). The calculation does not include the effect of the honeycomb mesh that would surround the ConeTrap central region.

Figure 5.17(a) shows a model of the IGISOL ConeTrap. The ConeTrap is suspended in high vacuum by four rods connected to a mounting flange. These rods can be made from an insulator if a charged central section is required, however steel rods, and grounded discs, are preferable as the ConeTrap is heavy (and requires strong supports to reduce the cantilever). A honeycomb mesh surrounds the central section, limiting fringe-field effects from the cone electrodes and shielding the voltage feed of the injection-extraction electrode, while still allowing access for radial pumping or detection of outgoing radiation. Insulators attach the cone electrodes to the discs and the mounting flange has two feed-throughs for the two cone electrodes and a third for other applications. The flange also has a central port for installation of a window for optical pumping or a Faraday cup (for commissioning purposes).

To achieve high vacuum a ConFlat flange (sealed with a copper gasket on a knife edge) and low out-gassing materials were used. Copper was used for the electrodes, stainless steel for the support rods and PEEK (Polyether ether ketone) for the insulators. PEEK was chosen as the insulator due to its insulating and vacuum properties and also its strength, as it needs to hold the cone electrodes rigidly in

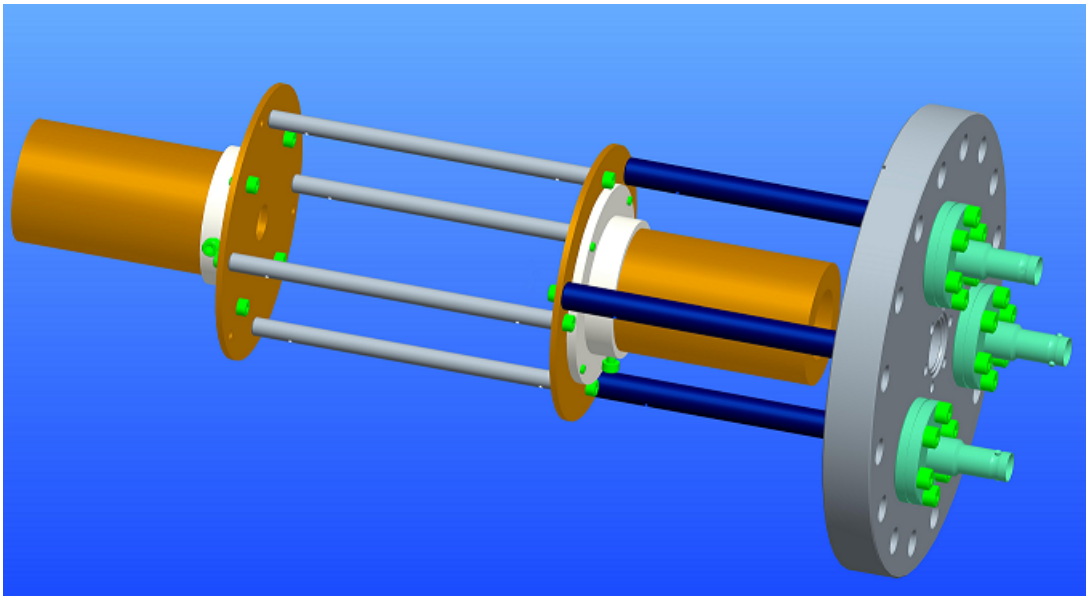

(a) Model of the ConeTrap and mounting flange.

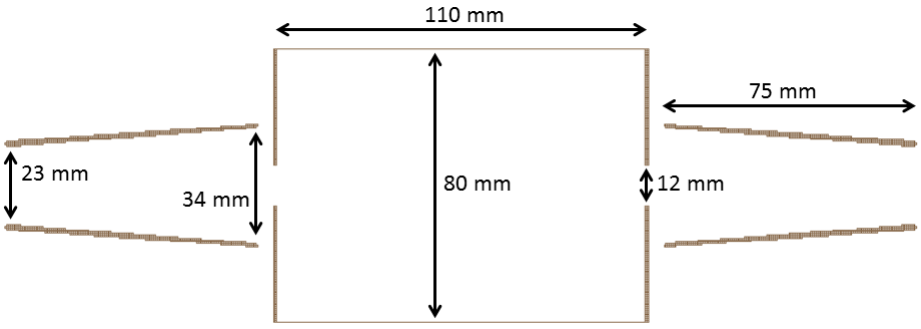


(b) Dimensions (in mm) of the ConeTrap.

**Figure 5.17:** Model and dimensions of the constructed IGISOL ConeTrap.

place. The ConeTrap can be baked in vacuum to remove any water vapour from the materials and reduce their out-gassing to achieve a base pressure beneath $10^{-7}$ mbar.

The dimensions of the final ConeTrap design are shown in Figure 5.17(b).

### 5.3.2 Fast-switching circuitry

The injection-extraction electrode must be able to switch rapidly between voltages to efficiently trap the ion bunch and to avoid altering the kinetic energies of outgoing ions upon release. The circuitry designed for this is shown in Figure 5.18. A ST Microelectronics 4N150 MOSFET is used to temporarily engage a resistive divider.

The device can tolerate a maximum current of 4 A and a maximum voltage of 1500 V. The gate control is provided by a micro-controller (Arduino) which sends a 5-V pulse into a gate driver that amplifies the pulse to the 12−18 V required to fully activate the MOSFET. Three 2 kV, 100 nF capacitors provide the instantaneous current needed to overcome the capacitance of the cone electrode and enables the use of continuous low-current HV supplies. When the MOSFET is insulating the cone electrode (output) is at the source voltage and when the MOSFET is conductive the cone electrode is set at a voltage determined by the 5 kΩ potentiometer.

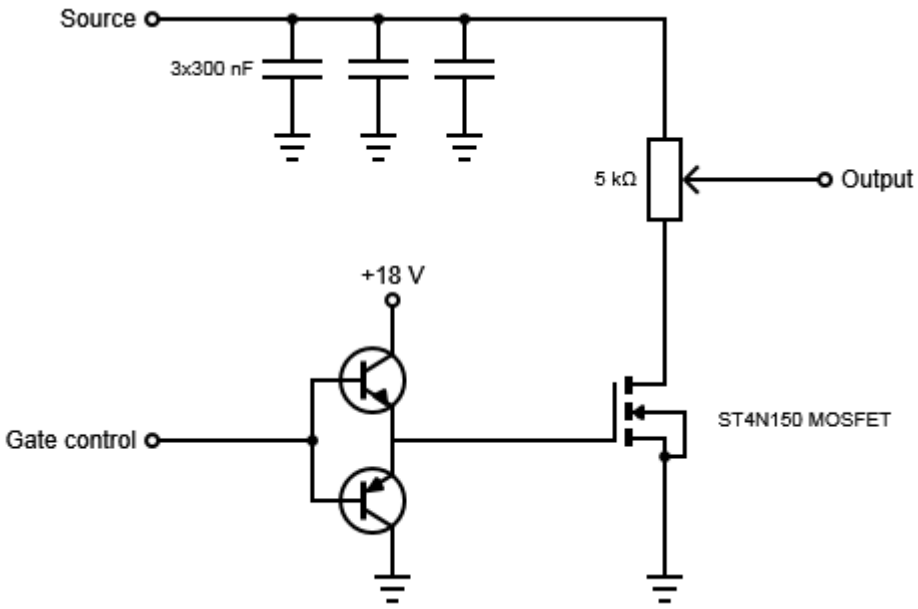


**Figure 5.18:** Circuitry used to change the potential of the injection-extraction electrode.

A 10 $\mu$s pulse was used to test the rise and fall times of the cone electrode. There is $\sim$ 160-ns propagation delay between the micro-controller sending the pulse to open the MOSFET and the voltage dropping. The transition to the low voltage takes $\sim$ 240 ns to drop and stabilise. There is a $\sim$1-$\mu$s delay between the end of the pulse and the voltage rising and it takes $\sim$ 700 ns for the voltage to rise and stabilise. At the IGISOL a 20-$\mu$s pulse is required due to the flight time between the ConeTrap and the second quadrupole deflector (reduced to $\sim$15 $\mu$s if the injection-extraction

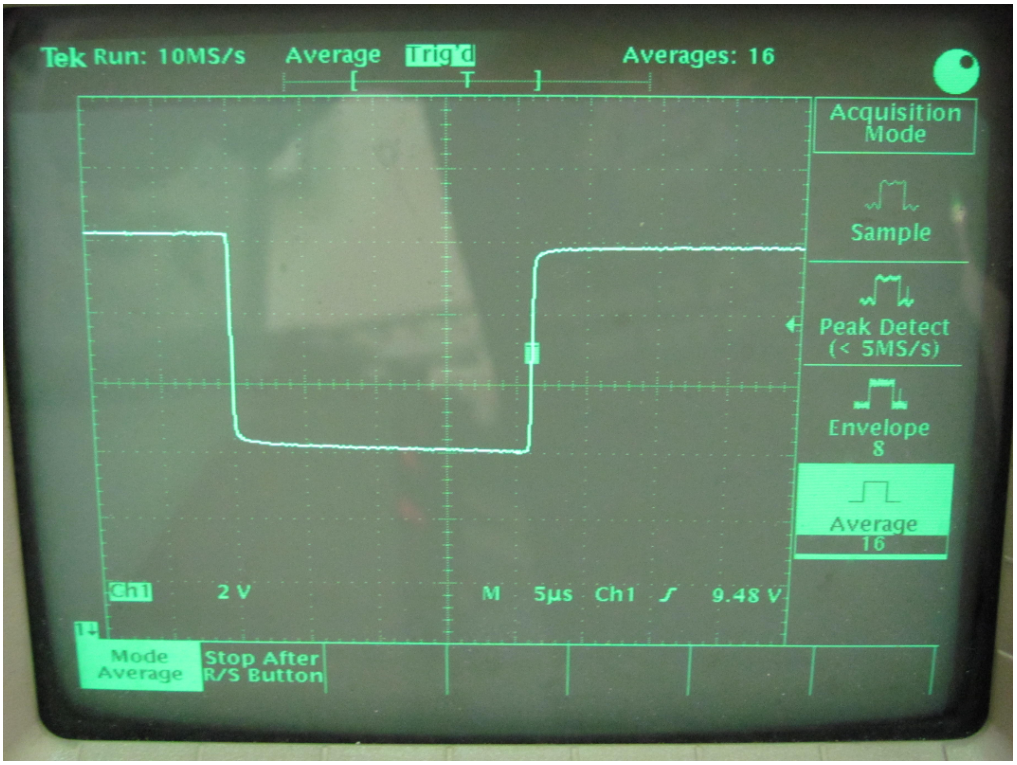


(a) Switch using Cooknell power supply.

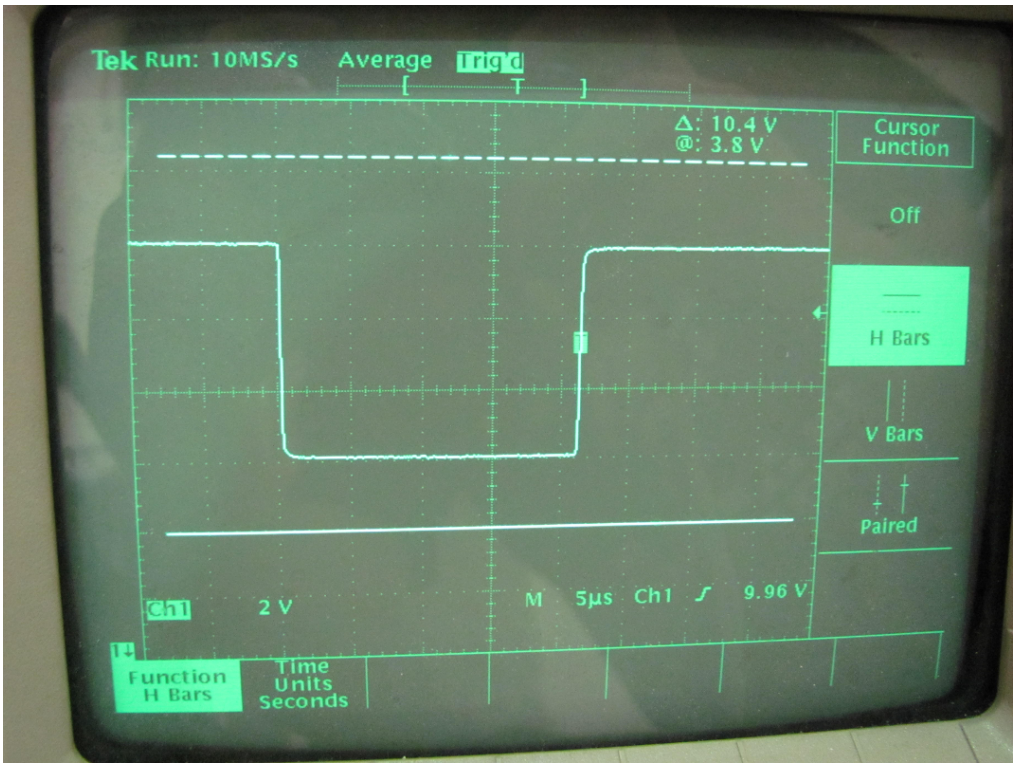


(b) Switch using high-current Hewlett-Packard power supply.

**Figure 5.19:** Oscilloscope images of the voltage switch for the ConeTrap using Cooknell and high-current Hewlett-Packard power supplies.

electrode is shielded).

A Hewlett-Packard high current (10 mA) source was found to provide a faster switch and faster stabilisation of the cone electrode voltage when compared to the Cooknell (1 mA) source (Figure 5.19).

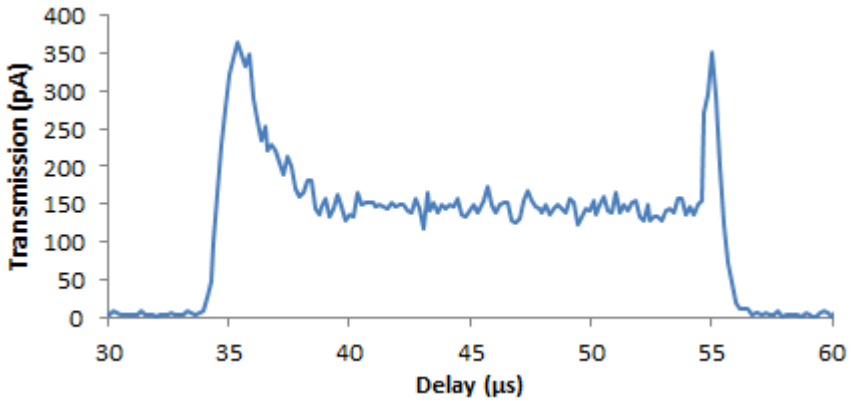


(a) Switch using a coaxial cable length of ∼15 m.

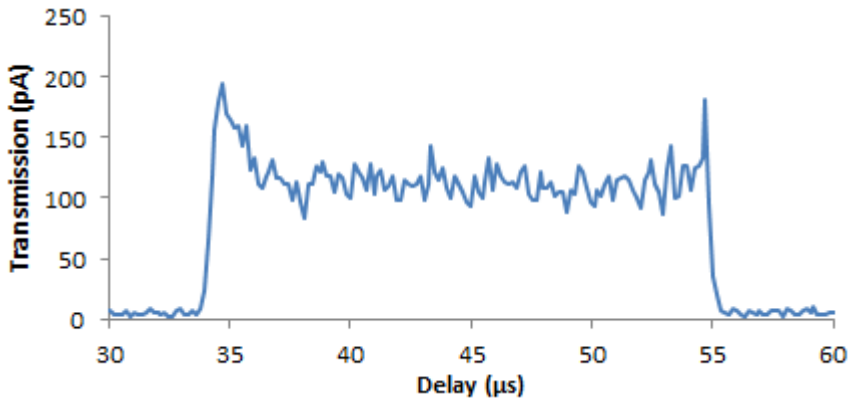


(b) Switch using a coaxial cable length of ∼5 m.

**Figure 5.20:** Transmission current on the Faraday cup in the beam switch-yard showing the effect of a reduced cable length between the fast-switch circuitry and the output electrode. The circuitry was used to switch from 500 V (zero transmission) to 250 V, through a maximum transmission at 280 V.

The speed of the voltage switch provided by the circuitry was tested at the IGISOL facility by applying it to an electrode within a quadrupole lens located upstream from the dipole magnet. The source voltage was set to 500 V, where no current was observed on the Faraday cup located in the beam switch yard, and switched to 250 V to create a beam "chopper". The maximum current on the Faraday

cup was earlier observed at 280 V, thus the voltage switch passes through the optimal voltage and was used to determine the speed of the transition. The length of the cable connecting the switch circuitry and the output electrode was found to critically affect the transition rate. Figure 5.20 shows the effect of reducing the cable length on the transmission current received on the Faraday cup. The fast-switch circuitry was placed above the ConeTrap installation point on the beam line to minimise the required cable length, finally ∼30 cm (Figure 5.21).

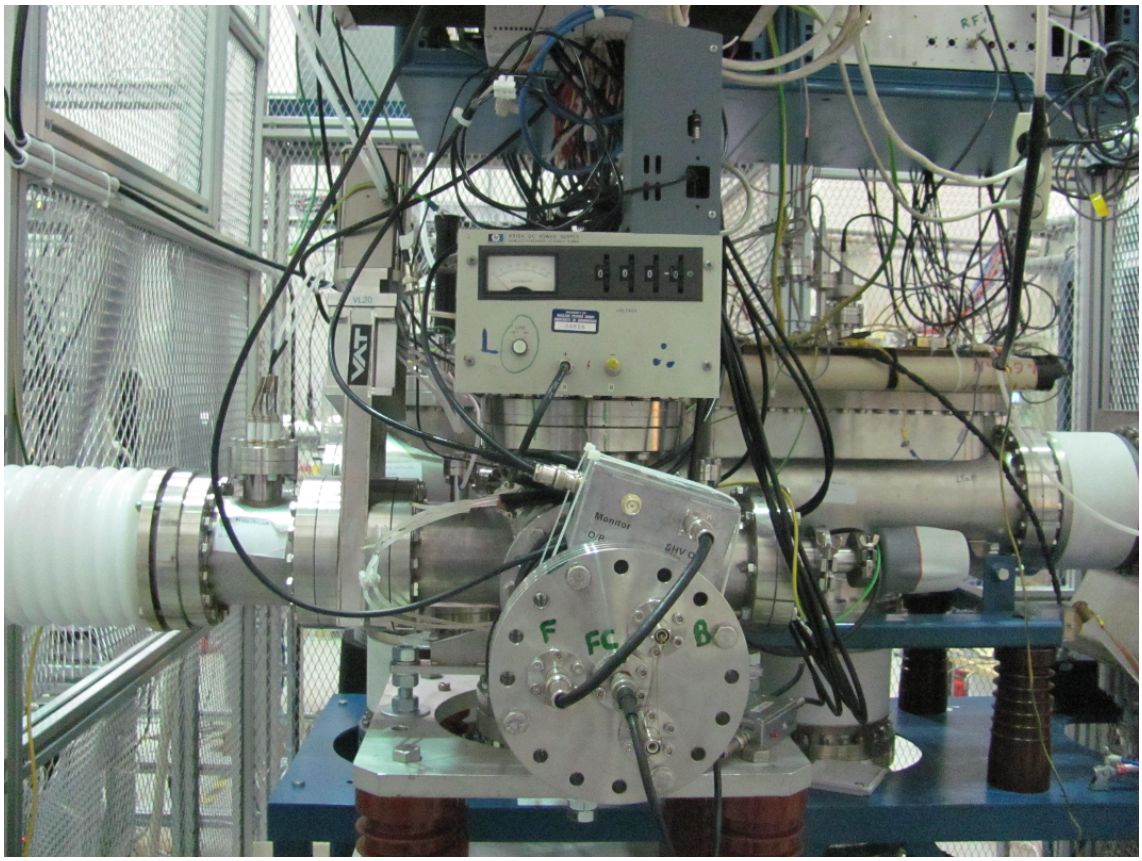


**Figure 5.21:** Fast-switch circuitry in place above the ConeTrap installation point.

### 5.3.3 ConeTrap commissioning stages

The electrostatic nature of the ConeTrap ensures that once the trapping voltages are determined for one case (ion energy) then settings for any other can be accurately scaled. The trapping "ratios" (electrode potentials divided by beam energy

in eV) have been determined using simulations (see Figure 5.22), and can now be used to determine the trapping voltages for arbitrary ion energies. Fine adjustment and tuning is experimentally required to optimise the trapping ratios and then the entire ConeTrap can be controlled using a single power supply and single injection-extraction signal.

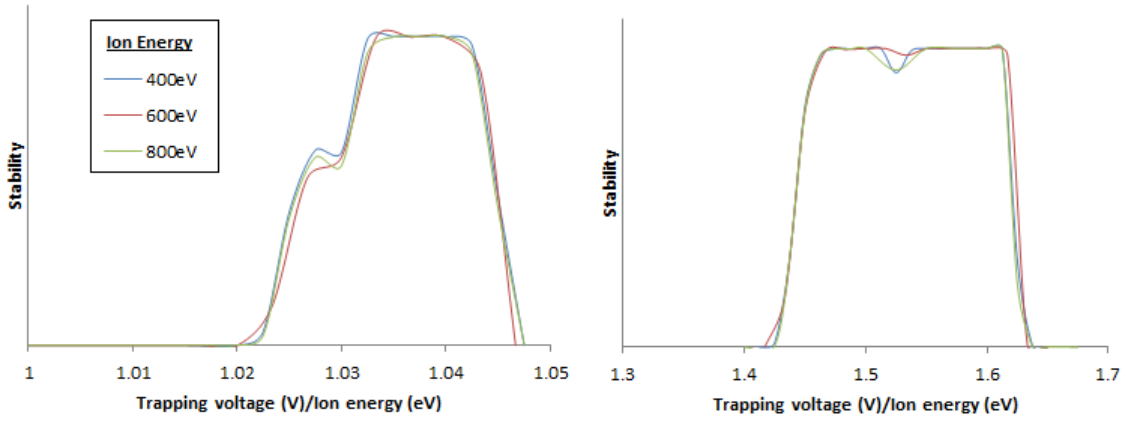


**Figure 5.22:** Stable regions of the ConeTrap in terms of the ratio of the trapping voltage and the simulated ion beam energy. The LV stability region (left) lies between 1.022 and 1.046 and the high-voltage stability region (right) lies between 1.42 and 1.64. The stable regions are invariant of ion energy but absolute emittance and acceptance time can affect the trapping efficiency.

A 3-mm radius Faraday cup was mounted in the front of the central port of the mounting flange beyond the back electrode. The cup measures the ion current passing through the ConeTrap and was used with a continuous beam of stable $^{63}$Cu ions to determine the energy of the ion beam and the required injection voltage on the front cone electrode. Bunched ion ensembles of $^{67}$Zn were used to determine the delay time required to trap ions in the ConeTrap.

#### 5.3.3.1 Ion energy

The mean ion energy in the beam was determined by focusing the continuous $^{63}$Cu beam on the Faraday cup and monitoring the transmission as the voltage of the back cone electrode was raised. The high-voltage platform the ConeTrap is mounted on is held at ~800 V below the Cooler-Buncher platform level and knowledge of the

exact potential is critical for the operation of the ConeTrap. The transmission test was used to determine the error in the voltage supply read-back (known to be substantial).

Simulations showed that the intensity on the Faraday cup falls sharply at the ion beam energy ($V_{trap}$(V)= $E_{ion}$(eV)), after a peak similar to the injection efficiency maximum at $\sim 0.94E_{ion}$ (discussed in Section 5.2.3). The back cone electrode is used as it produces a well-defined sharp cut-off as the electrode potential approaches the ion beam energy. A continuous 540-pA beam of stable $^{63}$Cu was focused onto the Faraday cup. The potential of the back electrode was raised until the transmission dropped to zero, which occurred at a requested voltage of 800.0 V and a read-back of "725 V".

#### 5.3.3.2 Injection voltage

The operational injection voltage was determined by raising the front cone electrode voltage. Figure 5.23 shows the front cone transmission given in the simulations, where the voltage peak at $\sim 0.94E_{ion}$ is the optimal injection voltage. The $\sim 0.94E_{ion}$ potential produces a weakly convergent beam onto the Faraday cup, providing an optimal input beam for the back cone electrode under trapping operations.

The peak in injection efficiency was estimated to occur around 745 V for the 800-eV $^{63}$Cu beam. The stable beam was again focused onto the ConeTrap Faraday cup while the ConeTrap was inactive (producing a current of 500 pA). The front electrode potential was raised and the current on the Faraday cup recorded with results shown in Figure 5.24.

Comparing Figure 5.23 to Figure 5.24 shows similar properties; a minimum at $\sim 680-700$ V followed by a local maximum. The difference in transmission intensities is due to the simulated bunch using a "top-hat" spatial distribution and the real

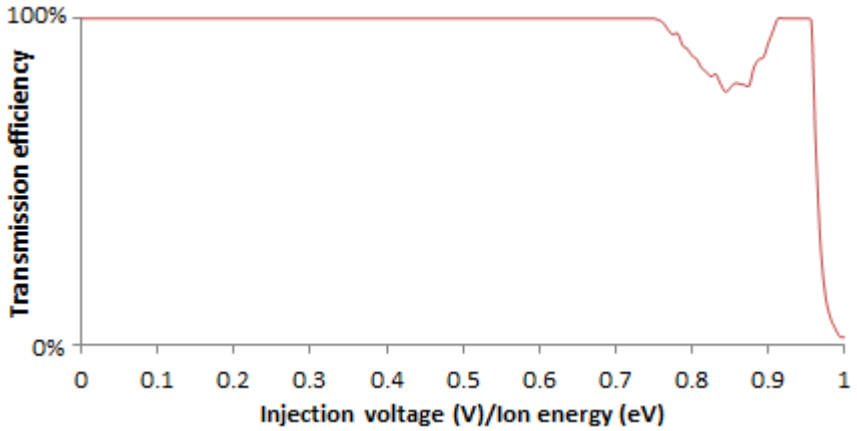


**Figure 5.23:** Transmission efficiency with changing injection voltage on the front cone electrode. Initially the transmission efficiency is already at 100%, followed by a reduction to a minimum at ∼680 V and a local maximum at ∼745 V (at $E_{ion} = 800$ eV).

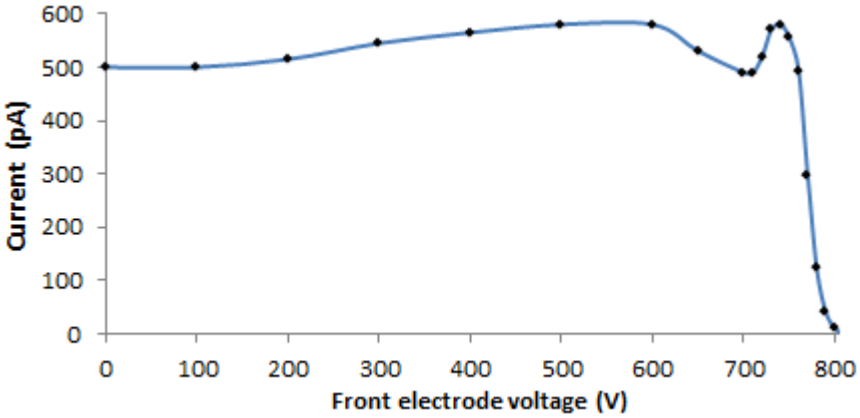


**Figure 5.24:** Injection voltage commissioning data.

ion beam having a Gaussian distribution, however, reassuringly, both show the local maximum at ∼750 V.

#### 5.3.3.3 Trapping delay

The delay time between the ion bunch release signal for the Cooler-Buncher and the trapping signal to raise the injection electrode voltage can be acquired by using a bunched stable beam. The injection electrode is activated and raised to an approximate HV cone electrode voltage upon receiving the delayed trapping signal. The signal opens the ConeTrap for ∼20 $\mu$s to account for the ion approach time and

transit through the injection electrode (as well as the acceptance time). The current measured on the Faraday cup, modeled assuming instantaneous voltage transition and a focused beam when the ConeTrap is inactive, is shown in Figure 5.25.

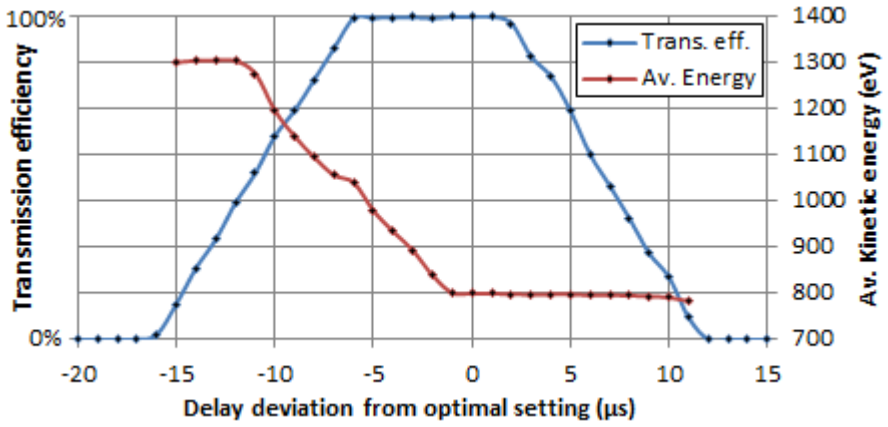


**Figure 5.25:** Transmission efficiency and average ion energy, for a weakly focused simulated beam, as a function of deviation from the optimum injection delay. An injection voltage of 740 V and HV cone electrode voltage of 1250 V were used.

The left side of the figure shows the effects of an overly short delay time, where the ConeTrap closes while ions are passing through the injection electrode (which then exit with larger kinetic energies). The ∼1310 eV average kinetic energy plateau occurs when only the front of the ion bunch is inside the injection electrode when the ConeTrap closes, after which the average kinetic energy decreases, and the ion count increases, as more ions enter the ConeTrap unaffected by the voltage switching. The right side of the figure shows the effects of an overly long delay, where the ConeTrap opens while the ions are approaching the injection electrode and only a few ions can survive injection (after losing some kinetic energy from the voltage drop).

The form of all transmission curves depends on the emittance profile of the incoming beam. Figure 5.26 shows the curves resulting from a realistically divergent incoming beam. Both "peaks" in transmission reflect focusing by premature and delayed switching.

Figure 5.27 shows the transmission efficiency for divergent ions with a 0-$\mu$s bunch width. It shows clearly the focusing effects of the early and late delay signals, the

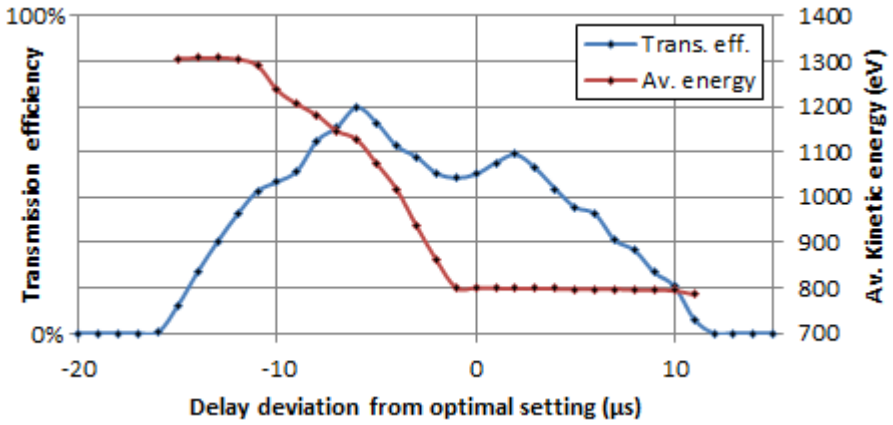


**Figure 5.26:** Transmission efficiency and average ion energy, for a realistically divergent simulated beam, as a function of deviation from the optimum injection delay. An injection voltage of 740 V and HV cone electrode voltage of 1250 V were used.

lower, central plateau of the unaltered ions and also a sharp drop in transmission after the early delay peak. This minimum is caused by the ConeTrap closing as the ions are exiting the injection electrode, therefore experiencing the divergence of the HV cone electrode fringe field but not the focusing effect of the HV cone electrode itself.

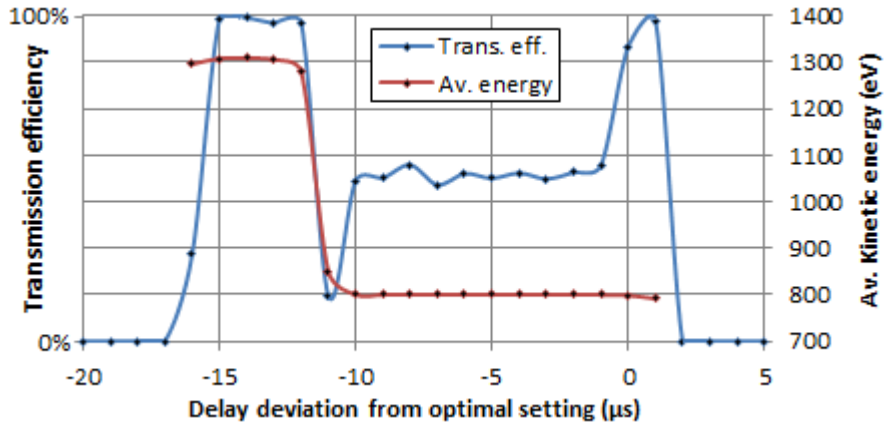


**Figure 5.27:** Transmission efficiency and average ion energy, for a realistically divergent simulated beam with an (unrealistic) bunch width of 0 $\mu$s, as a function of deviation from the optimum injection delay. An injection voltage of 740 V and HV cone electrode voltage of 1250 V were used.

The simulations of realistic beam conditions strongly suggest that the injection delay commissioning should be attempted by tuning the device from over-delayed to

optimal settings. The local maximum due to an over-delayed injection is narrower, compared to an under-delayed injection, and has an almost negligible effect on the kinetic energy of the incoming ions. The situation can be improved further by using a shielded injection-extraction cone electrode (Section 5.2.3), which reduces still further the width of the peak in transmission efficiency and its effect on the ion energies.

During commissioning, the implemented delay time was found to be consistently longer than the micro-controller requested delay by 3 $\mu$s. Bunched ion ensembles of $^{67}$Zn were focused onto the Faraday cup placed behind the ConeTrap and the transmission current monitored with respect to the delay time (Figure 5.28). The optimum delay for the $A = 67$ ions is $\sim$50 $\mu$s, in agreement with the delay of 60 $\mu$s determined for $A = 100$ ions in the simulations (scaled by $\sqrt{67/100}$). The form of the transmission curve is consistent with that shown in Figure 5.25. The $\sim$5 $\mu$s plateau in the transmission maximum suggests a transmission window of $\sim$10 $\mu$s and a bunch length of $\sim$15 $\mu$s (typical for ion bunches in this mass range).

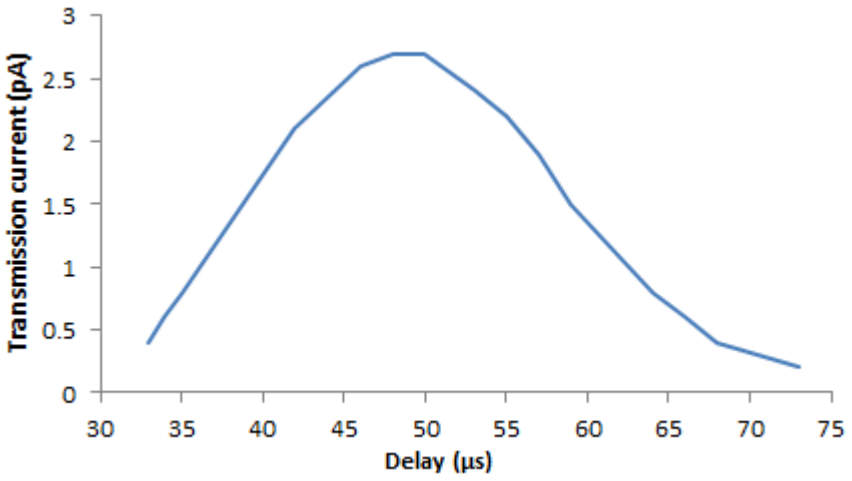


**Figure 5.28:** Transmission current received on Faraday cup with respect to the switch delay upon release from the Cooler-Buncher.

#### 5.3.3.4 Back electrode voltage

The voltage required on the back electrode can best be determined (using a continuous stable beam) by the addition of a ring electrode or injection-extraction electrode shield (Section 5.2.3) placed between the ConeTrap and the quadrupole deflector. The current detected on this aperture electrode can be monitored as a function of back electrode voltage and used to determine the optimal setting for the rear reflector (Figure 5.29). The optimal voltage is within the region where the detected current reaches a minimum, where the ions are transported through the aperture of the electrode. This can also be used to determine the approximate voltage required on the front electrode as both cone electrodes are the same shape and size.

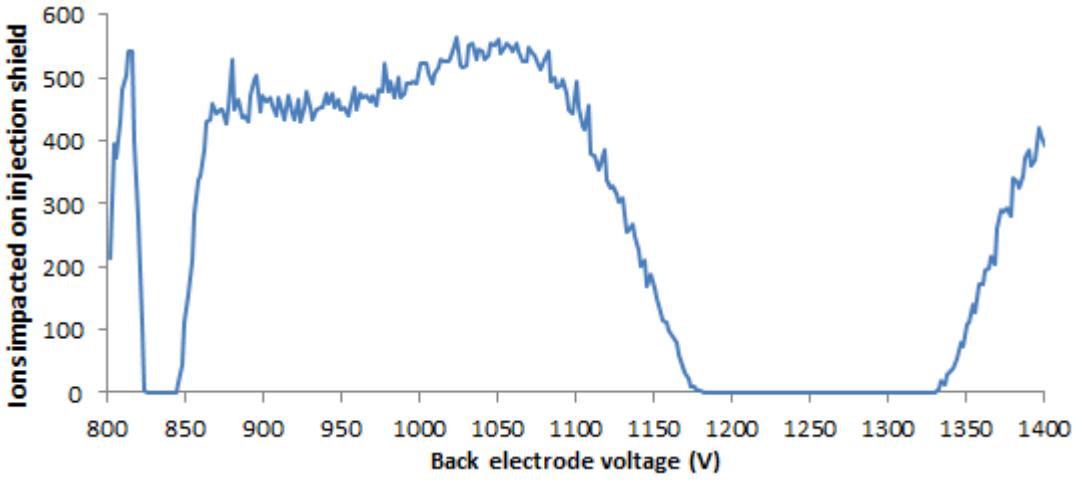


**Figure 5.29:** Current measured on an injection-extraction electrode shield. The LV and HV stability regions are located within the regions where the detected current reaches a minimum.

Whilst desirable, the installation of a suitable ring electrode is not immediately practical with the full ConeTrap due to the lack of mounting positions and available feed-throughs (Section 5.4.5, however, presents a restructuring of the device that, during commissioning, will provide this feature). In the absence of a ring electrode or injection-extraction shield, bunched stable or radioactive ion ensembles can be deflected by the quadrupole deflector, upon release from the ConeTrap, to impact

on a Faraday cup.

#### 5.3.3.5 Trapping potentials

The number of ions captured in a single ConeTrap loading ($\sim 10^5$) is insufficient to register on a Faraday cup however the release of 100 bunches/sec may be observable on the pico-amp scale; alternatively the containment characterisation can be performed using a radioactive bunched beam. A detector (and tape station) can be used to measure the radiation emitted by radioactive ions after release from the ConeTrap. Performance can be assessed by measuring the amount of radiation as the sample builds, thus "de-bunching" the ions into a continuously decaying sample observable by the detector. To optimise the trap the back electrode voltage can be altered freely, however the injection-extraction voltage has to be made constant while optimising the front electrode to avoid changes in the injection-extraction efficiency.

#### 5.3.3.6 Loss mechanisms and containment time

The original study at Stockholm University [70, 71] showed that 4 keV $Ar^+$ ions had a storage lifetime inside their ConeTrap of more than 100 ms at $\sim 7 \times 10^{-8}$ mbar. This limit is due to neutralising and momentum changing collisions between the ions and residual gas. This would suggest that lower energy, slower-moving ions in ultra high vacuum could be contained inside the ConeTrap for many seconds due to the reduced collision rate (solely a function of distance traveled).

The loss rate of ions due to neutralising collisions is given by,

$$\delta N = -N < v \cdot \sigma > \frac{P}{k_B T} \delta t$$

which integrates to become,

$$N(t) = N_0 e^{-\frac{t}{\tau}} \tag{5.1}$$

to give the number of ions remaining in the ConeTrap [70]. In the equations, $N_0$ and $N$ are the initial ion number density and the ion number density at time $t$ respectively. The terms $P$, $k_B$ and $T$ are the pressure, Boltzmann constant and temperature respectively, $v$ and $\sigma$ are the ion velocity and electron transfer cross-section respectively, and $\tau$ is the containment lifetime,

$$\tau = \frac{k_B T}{< v \cdot \sigma > P}.$$

The ion velocities are not constant in the ConeTrap and the electron capture cross-sections are dependent on the ion velocities, therefore the average, $< v \cdot \sigma >$, is used.

While neutralising collisions with residual gas are the main loss mechanism for ions stored in a ConeTrap, another loss comes from collisions between the ions themselves. This loss mechanism dominates at high ion densities/injection currents and at low pressures (when the gas collision loss mechanism is reduced), and rapidly decreases the ion count in the ConeTrap until the ion density reduces to the point where these losses become negligible compared to the neutralising collision-loss mechanism [74]. The loss term added to the rate equation is $-\gamma N^2 \delta t$, where $\gamma$ is a constant based on the geometry of the ConeTrap, and changes Equation 5.1 into the analytical solution [70]:

$$N(t) = \frac{1}{\left(\frac{1}{N_0} + \gamma\tau\right) e^{\frac{t}{\tau}} - \gamma\tau}.$$

The $\tau$ term now refers to the long-term lifetime of ions in the ConeTrap and neglects the effects from ion-ion collisions. The effects of this ion-ion loss term can be reduced by using a larger ConeTrap and reducing the ion density within the trap.

The lifetime of ions inside the ConeTrap also depends on the shape of the orbits

the ions travel along (Section 5.2.1). Ions orbiting in a symmetrical HV ConeTrap will have a shorter lifetime than the same ions in a symmetrical LV ConeTrap. This difference in lifetime arises as the ions spend longer and travel slower in a LV cone electrode compared to a HV cone electrode, therefore reducing the average velocity of the ions and their collision rate with the residual gas. This can be seen by taking the ratio between the lifetimes in the LV and HV stability regions:

$$\frac{\tau_{LV}}{\tau_{HV}} = \frac{< v \cdot \sigma >_{HV}}{< v \cdot \sigma >_{LV}} \simeq \frac{< v >_{HV}}{< v >_{LV}}$$

assuming constant temperature and pressure. If the non-resonant charge exchange cross-sections at low velocities are considered constant then the lifetime ratio in Equation **??** becomes entirely dependent on the average velocity of the trapped ions.

The average velocities for the simulated IGISOL ion bunch were determined to be 20.1 mm/$\mu$s, 32.4 mm/$\mu$s and 24.5 mm/$\mu$s for the LV (830 V), HV (1250 V) and asymmetric ConeTraps respectively.

## 5.4 ConeTrap applications

All ConeTrap design considerations have been made to optimise the trap for multiple applications. In this section applications that are immediately available with the current IGISOL ConeTrap are described. They include a "potential energy elevator", a "neutralising ConeTrap" and the optimum sites for optical pumping for energy manipulation or to acquire greater populations in metastable states. The outline of a "radiation transparent" ConeTrap design that is specifically optimised for detection of nuclear (particle and photon) radiation is presented. Finally, a hybrid design modification of the full ConeTrap, exploiting attractive features of the "radiation transparent" trap, is discussed. It is this hybrid design that is to be

used for the initial commissioning of electrostatic traps at IGISOL 4. Additional ConeTrap designs considered are of possible future interest and are summarised in Appendix B.

### 5.4.1 Optical pumping

The primary application of the ConeTrap at the IGISOL facility will be the efficient holding of ions in vacuum for optical pumping and subsequent release without perturbations to their energy. Ions in the trap may be pumped axially or, as a mesh is used to surround the central area, radially. Axial pumping with a laser would affect those ions moving at resonant velocities in the centre of the Conetrap and exploit the reduction in collinear Doppler broadening. Optical pumping in the radial direction would encounter the full broadening caused by the velocity spread of the ions, however this can be matched with a broadband laser source (TiSa) or, due to the long containment and interaction time of the ConeTrap, it will be possible to use far broader bandwidth sources such as LEDs. LEDs can now provide light in the UV region with linewidths of 5 to 10 nm, which can be used to illuminate all ions in the central region. It is intended that the re-pumping of ions shelved in undesired metastable states be thus achieved without the need for multiple (costly) laser systems.

In a two-level system excited ions can only return to the ground state. If ions are axially pumped and continually promoted to the excited state (laser induced absorption) then their axial velocity, and therefore their kinetic energy, is altered. This is due to the ions experiencing a net drift as they are minutely accelerated upon absorbing the unidirectional axial laser photons while the fluorescent photons are emitted isotropically. If the ion axial velocities change sufficiently, ions can move out of resonance with the laser light and ensembles of ions should thus form kinetic energy bunches at the point when finally off resonance (Figure 5.30). Such

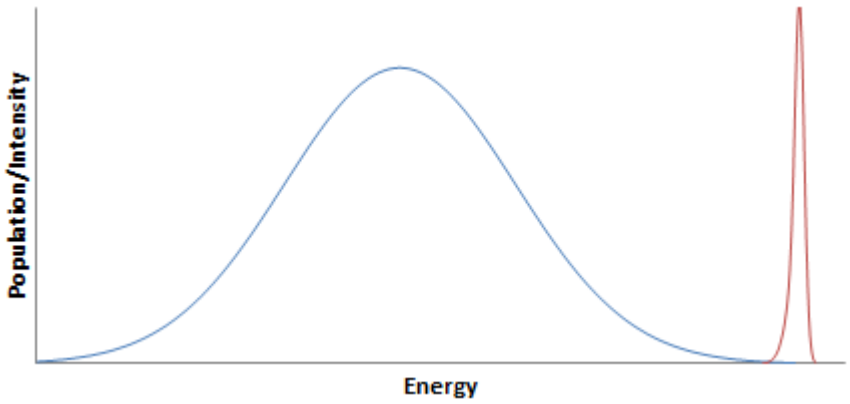


**Figure 5.30:** Energy shift due to repeated laser induced fluorescence. The blue curve shows the absorption profile of the fluorescent transition and the red curve shows the population of the pumped ions.

pumping results in manipulated ensembles having a reduced energy spread and different energies ($\Delta E$ ~2-5 eV) to the contained isobars. The reduced energy spread improves the efficiency of spectroscopy experiments and the energy shift can facilitate the separation of the manipulated ions from the isobaric bunch (upon release from the ConeTrap).

In a three-level system the excited states may also decay into a metastable state and, eventually, this results in the ground-state population being depleted and transferred to the metastable state. It is planned to selectively remove individual species from the contained ion ensemble by combining the "neutralising" ConeTrap (Section 5.4.2) and optical pumping. Exciting ions into a metastable state that has a larger charge-exchange cross-section causes them to be neutralised more rapidly than the rest of the contained ions. This has immediate applications in spectroscopy, where the loss of ions can be used to indicate resonance.

In systems with more than three levels, spectroscopy can be performed from the metastable state (Figure 5.31), however in a system with more than four levels the efficiency of the optical pumping is limited by decays into long-lived states other than the metastable state of interest. During the late phases of the IGISOL 3 operation, spectroscopy of excited species, optically pumped in the Cooler-Buncher, dominated

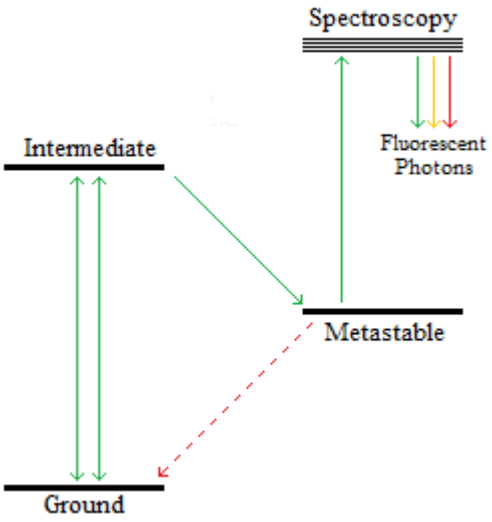


**Figure 5.31:** Optical pumping to metastable state and subsequent spectroscopy.

experimental activity. The Cooler-Buncher is gas-filled and high lying metastable states were relaxed due to collisions with the buffer gas. The ConeTrap allows the ions to be optically pumped into metastable states in high vacuum, where the state populations are only limited by their natural lifetimes and the stability of the trap.

### 5.4.2 Neutralising trap

A primary loss mechanism in the ConeTrap is neutralising collisions between the ions and residual gas (Section 5.3.3.6), therefore a ConeTrap at finite pressure may be used intentionally as a beam neutraliser and to facilitate the techniques discussed in Section 3.7.3.

The rate of neutralisation is proportional to the pressure in the ConeTrap [70, 71] and the speed of the ions; higher ion speeds result in longer distances traveled, more collisions and faster neutralisation. Ions contained in a HV ConeTrap have larger average ion velocities and would be preferable for faster neutralisation (reflected in the shorter trapped lifetime), and less divergent upon exiting the ConeTrap. Efficient neutralisation would be useful for spectroscopy involving state-dependent charge exchange, where the atoms and remaining ions are counted to determine

resonance.

Electrostatic manipulation of neutral species is not possible and the neutral emissions from the ConeTrap will naturally diverge. On the IGISOL line a "neutralising" ConeTrap can be placed inside a high voltage box immediately upstream from the light collection region (replacing the charge exchange cell presently installed).

### 5.4.3 Potential energy elevator

The platform voltage of a working ConeTrap can be altered while ions are contained inside, thus altering the kinetic energy of the ions upon release. Conventionally such elevation is achieved in beam lines by using a drift tube, where the tube voltage is changed as ions transit the device. The drift-tube method requires high speed and high precision voltage switches to change the drift-tube voltage while ions are passing through ($\sim$kV/$\mu$s). The ConeTrap method allows the platform change to occur over any voltage range, at a speed determined by the trap-ion lifetimes. This would allow the platform voltages of the ion source and Cooler-Buncher to be decoupled from the required acceleration of the final ion beam and permit the ions to be accelerated to a precise energy (a critical requirement for laser spectroscopy).

### 5.4.4 "Radiation transparent" ConeTrap

The bunching of ions in the LV cone electrode in the IGISOL ConeTrap means at any instant around 40$-$50% of the ions contained in the ConeTrap are held within the back cone electrode. An LV cone electrode constructed from a fine mesh would provide any radiation detector maximum visibility of the ionic ensemble.

Figure 5.32 shows a ConeTrap specifically designed for radiation-detection applications. The design does not require a region for laser pumping and the long central section has been removed. The back cone electrode can be made larger and wider to remove the sensitivity of the potential to the imperfections of the mesh cone. The

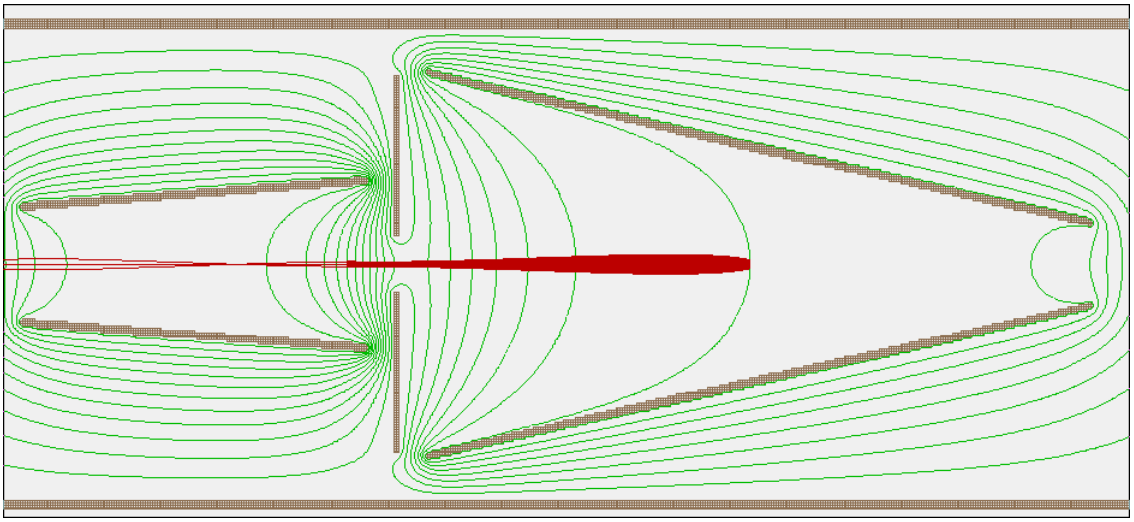

**Figure 5.32:** Structure, orbital shape and potential contours of the radiation transparent ConeTrap. Contours are in steps of 100 V, with the HV cone electrode and LV cone electrode set at 1250 and 805 V respectively. The back cone electrode is 140 mm long with 80 mm and 16 mm diameters at either end (giving an angle of $\sim 12.9°$).

compact nature of the radiation transparent ConeTrap in conjunction with the wide angle of the back cone electrode enables the rear cone electrode to be set at very low potentials that have the largest reflection times and therefore the greatest bunching potential. The LV stability region for the back cone electrode ranges from 805 to 835 V, providing acceptance times of $\sim$22 to $\sim$9 $\mu$s respectively, with $\sim$90% of the ions in the trap held within the back cone electrode at 805 V.

### 5.4.5 "Commissioning"' ConeTrap

The large acceptance times, broad tolerances and fully shielded nature of the "radiation transparent" trap design are highly attractive features to exploit when initially attempting ConeTrap commissioning. The full ConeTrap, Figure 5.17(a), can be readily reconfigured to that shown in Figure 5.33, approximating closely the trap in Section 5.4.4, by straight forward relocation of the injection-extraction cone electrode. Commissioning at IGISOL 4 can thus take place with wider stable regions, specifically the LV stable region, and reduced losses from any change in ion energy

caused by the stabilisation of the trapping potential (Section 5.3.2). The LV stable region extends down to ∼805 V, providing >10 $\mu$s acceptance time, and up to ∼835 V. The stable regions shift downwards in potential as the ions lose energy, thus the LV electrode can be set at 805 V to provide the 10 $\mu$s acceptance time and the ions would have to lose ∼30 eV of kinetic energy before becoming unstable (assuming a stable transition between the focused and parallel orbits). The first disc electrode can furthermore now be used as a shield for injection and as an aperture electrode for extracted ensembles (Section 5.3.3.4).

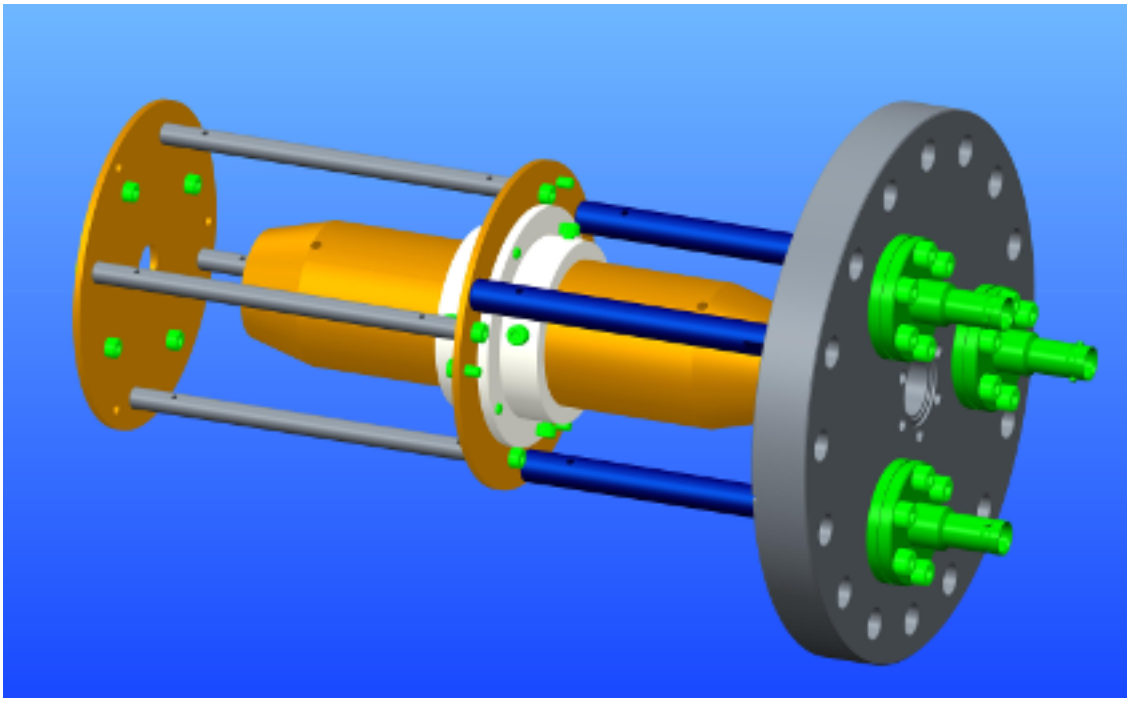

**Figure 5.33:** Model of the "commissioning" ConeTrap.

The design, whilst not immediately permitting internal collinear laser spectroscopy, provides the tolerances and simplifications essential for the initial commissioning of the multi-parameter device and it is this ConeTrap that is, at time of writing, under testing at IGISOL 4. Once commissioned, ions optically-pumped in the *Cooler-Buncher* or *low-energy region* can instead be injected into the device and all aspects of state-dependent charge exchange (Section 3.7.3) explored.

# CHAPTER 6

# First results from IGISOL 4

Before the commissioning of the ConeTrap could be attempted, the new IGISOL facility had to be convincingly restored to at least its previous operating standards. This demonstration and confirmation was achieved by measuring the hyperfine structures and isotope shifts of stable and radioactive isotopes of molybdenum. This element was chosen as it was one of the last studies using the IGISOL 3 facility [17]. The system was used to test whether the IGISOL 4 and beam-line components were operating correctly and to check for consistency with previous results. Molybdenum has a wide range of stable isotopes with fractional compositions ranging between 9−24% [75], providing an equally wide range of stable ion beams.

The singly-charged molybdenum ion has a half-filled valence shell ($d^5$), whose many allowed, particle-hole, angular couplings gives rise to a high density of excited states ∼1.5 eV above a tightly-bound ground state. In the Cooler-Buncher, such metastable states would usually de-excite to the ground state during collisions with the buffer gas and optical pumping to a desired metastable state would be required. However at IGISOL 3 it was found that there is a naturally enhanced population in the first excited state ($4d^4(^5D)5s\ ^6D_{1/2}$) and that relaxation from this state to the ground state ($4d^5\ ^6S_{5/2}$) is inhibited. All excited states of $Mo^+$ up to ∼5 eV are couplings of $d^5$ and $d^4s$ [76], thus all ions in the $d^4s$ configuration de-excite and bottleneck in the first excited state.

The isotope shifts and hyperfine structures of the $^6D_{1/2}$ to $4d^4(^5D)5p\ ^6F_{1/2}$ transition (between energy levels of 11783.36 $cm^{-1}$ and 45853.08 $cm^{-1}$, respectively) were studied for the stable molybdenum isotopes, $^{92,94-98,100}$Mo, and radioactive isotopes, $^{102,104,106,107}$Mo. The hyperfine structure of the $^6D_{1/2}$ to $4d^4(^5D)5p\ ^6F_{3/2}$ (46148.12 $cm^{-1}$) transition in $^{97}$Mo was also measured.

## 6.1 Stable molybdenum

The off-line beam experiment used continuous beams of stable molybdenum isotopes that were focused and overlapped with a counter-propagating, frequency-doubled, CW dye laser beam. The light from a dye laser was locked onto iodine ($I_2$) absorption peaks at 17020.4333 $cm^{-1}$, for the $^6D_{1/2} \rightarrow ^6F_{1/2}$ transition, and 17168.2689 $cm^{-1}$, for the $^6D_{1/2} \rightarrow ^6F_{3/2}$ transition, and was frequency-doubled to wavelengths of 291.23 nm and 293.76 nm, respectively. The power of the frequency-doubled laser beam was ~0.9 mW which caused ~200 photons/s background laser scatter. The stable beams were produced using electric discharge from molybdenum foil. The ions were then Doppler shifted into resonance with the laser beam by tuning the platform voltage of the light collection region. The production rate of resonant photons was of the order $10^3$ $s^{-1}$.

A reference isotope, $A = 98$, was selected and periodically scanned so that any drift in the acceleration voltage or laser frequency would be detected and accounted for in the data analysis. All spectra were fit with Voigt profiles (convolutions of Gaussian and Lorentz distributions) by minimizing squared deviations ($\chi^2$) and the voltage centroids for resonances in each isotope were determined. The resonant voltages can be used to calculate the effective frequency of the laser light in the reference frame of the ion and the difference of these between any two isotopes gives the "isotope shift". Tables 6.1 and 6.2 compare the isotope shifts and hyperfine dipole constants measured, for the $^6D_{1/2} \rightarrow ^6F_{1/2}$ transition, at the IGISOL 4 and

IGISOL 3.

The isotope shifts are consistent within the total errors, which include the statistical error and a systematic error. The systematic error is much larger than the statistical error and is due to the 0.1% uncertainty in the acceleration voltage monitor. The isotopes shifts measured in this study are, however, consistently larger (by $0.2 - 0.8\%$) than those measured at IGISOL 3, suggesting a difference in the acceleration voltage monitor between the two studies. The hyperfine dipole coefficients are all consistent within one or two standard deviations of their statistical error.

| A | $I^\pi$ | $\delta\nu^{92,A}$ (MHz) | |
|---|---|---|---|
| | | IGISOL 3 | IGISOL 4 |
| 92 | $0^+$ | 0 | 0 |
| 94 | $0^+$ | -762(1)[9] | -768(1)[8] |
| 95 | $5/2^+$ | -925(1)[13] | -933(1)[12] |
| 96 | $0^+$ | -1390(1)[16] | -1401(1)[17] |
| 97 | $5/2^+$ | -1391(1)[21] | -1400(1)[21] |
| 98 | $0^+$ | -1842(1)[20] | -1847(1)[25] |
| 100 | $0^+$ | -2645(1)[33] | 2650(1)[33] |

**Table 6.1:** Comparison of isotope shifts for the $^6D_{1/2} \rightarrow ^6F_{1/2}$ transition in the stable molybdenum isotopes. The isotope shifts are given relative to $^{92}$Mo. Statistical errors are in curved brackets and total errors are given in square brackets.

| A | $I^\pi$ | A($^6D_{1/2}$) (MHz) | | A($^6F_{1/2}$) (MHz) | |
|---|---|---|---|---|---|
| | | IGISOL 3 | IGISOL 4 | IGISOL 3 | IGISOL 4 |
| 95 | $5/2^+$ | -919.7(5) | -920.5(3) | -688.4(5) | -688.8(2) |
| 97 | $5/2^+$ | -940.0(6) | -939.7(3) | -702.2(6) | -702.4(6) |

**Table 6.2:** Comparison of hyperfine dipole coefficients for the $^6D_{1/2} \rightarrow ^6F_{1/2}$ transition in the stable odd isotopes of molybdenum.

The distribution of the hyperfine resonances of the $^6D_{1/2} \rightarrow ^6F_{1/2}$ transition observed in odd-$N$ isotopes was used to calculate the magnitudes of the hyperfine

dipole coefficients for the two states involved. Their signs and ordering of states, however, had to be determined by comparing the relative intensities of the peaks with those calculated from angular momentum coupling coefficients. The two peaks corresponding to the $|\Delta F| = 1$ transitions have, by symmetry, the same intensity. If these $|\Delta F| = 1$ peaks are located between the two peaks corresponding to the $\Delta F = 0$ transitions then two solutions for the hyperfine dipole coefficients exist; in which the coefficients have opposite signs. If the $\Delta F = 0$ peaks are positioned between the $|\Delta F| = 1$ peaks, as is the case for the $^6\mathrm{D}_{1/2} \rightarrow ^6\mathrm{F}_{1/2}$ transition, then both dipole coefficients have the same sign. This is shown in Figure 6.1, where the solutions for the lower and upper state ($A_L$ and $A_U$) are given in terms of the magnitudes of the measured hyperfine dipole coefficients ($a_1$ and $a_2$, with $a_1 > a_2$). Another transition, involving one of the states with $J = 1/2$, was required to determine which set of solutions was correct. The ratio $\frac{A_1}{A_2}$ is, to an excellent approximation, constant within an isotope chain, therefore the alternative transition only needs to be measured for a single isotope within a chain.

In this case, the transition from the $^6\mathrm{D}_{1/2}$ state to $4\mathrm{d}^4(^5\mathrm{D})5\mathrm{p}\ ^6\mathrm{F}_{3/2}$ (46148.12 $\mathrm{cm}^{-1}$) was studied for $^{97}$Mo to determine the correct solution (at the IGISOL 3 the same transition was studied in $^{95}$Mo). The fitted spectrum of this transition for $^{97}$Mo and the hyperfine structure of the states are shown in Figures 6.2 and 6.3. The spectrum indicates that the hyperfine dipole coefficient solutions are negative, with the lower state found to have A($^6\mathrm{D}_{1/2}$)=−939.0(6) MHz (in agreement with the independent values measured in the $^6\mathrm{D}_{1/2} \rightarrow ^6\mathrm{F}_{1/2}$ transition shown in Table 6.2).

The $^6\mathrm{D}_{1/2} \rightarrow ^6\mathrm{F}_{3/2}$ transition was also studied to determine the hyperfine quadrupole coefficient, $B$, of the upper state as no quadrupole shift occurs in the $^6\mathrm{D}_{1/2} \rightarrow ^6\mathrm{F}_{1/2}$ transition due to $J_{upper}, J_{lower} < 1$. Table 6.3 shows the hyperfine dipole and quadrupole coefficients measured for the $^6\mathrm{F}_{3/2}$ state in $^{97}$Mo, with the same constants in $^{95}$Mo, measured at the IGISOL 3, shown for comparison. Although a

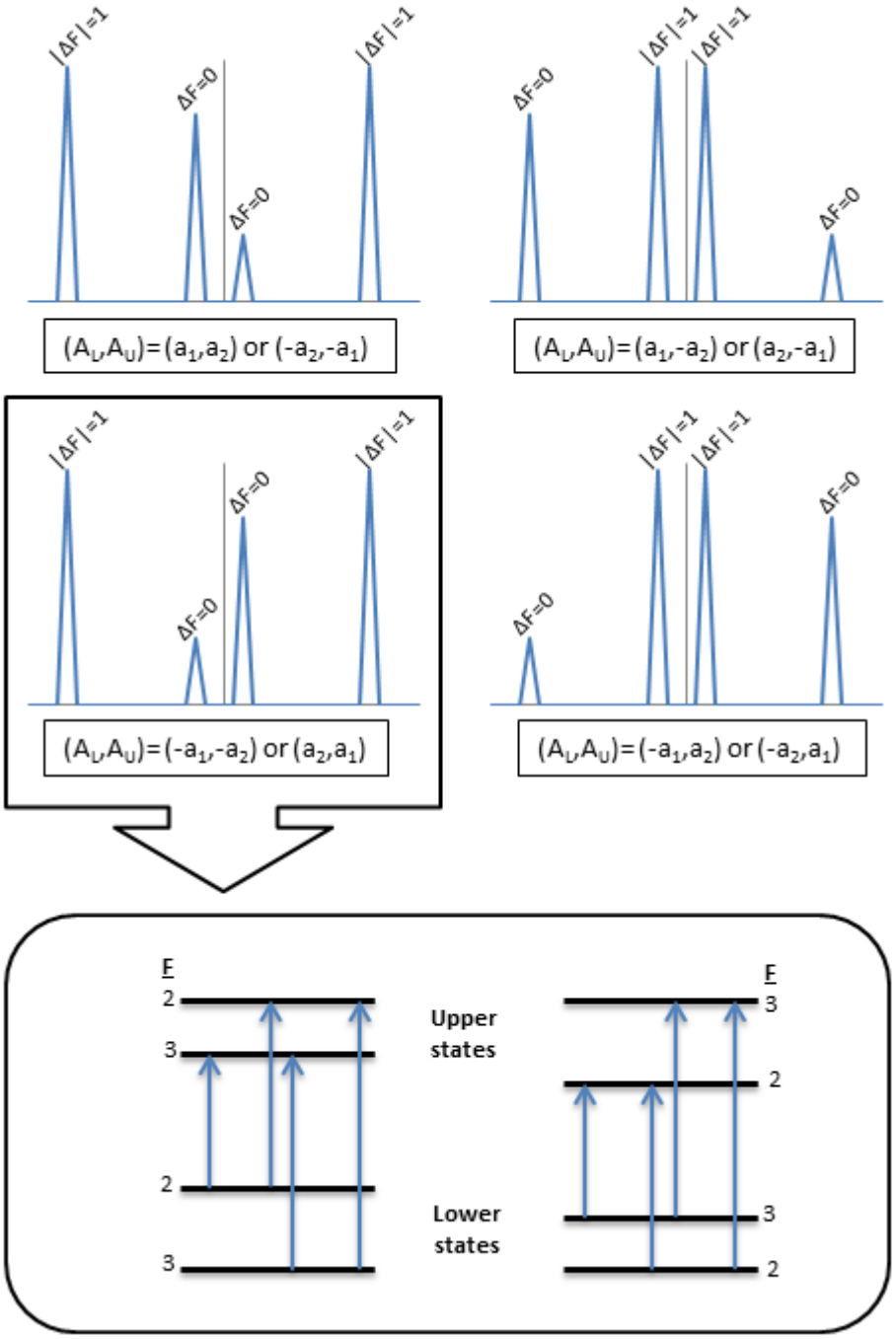


**Figure 6.1:** Multiple solutions for the hyperfine structure centroids of a $J = 1/2 \rightarrow 1/2$ transition; reduced to two solutions using the relative intensities of the peaks (calculated from angular momentum coupling coefficients). The magnitudes of the hyperfine dipole coefficients are $a_1$ and $a_2$ with $a_1 > a_2$ and relative intensities were calculated, and states labeled, using a nuclear spin, $I$, of 5/2.

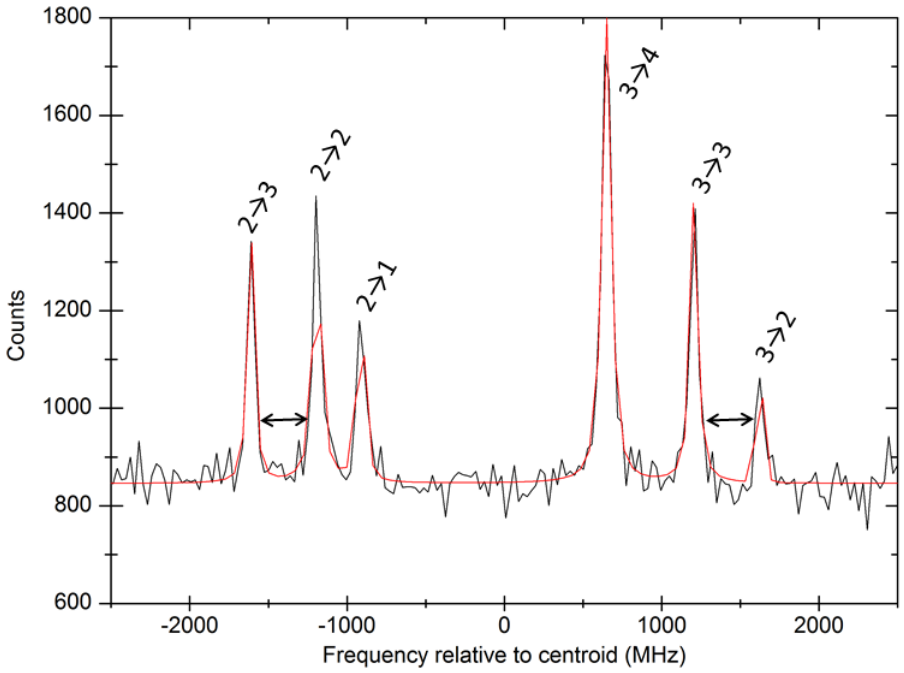


**Figure 6.2:** Hyperfine spectra of the $^6D_{1/2} \rightarrow ^6F_{3/2}$ transition for $^{97}$Mo and Voigt profile fit. Transitions are labeled and the double arrows indicate the gap shown in Figure 6.3.

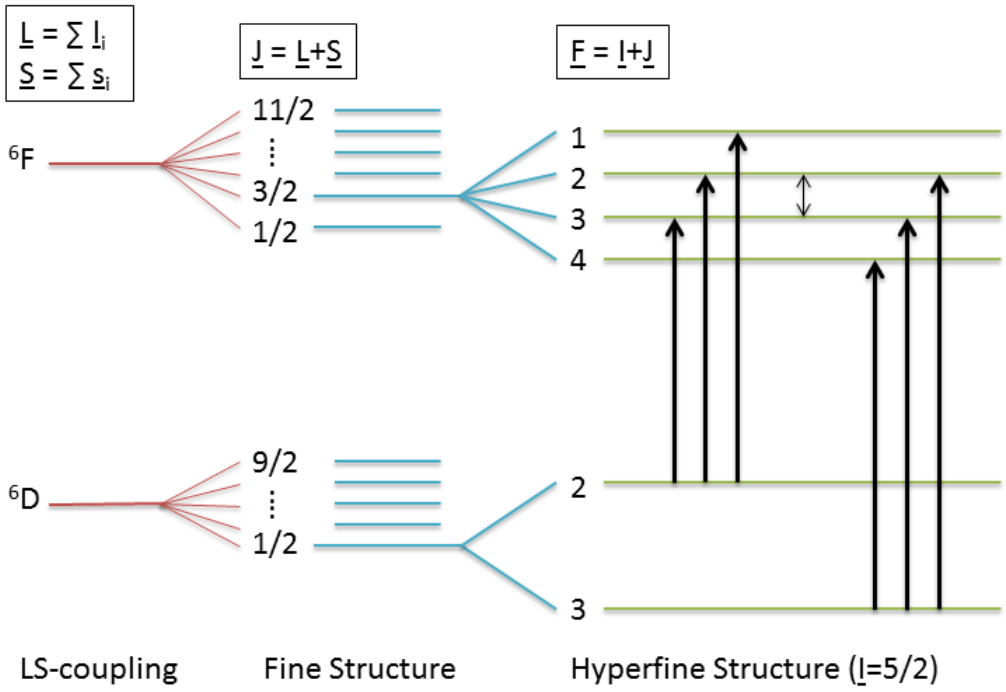


**Figure 6.3:** Fine and hyperfine structure of the $^6D_{(1/2)}$ and $^6F_{(3/2)}$ states with transitions labeled in Figure 6.2. The double arrow indicates the gaps shown in Figure 6.2.

transition involving a $J = 3/2$ state usually displays a quadrupole splitting, the hyperfine quadrupole coefficient was found to be 0(2) MHz. The difference between the hyperfine dipole coefficients, $A$, is due to the different magnetic moments of the two nuclei ($-0.9142(1)\mu_N$ and $-0.9335(1)\mu_N$ for $^{95}$Mo and $^{97}$Mo respectively [75]). No hyperfine anomaly was found between the two $A$ values beyond the statistical error.

| Hyperfine constant (MHz) | IGISOL 3 ($^{95}$Mo) | IGISOL 4 ($^{97}$Mo) |
|---|---|---|
| A($^6F_{3/2}$) | -135.9(3) | -139.5(3) |
| B($^6F_{3/2}$) | 0(2) | 0(2) |

**Table 6.3:** Hyperfine dipole and quadrupole constants for the $^6F_{3/2}$ state in $^{95}$Mo and $^{97}$Mo, measured at the IGISOL 3 and IGISOL 4 respectively.

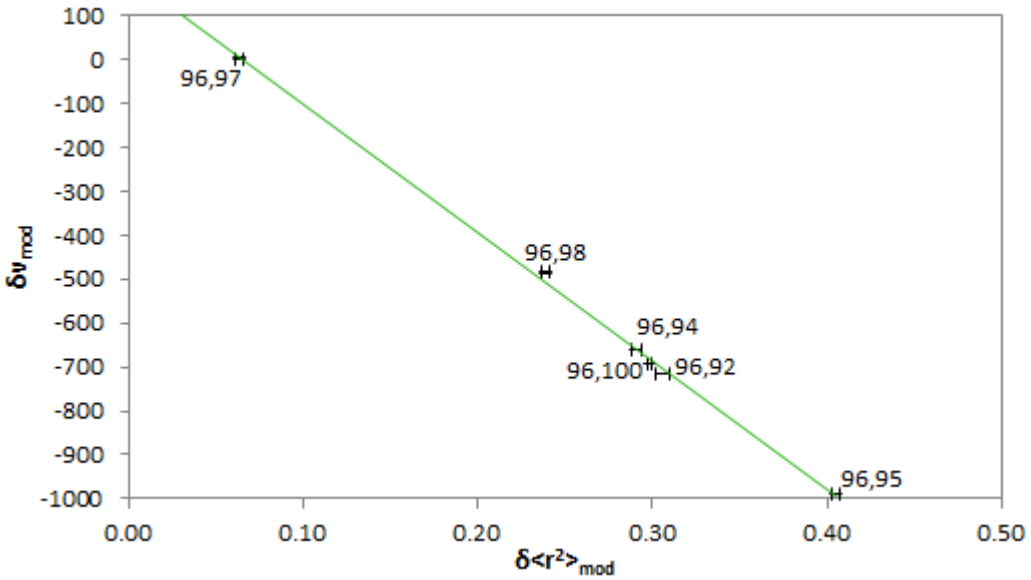


**Figure 6.4:** A King plot used to calibrate the electronic factor, F, and mass shift factor, M. The $\delta < r^2 >$ values used to create the King plot were taken from Fricke et al. [77].

The isotope shifts measured in the IGISOL 3 experiment were plotted in a modified King plot (see Section 2.3.3.1) with combined analysis evaluations of $\delta <r^2>$ for the stable molybdenum isotopes [77]. This King plot was then used to determine the electronic factor, $F$, and mass-shift factor, $M$. These were then used to refine the

values of $\delta <r^2>$ for the stable isotopes and determine $\delta <r^2>$ for the radioactive isotopes of molybdenum [27]. The isotope shifts measured at the IGISOL 4 were similarly used in a modified King plot (Figure 6.4), in combination with the same $\delta <r^2>$ values, to independently (re)determine the electronic factor and mass shift factor. The results of the two experiments were found to agree, with the IGISOL 4 data giving $F = -2993(115)$ MHz fm$^{-2}$ and $\delta\nu_{MS}^{96,98} = 188(32)$ MHz compared to $F = -3024(91)$ MHz fm$^{-2}$ and $\delta\nu_{MS}^{96,98} = 195(25)$ MHz found at IGISOL 3.

## 6.2 Radioactive molybdenum

Beams of radioactive molybdenum were produced from the fission of natural uranium induced by bombardment of 30-MeV protons. The ions were accumulated in the Cooler-Buncher for 100 ms, released in bunches and overlapped with the counter-propagating laser beam for time-of-flight gated laser spectroscopy. The laser lock was set to a higher-frequency iodine absorption peak (17021.2341 cm$^{-1}$) to reduce the scanning voltage needed to Doppler shift the heavier and slower moving isotopes into resonance. The hyperfine structure of the $^6D_{1/2} \rightarrow ^6F_{1/2}$ transition was measured for $^{102,104,106}$Mo and, for the first time, $^{107}$Mo. Using bunched-ion spectroscopy it was possible to measure the hyperfine structure with production rates of resonant photons of $< 1$ s$^{-1}$.

| A | $I^\pi$ | $\delta\nu^{92,A}$ (MHz) | |
|---|---|---|---|
| | | IGISOL 3 | IGISOL 4 |
| 102 | $0^+$ | -3635(7)[42] | -3640(6)[41] |
| 104 | $0^+$ | -4353(6)[46] | -4353(4)[49] |
| 106 | $0^+$ | -4836(8)[56] | -4808(8)[56] |

**Table 6.4:** Comparison of isotope shifts for the $^6D_{1/2} \rightarrow ^6F_{1/2}$ transition in $^{102,104,106}$Mo. The isotope shifts are given relative to $^{92}$Mo. Statistical errors are in curved brackets and total errors are given in square brackets.

The isotope shifts of $^{102,104,106}$Mo were evaluated and compared to those studied previously, shown in Table 6.4. The results for $^{102}$Mo and $^{104}$Mo are consistent within statistical errors, however there is a significant difference between the isotope shifts measured for $^{106}$Mo and they are only consistent within three standard deviations of their combined statistical error (with the difference between the two isotope shifts and their combined error being 28(11) MHz).

The measurement of the hyperfine structure resonances of $^{107}$Mo was too challenging to be performed at the IGISOL 3. The IGISOL 4 facility is already able to observe these resonances, albeit with relatively poor statistics ($\sim$0.1 resonant photons per second). Three peaks were consistently observed in the measured spectra. The lack of a fourth peak suggests a low nuclear spin, with this peak either being very weak in intensity, compatible with $I$=3/2, or having zero intensity, compatible with $I$=1/2 (as a 0$\rightarrow$0 transition is forbidden), as shown in Figure 6.5. The isotope shifts and hyperfine dipole coefficients were thus calculated for $^{107}$Mo assuming spins of both 1/2 and 3/2. The isotope shifts and changes in mean-squared charge radius of the nucleus, calculated using the calibrated electronic factor, $F$, and mass shift factor, $M$, are shown in Table 6.5. The hyperfine dipole coefficients and magnetic moments of the nucleus, calculated using Equation 2.6 and a nuclear magnetic moment of -0.9335(1)$\mu_N$ for $^{97}$Mo [75] as a reference, are shown in Table 6.6.

| Nuclear spin, $I$ | $\delta\nu^{92,107}$ (MHz) | $\delta < r^2 >^{92,107}$ (fm$^2$) |
|---|---|---|
| (1/2) | -5008(4)[62] | 2.12(10) |
| (3/2) | -4979(4)[62] | 2.11(10) |

**Table 6.5:** Isotope shifts of the $^6$D$_{1/2} \rightarrow ^6$F$_{1/2}$ transition in $^{107}$Mo, and the change in mean-squared charge radius of the nucleus, assuming a nuclear spin of 1/2 or 3/2. Statistical errors are in curved brackets and total errors are given in square brackets.

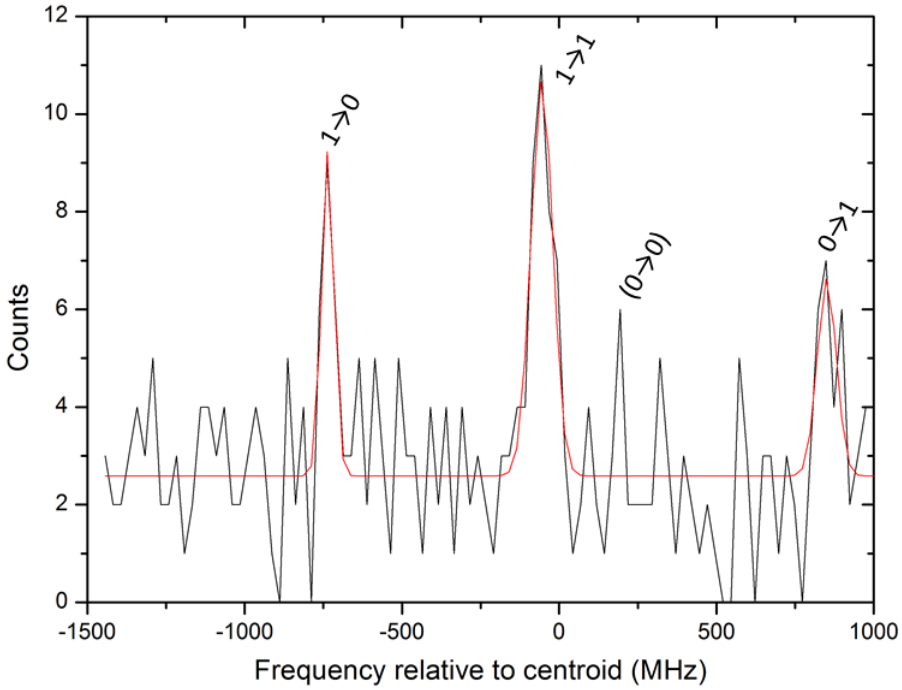


(a) $I$=1/2

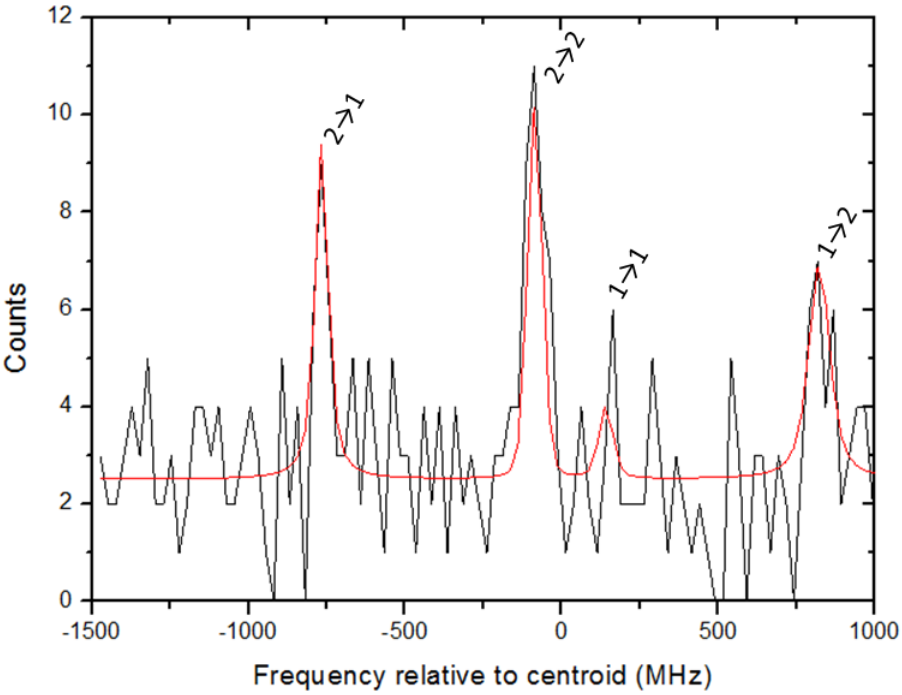


(b) $I$=3/2

**Figure 6.5:** Hyperfine spectra of the $^6D_{1/2} \rightarrow ^6F_{1/2}$ transition for $^{107}$Mo, assuming $I$=1/2 or 3/2, with fitted Voigt peaks. Transitions are labeled and the approximate position of the forbidden 0→0 transition is indicated.

| Nuclear spin, $I$ | A($^6$D$_{1/2}$) (MHz) | A($^6$F$_{1/2}$) (MHz) | magnetic moment, $\mu$ ($\mu_N$) |
|---|---|---|---|
| (1/2) | +904(6) | +680(5) | +0.179(2) |
| (3/2) | +455(4) | +342(3) | +0.270(5) |

**Table 6.6:** Hyperfine dipole coefficients for the $^6$D$_{1/2} \rightarrow ^6$F$_{1/2}$ transition in $^{107}$Mo, and the magnetic moment of the nucleus, assuming nuclear spins of 1/2 and 3/2.

## 6.3 Discussion

Isotopes of elements in the $Z \sim 40$ region are of long-standing interest at the IGISOL and other facilities as they exhibit rapid structural changes in both their neutron-rich and neutron-deficient isotopes. This work focuses on the structural changes observed in nuclei beyond the $N = 50$ shell closure. Near-spherical ground states exist at $N = 50$, but then nuclei increase in oblate deformation, both in static and dynamical components, as they approach $N = 60$. At $N = 60$ a sudden rise in deformation is observed for elements close to $Z = 40$, indicating a rapid transition to a rigid prolate deformation [78]. This effect is most prominent in yttrium ($Z = 39$) [25], but reduces in magnitude in the adjacent elements (strontium ($Z = 38$) [79, 80] and rubidium ($Z = 37$) [81] beneath and zirconium ($Z = 40$) [82] and niobium ($Z = 41$) [83] above). At krypton ($Z = 36$) [84] and molybdenum ($Z = 42$) [17] a smooth transition to deformed shapes is observed around $N = 60$. Measured changes in mean-square charge radii are shown for ground states of yttrium and molybdenum in Figure 6.6.

The sudden rise in deformation at $N = 60$ is due to the difference in deformation magnitude, $|\beta_2|$, between the oblate and prolate states. Theoretical predictions for the behaviour of $< r^2 >$ beyond $N = 60$ differ greatly due to the close competition between the near-degenerate minima, in the excitation energies, of oblate and prolate shapes. Such critical behaviour makes the region an ideal testing ground for nuclear models. Molybdenum nuclei are predicted to have triaxial properties beyond $N = 60$

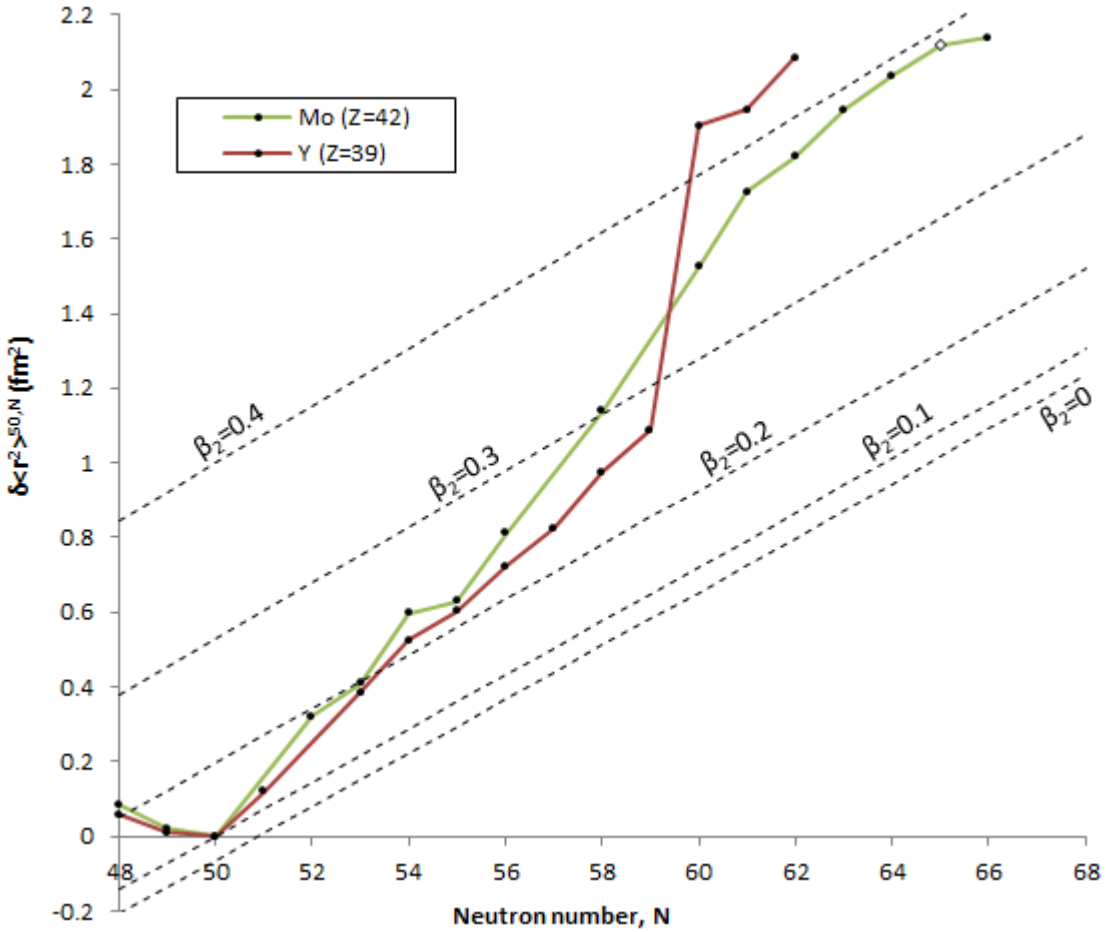


**Figure 6.6:** Change in mean square charge radii for molybdenum (this work and [27]) and yttrium [25] isotopes in the N$\sim$ 50 − 60 region. Iso-deformation lines, calculated from the droplet model [23], are shown for the molybdenum isotopes and are normalised to $\beta_2(^{92}\text{Mo}) = 0.1$ [85]. The mean-squared charge radii of both elements are plotted relative to $N = 50$, with the $\delta < r^2 >$ for $^{107}$Mo, assuming I= 1/2, shown as an open circle.

[78] and to peak in deformation at $N = 65$ [86]. Even nuclei in this region are then predicted to become oblate beyond $N = 66$, with the transition in molybdenum occurring around $N = 68 - 70$ [87]. The transition to oblate deformation would be indicated by a decrease in deformation, due to the oblate deformation energy minima occuring at lower $|\beta_2|$.

In this work the hyperfine structure of $^{107}$Mo has been measured for the first time. Initial observations, before a repeat experiment with a fully optimised IGISOL, indicate the nuclear spin is either 1/2 or 3/2. The nuclear spin is unlikely to be $> 3/2$

due to the absence of a fourth resonance in the observed hyperfine spectrum. The change in mean-square charge radius of the nucleus, obtained from the measured isotope shift, indicates a peak in deformation at $N = 65$, irrespective of spin assignment, in agreement with theory [86]. Although the molybdenum nuclear ground state is predicted to become oblate at $N = 68 - 70$ for the even isotopes, predictions for odd nuclei suggest the transition may occur earlier in an odd isotope such as $^{107}$Mo ($N = 65$) or $^{109}$Mo ($N = 67$). The smooth evolution of the mean-square charge radius suggests that the transition to oblate deformation has not occurred for molybdenum nuclei with $N \leq 66$.

If the nuclear spin of $^{107}$Mo is 1/2 and the quadrupole deformation is $\beta_2 \simeq 0.35 - 0.4$, then the ground state of the nucleus can be sensibly attributed to the $1/2^+[411]$ Nilsson orbital (above the $N = 64$ deformed sub-shell in Figure 6.7) of the $3s_{1/2}$ spherical shell state (overlapped with the $1g_{7/2}$ state in Figure 6.7). A nuclear spin of 3/2 could be attributed to the $1/2^+[400]$ or $3/2^+[402]$ Nilsson orbitals from the $2d_{3/2}$ spherical shell state, however this is unlikely as these orbitals are predicted to rise beyond the Fermi level of the $^{107}$Mo isotope. If the deformation of the nucleus is considered to be oblate ( $\beta_2 \simeq -0.35 - 0.4$), then the nuclear spin could potentially be attributed to the $1/2^-[301]$ Nilsson orbital of the $2p_{1/2}$ spherical shell state, but a deformation of such magnitude is not expected for the oblate minimum. The possible triaxial nature of the molybdenum nucleus in this region makes attributing a Nilsson orbital problematic however, as they are conventionally calculated assuming axial symmetry.

## 6.4 Future work on molybdenum

Future work on the molybdenum isotopes at IGISOL 4 would seek to exploit the full production improvements of the facility to determine and observe when the ground state transitions to an oblate deformation occurs. This can be achieved

through measurements of the isotope shift to determine any sharp changes in the mean-square charge radius, or in combination with measurements of the quadrupole moment for odd-A nuclei. The measurement of the $^{107}$Mo hyperfine structure will shortly be repeated to uniquely assign the nuclear spin.

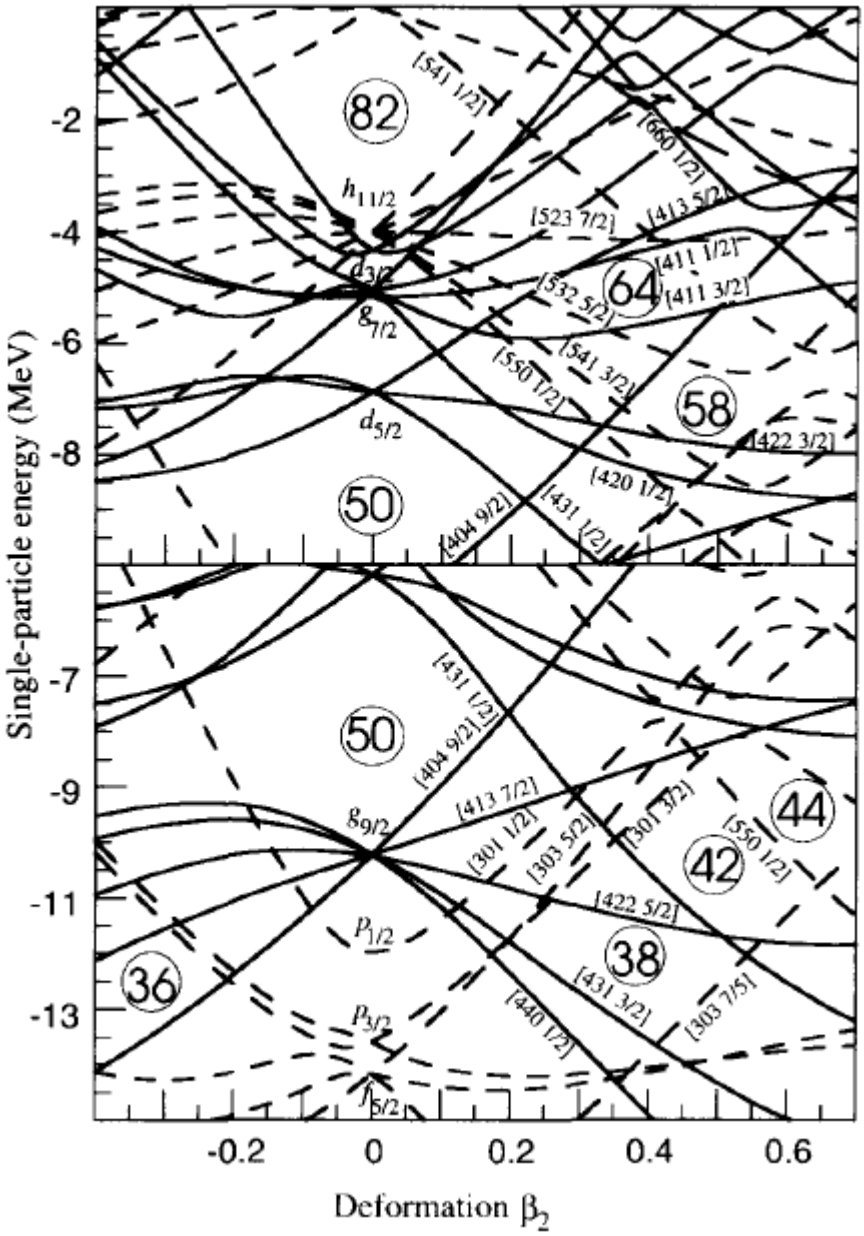


**Figure 6.7:** Nilsson diagrams for neutrons (top) and protons (bottom) in a deformed Woods-Saxon potential. Single-particle energy levels, for a central $^{100}$Zr nucleus, are shown according to the quadrupole deformation parameter, $\beta_2$ [87].

# CHAPTER 7

# Summary

During this work the IGISOL 4 facility has been developed from the construction of the building (Figure 7.1) to a complete, operational isotope separator and laser station (Figure 7.2) that has produced its first new spectroscopic results.

**Figure 7.1:** The laboratory before the installation of IGISOL 4 (October 2009).

In this thesis, the theoretical modeling of the IGISOL 4 facility has been presented and the simulations used to design the beam line and determine parameters for commissioning have been discussed. The optimum potentials for ion deflection by the quadrupole deflectors have been investigated and an Einzel lens, designed to

transport ions between the deflectors in the low-energy region, has been built and installed at the facility. The beam-line simulations were also used to determine the timing required for the operation of a new electrostatic ion trap, ConeTrap.

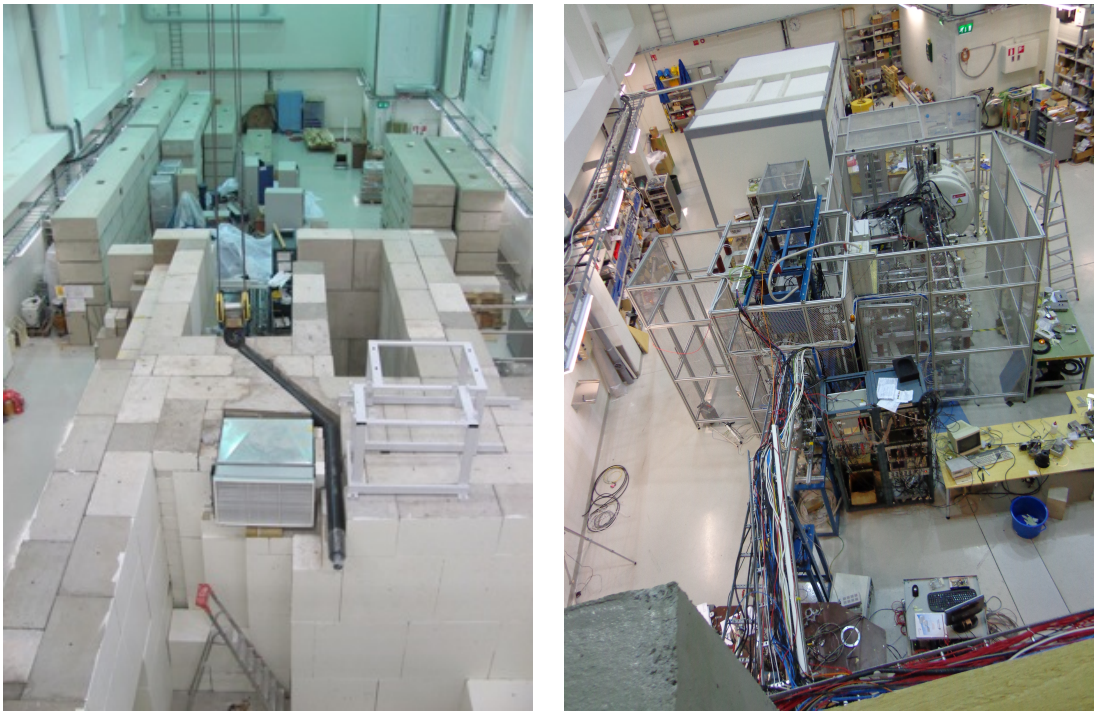

(a) Construction of IGISOL 4 (March 2011). (b) IGISOL 4 beam-line (December 2012).

**Figure 7.2:** The construction of the IGISOL 4 laboratory and the layout of the beam-line.

The ion optical simulations used to design the ConeTrap have been presented. These were used to acquire a ConeTrap design that provides 10 $\mu$s acceptance time and a uniform potential central region. Cone electrode shapes were investigated to provide efficient injection and extraction at high voltages and asymmetric potentials were sought and found to improve both the acceptance time and the injection-extraction efficiency of the trap. Fast-switching circuitry has been designed to reduce the effect of the changing voltages on the ions during injection and extraction and the ConeTrap has been constructed and built with materials with low out-gassing properties to optimise the vacuum achievable in the trap. The ConeTrap was designed primarily for optical pumping of ions in vacuum, however other applications,

immediately accessible with the current ConeTrap and with modifications, are also presented.

Results of the commissioning of the beam-line, required before the installation of the ConeTrap, have been presented. This effort concentrated on the spectroscopic study of the hyperfine structures and isotope shifts of stable and radioactive molybdenum isotopes (and comparing them to those acquired at the IGISOL facility previously). The agreement of these results confirms that the operation of the facility is back up to the standards achieved at IGISOL 3. The counting rates, however, exceeded those of IGISOL 3 by almost a factor of three. With the new sensitivity the hyperfine structure of $^{107}$Mo was measured for the first time and the ground state spin of the nucleus has been determined to be low, either 1/2 or 3/2, almost certainly excluding an onset of oblate deformation. The $^{107}$Mo spectra were acquired over several hours, thus demonstrating the long term stability of IGISOL 4. The long-term stability of the facility will allow the measurement of hyperfine spectra that were previously too weak to be observed.

Commissioning strategies for the ConeTrap have been presented and are, at the time of writing, being performed at the IGISOL 4. Upon completion a new wave of spectroscopic studies concentrating around $Z \sim 28$ (Cr, Fe, Co and Ni) will commence at the facility. Entirely new, trap-enabled, spectroscopy can commence as soon as the ConeTrap mean storage lifetime exceeds 10 ms. At this point the development of the IGISOL 4 facility (phase 1) will be complete.

# APPENDIX A

# Emittance

The emittance of an ion beam describes the position and momentum distributions of the ions in phase space [88]. The conservation of emittance follows from Liouville's theorem:

$$\frac{d\rho}{dt} = \frac{\partial\rho}{\partial t} + \sum_i \left( \frac{\partial\rho}{\partial q_i}\frac{\partial q_i}{\partial t} + \frac{\partial\rho}{\partial p_i}\frac{\partial p_i}{\partial t} \right) = 0$$

which shows that the density of an arbitrarily infinitesimal region ($dqdp$) in the emittance distribution ($\rho(q,p)$) is constant over time (where $q$ and $p$ are the particle positions and momenta respectively). The total volume of the emittance profile thus stays constant and no area can disperse or concentrate in ion density [89].

The emittance of an ion beam is typically split into the longitudinal component and two transverse components. The longitudinal emittance is a measure of the energy and temporal spread of an ion bunch and is given by [90],

$$\epsilon_{long} = \Delta E \Delta t \tag{A.1}$$

where $\Delta E$ and $\Delta t$ are the energy spread and bunch size respectively. The longitudinal emittance is an important consideration for efficient injection into ion traps. Equation A.1 shows that a continuous beam has an infinite longitudinal emittance and, at the IGISOL, ion bunches of $\Delta E$ $\sim$1 eV and $\Delta t$ $\sim$10 $\mu$s [10, 58] have a longitudinal emittance of around $10^{-5}$ eV seconds.

The transverse emittance is a measure of the transverse velocity of the ions with respect to the axial velocity and reflects the divergence of the beam. This parameter is described by the transverse position, $x$, and angular deviation, $x' = v_x/v_z$ with the total emittance given by [91],

$$\epsilon_x = \int\int dx dx'.$$

The angular deviation, $x'$, changes with axial velocity (resulting in a change in emittance). A normalised emittance, independent of the velocity of the ion beam, is given by,

$$\epsilon_{xn,r} = \beta\gamma\epsilon_x$$

for relativistic beams, which can be simplified to,

$$\epsilon_{xn} = \beta\epsilon_x \simeq \frac{v_x}{v_z}\epsilon_x$$

for non-relativistic beams [91]. The normalised emittance can be used to compare the beam emittance at each point in a path regardless of beam velocity.

Normalised emittance is usually quoted as the product of length and angular divergence, typically $\pi \cdot mm \cdot mrad$. The emittance of the ion beam at the IGISOL facility is reduced to $\sim 3\pi$·mm· mrad after cooling in the Cooler-Buncher [10].

The conservation of emittance is lost under the influence of inelastic interactions such as collisions, but is conserved for ions passing through electrostatic and magnetic fields, which only act to alter the shape of the emittance profile. Electrostatic and magnetic lenses can thus be used to transport ions along a beam line and avoid losses from divergence. Ion optics along the path manipulate the transverse emittance to avoid losses from divergence and to optimize the overlap between the ion and laser beams for spectroscopy. Figure A.1 shows common emittance profiles found in ion beams. Emittance profiles of real beams are usually Gaussian distri-

butions and therefore a root-mean squared emittance or an emittance of a certain proportion of the beam (such as 90%) is used instead. A beam waist is formed when the ion beam converges to a minimum spatial extent from which it then starts to diverge. Beam transport most often involves repeatedly forming waists between regions of large spatial extent. A near parallel beam is used for greater transport lengths to minimise aberrations. Near parallel beams are formed at the IGISOL to optimise beam overlap with similar, waist forming, Gaussian laser beams.

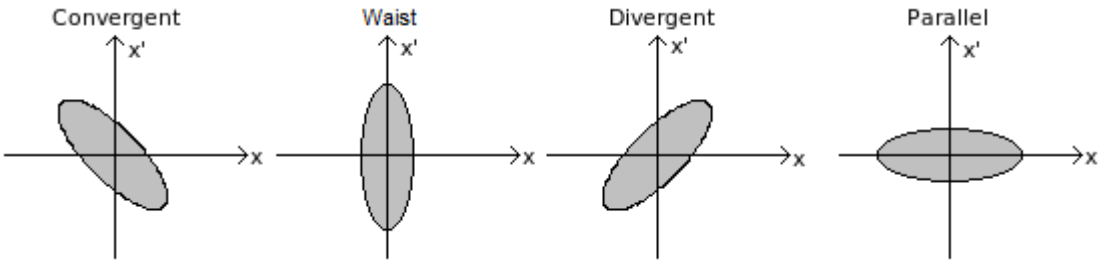


**Figure A.1:** Common emittance profiles of ion beams.

# APPENDIX B

# Designs of future ConeTraps

In this work, alternative designs and applications of the ConeTrap have been considered. Listed here are applications that require additional electrodes or modifications to the beam-line itself. These include the "high density" ConeTrap, for two-photon spectroscopy, the "Dual-stability" ConeTraps, for providing doubly-charged, ultra-pure ion ensembles, and the "fast-beam" ConeTrap, for collinear laser spectroscopy of fast moving (30 keV) trapped ions.

## B.1 "High-density" ConeTrap

The addition of a negative potential barrel electrode to one side of the central region enables the formation of high densities in the ConeTrap. Figure B.1 shows the structure of the "high-density" ConeTrap, the potential created by the negative barrel electrode (and the contraction of the ion orbits it can create).

Figure B.2 shows the stability regions of the high-density ConeTrap as a function of HV cone electrode and barrel electrode voltage at constant LV cone electrode voltages of 830 V and 850 V. Higher densities can be achieved with larger potentials on the barrel electrode and, at constant $V_B$, increasing $V_{HV}$ shifts the orbital 'waist' towards the HV cone electrode (as shown in Figure B.1(a)).

Figure B.3 shows the change in density of the ion orbit within the 'lip' of the

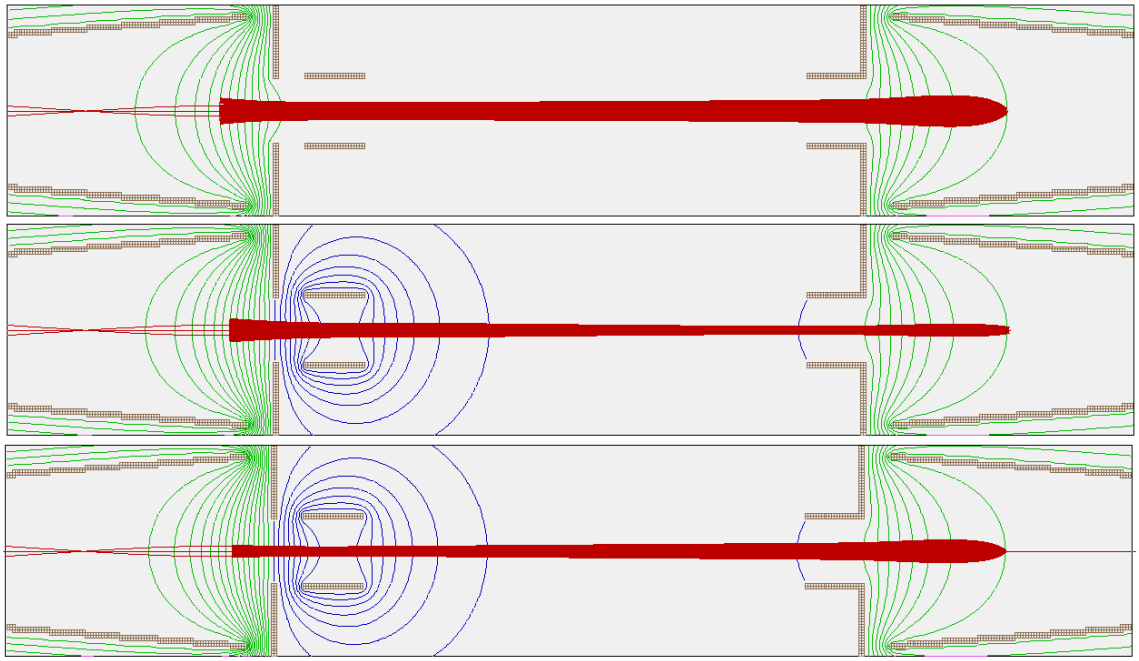

(a) Orbital shapes and potential contours of a "high-density" ConeTrap. Contours are in steps of 100 V with 0 V and below shown in blue. The ion orbits shown are; (top) typical orbital shape with a grounded barrel electrode and $V_{HV} = 1250$ V, (middle) compressed ion orbits within the 'lip' of the back disc electrode ($V_{HV} = 1480$ V and $V_B = -800$ V) and (bottom) compressed ion orbits within the barrel electrode ($V_{HV} = 1600$ V and $V_B = -800$ V).

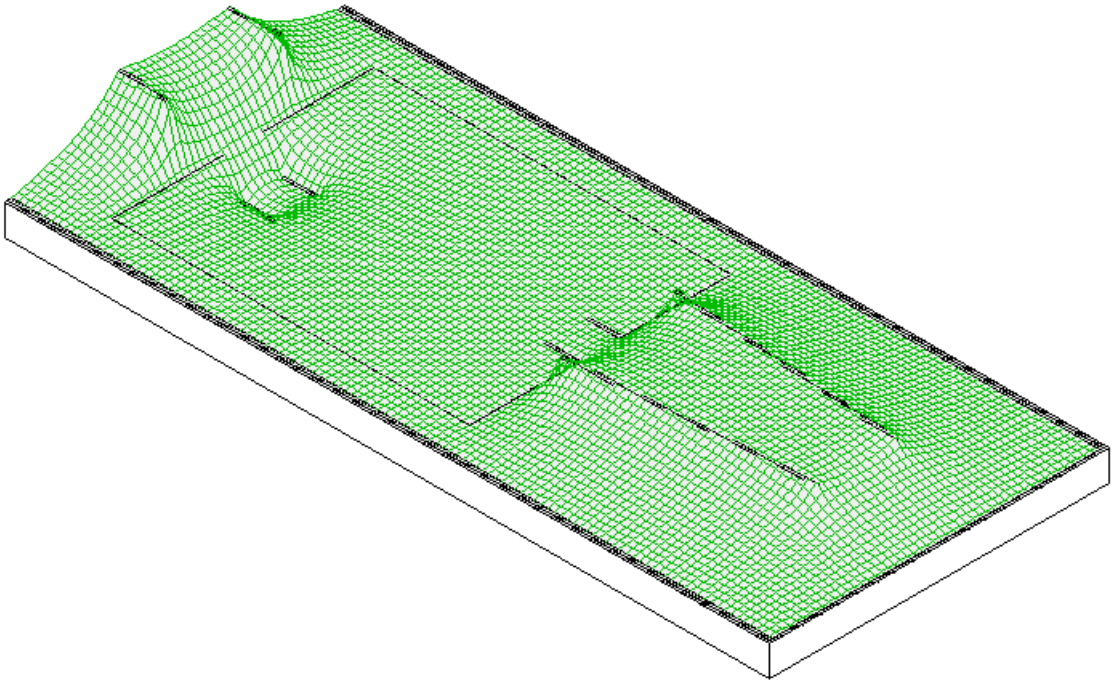

(b) Shape of the electrostatic potential inside a focusing ConeTrap, with $V_{HV} = 1480$ V and $V_B = -800$ V.

**Figure B.1:** Structure, orbital shape, potential contours and 3D potential of the "high-density" ConeTrap. The simulations used $V_{LV} = 830$ V. The barrel electrode is 10 mm long with a 12 mm diameter and a 5 mm gap between it and the disc electrode. The aperture 'lip' of the back disc electrode is 10 mm.

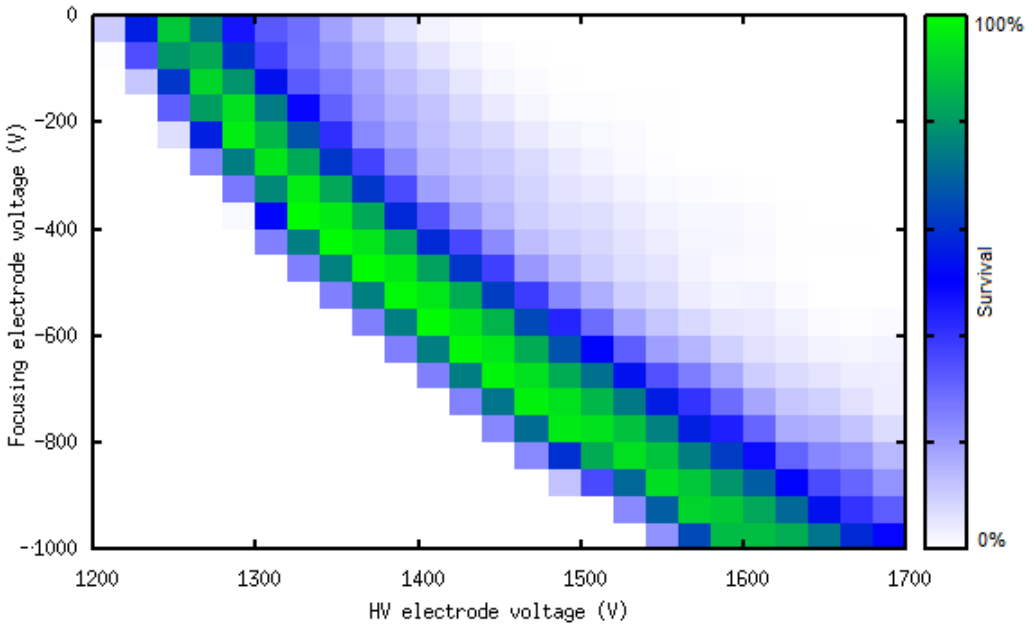


(a) LV cone electrode at 830 V.

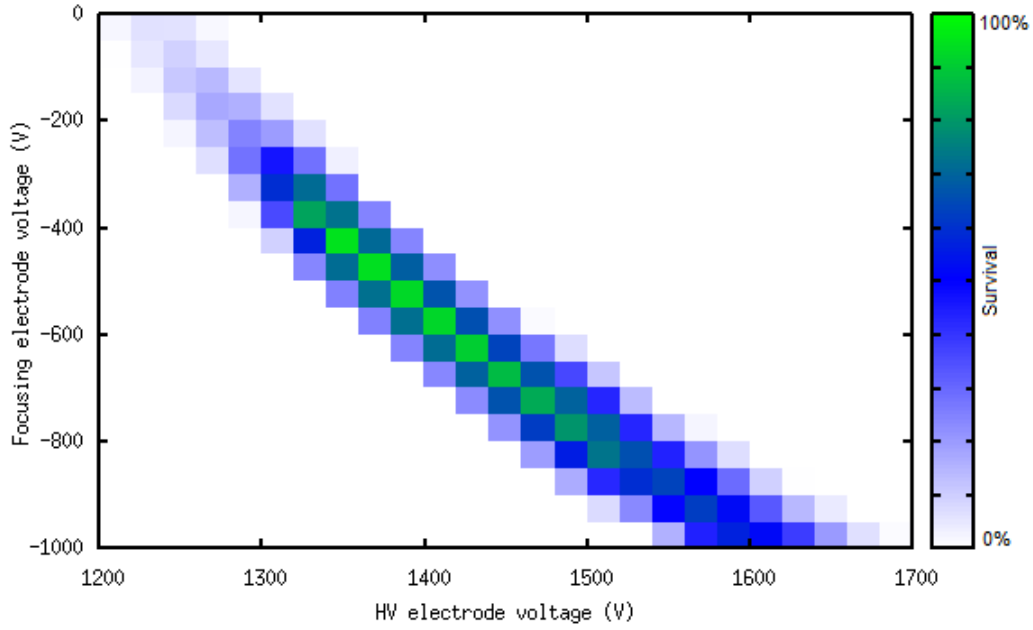


(b) LV cone electrode at 850 V.

**Figure B.2:** Stable regions of the "high-density" ConeTrap.

back disc electrode. A minimum waist of ∼0.5 mm radius can be achieved with $V_B$ =-800 V.

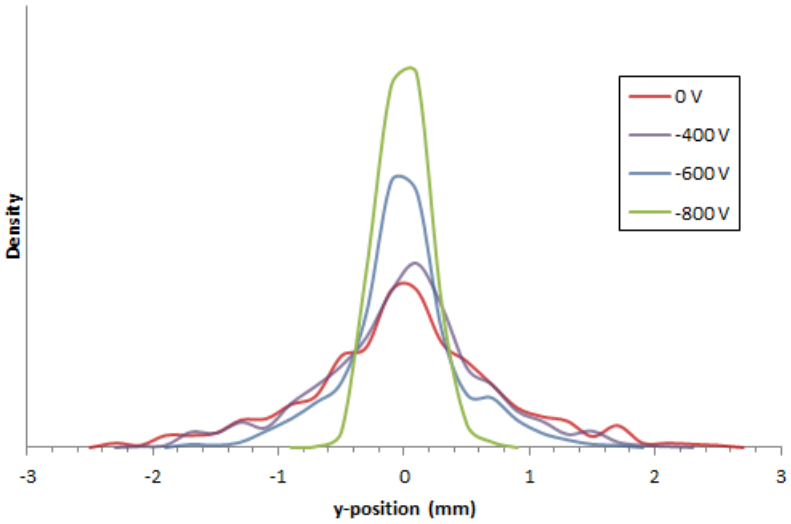


**Figure B.3:** Transverse density of ions at the orbital waist, located within the 'lip' of the back disc electrode, in a "high-density" ConeTrap. Shown are the densities of ions along the y-axis relative to x, the axial direction, and z, the direction of laser pumping. The simulations used an LV cone electrode potential of 830 V, with the HV cone electrode set at 1250, 1320, 1400 and 1480 V for the barrel electrode potentials of 0, -400, -600 and -800 V respectively, each achieving 100% trapping efficiency.

The orbital waist of the high-density ConeTrap is intended to provide a spectroscopic point where high power density laser beams can act and enable two-photon transitions. The transverse Doppler effect of the ion motion is canceled out by the use of counter-propagating laser beams at a frequency equivalent to $\Delta E/2$. Ion motion acts to boost one frequency and contract the other, resulting in the transition occurring at one, velocity-independent frequency. It will furthermore be possible to use the 'lip' of the back disc electrode to define the position of greatest ion density and apertures on this 'lip' will be used to align laser beams onto the central axis.

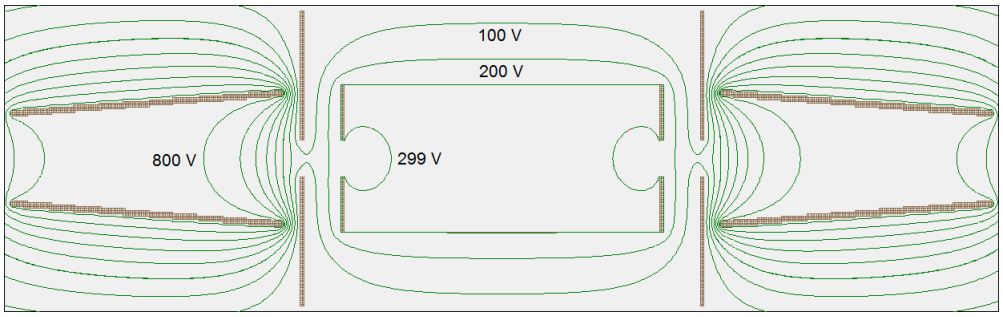


(a) Structure and potential contours of a "Dual-stability" ConeTrap. Contours are in steps of 100 V with an additional 299 V contour illustrating the extent of the fringe fields inside the (300 V) ionisation chamber.

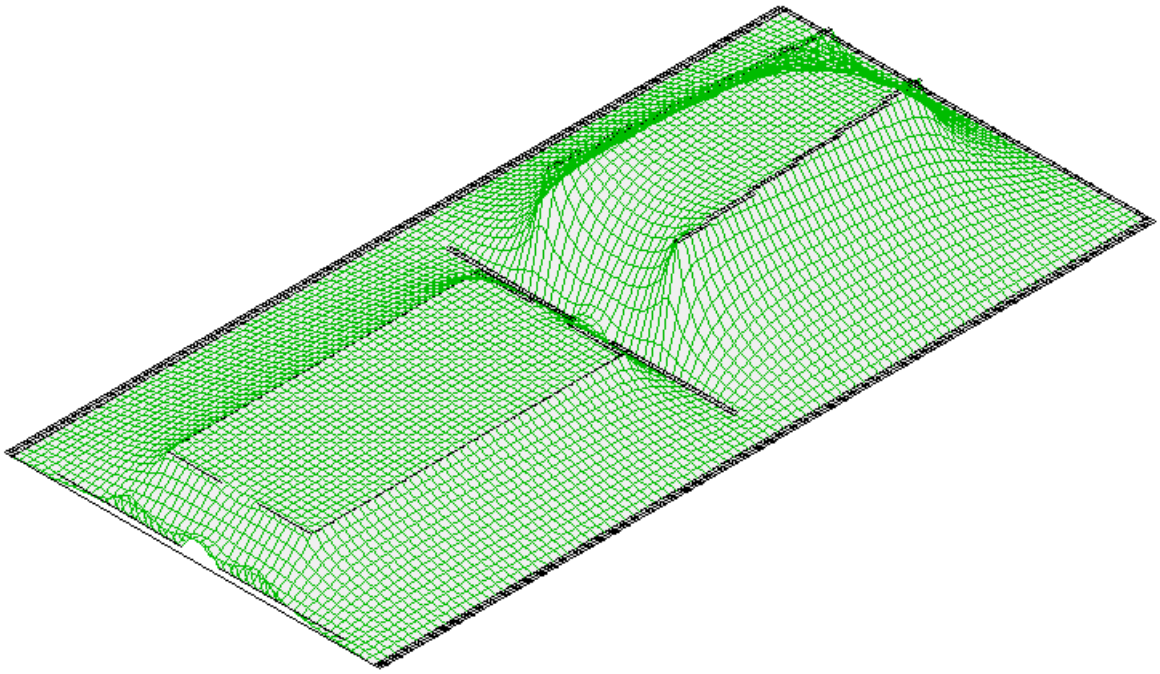

(b) Shape of the electrostatic potential inside a "Dual-stability" ConeTrap.

**Figure B.4:** Structure, potential contours and 3D potential of the "Dual-stability" ConeTrap, with cone electrodes and ionisation chamber set at 830 V and 300 V respectively. The ionisation chamber is 90 mm long with 12 mm apertures and 10 mm gaps between it and the disc electrodes.

## B.2 "Dual-stability" ConeTrap

A novel use of the ConeTrap is to place it in front of the Cooler-Buncher, allowing a continuous beam of $1^+$ ions to pass through but resonantly ionising selected species to $2^+$. The $2^+$ ions experience twice the potential due to their increased charge and are trapped inside the ConeTrap. The intensity of resonantly ionised $2^+$ ions thus builds up in the ConeTrap in a manner free of injection considerations and, as the trapping ratios ($V_{LV,HV}$(V)/$E_{ion}$(eV)) are both <2, the cone electrode voltages can be set to trap the ions in an asymmetric orbit. The ultra-pure ensemble of $2^+$ ions can then be extracted for spectroscopy. The central section would however require an applied potential to Doppler shift ions into resonance with the laser beams and prevent ions being resonantly ionised outside the trap.

Ultra-pure $2^+$ ion ensembles can also be acquired from trapped $1^+$ ions with a conventional ConeTrap by adding a smaller inner chamber in the centre of the trap. Placed between the grounded electrode discs (Figure B.4), the chamber has little effect on the stability of $1^+$ ions orbiting (symmetrically) in the lower stability region (Figure B.5) for a wide range of potentials. The shape of the ion orbits change with the chamber voltage and the decrease in stability for the $1^+$ ions in Figure B.5 at $V_{ch} = -400$ V is due to the ions shifting from the parallel to focused orbits.

The orbit of the injected $1^+$ ions rapidly destabilizes as the chamber approaches 600 V. Before this point however ions of twice the charge as those orbiting in the LV stability region will orbit in the HV stability region if the chamber is between 200 V to 350 V, as shown in Figure B.5 (assuming the two different ions have the same kinetic energy within the chamber). In such a configuration $1^+$ ions orbiting in the LV stability region that are resonantly ionised to the $2^+$ state inside the "ionisation chamber" will orbit in a stable HV mode. This unusual dual stability arises from the $2^+$ ions gaining more energy in the potential troughs, created by the

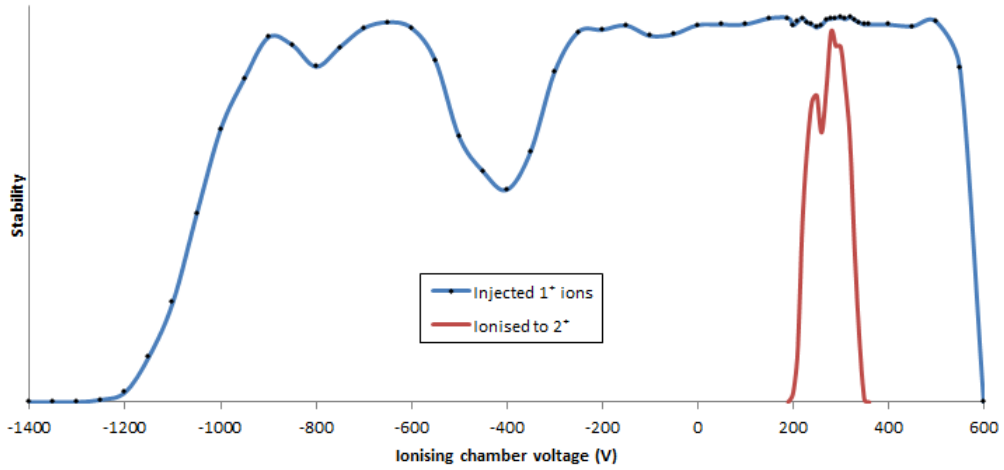


**Figure B.5:** Stability of an ion transferring from the LV stability region to the HV stability region upon ionisation from $1^+$ to $2^+$ inside the ionisation chamber of in an "Dual-stability" ConeTrap.

grounded disc electrodes, due to their increased charge (Figure B.6). Such ions can be separated from the rest of the ion bunch upon extraction by exploiting either their increased kinetic energy (time-of-flight gating) or charge (electrostatic deflection). The separation of the singly and doubly charged ions allows them to be individually counted and the efficiency of the resonant transfer determined. Efficient transfer can be used to provide an ultra-pure ion bunch for spectroscopy as no contaminant or non-photo resonant process can produce stably orbiting $2^+$ ions within the trap.

The symmetric design of this "dual-stability" ConeTrap couples the acceptance time and the released bunch size and reduces the maximum efficiency to ~50-60%. Both issues can be addressed by exploiting a double cone electrode, where a second set of disc and cone electrode are placed behind the ConeTrap and the first (central) cone electrode acts as a platform for the second (Figure B.7). Injected $1^+$ ions orbit between the front and back cone electrodes. The acceptance time is thus increased by the combination of the $1^+$ ions transit through the central cone electrode and the reduced potential required on the back cone electrode to reflect the lower energy ions. Upon ionisation to $2^+$ in the ionisation chamber, species can orbit asymmetrically between the front and central cone electrodes. The $2^+$ ions bunch in the central cone

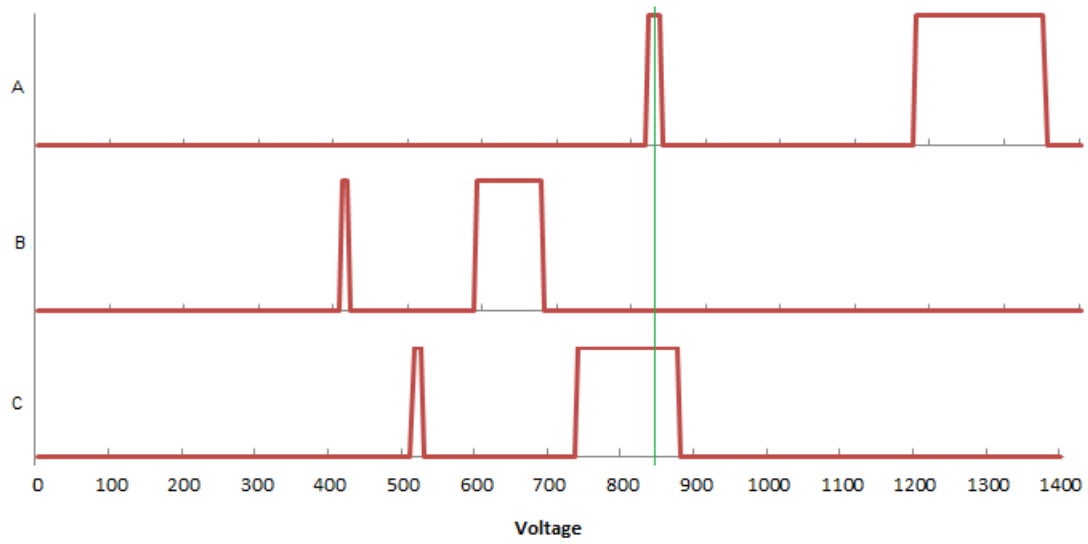


**Figure B.6:** Figure illustrating the change in stability regions as ions are resonantly ionised inside the "dual-stability" ConeTrap. The trapping potential is shown by the green line. The stability regions shown are, A: $1^+$ ions in LV stability region, B: $2^+$ ions experiencing twice the trapping potential due to their increased charge, and C: $2^+$ ions produced inside the ionisation-chamber.

electrode due to their asymmetric orbit, thus reducing losses upon extraction. The shape and size of the back electrode can be altered to further increase the acceptance time without alteration to the extracted $2^+$ ion bunch size.

The approximate potentials required for parallel orbits in the LV and HV stability regions are given by the ratios $R_{LV} = 1.04$ and $R_{HV} = 1.6$ respectively, where the potentials are given by $V_{LV,HV}(\mathrm{V}) = R_{LV,HV} E_{ion}(\mathrm{eV})$. The front cone electrode (or both cone electrodes for the symmetric "dual-stability" ConeTrap) is fixed at 830 V to reflect 800 eV $1^+$ ions in the LV stability region whilst also reflecting $2^+$ ions in the HV stability region. The required energy of the $2^+$ ions, with respect to the grounded discs, is therefore $E_{2^+}(\mathrm{eV}) = 2V_F(\mathrm{V})/R_{HV}$ and the difference between $E_{2^+}(\mathrm{eV})$ and $E_{1^+}(\mathrm{eV})$ gives the required ionisation chamber potential. The central cone electrode potential is then $V_C(\mathrm{V}) = R_{LV} E_{2^+}(\mathrm{eV})$ and the back cone electrode potential is $V_B(\mathrm{V}) = (E_{1^+}(\mathrm{eV}) - V_C(\mathrm{V}))R'_{LV,HV} + V_C(\mathrm{V})$, where the $R'_{LV,HV}$ term is the ratio for the back cone electrode and is a function of size and shape. The required voltages for the respective electrodes, in terms of the stability ratios and

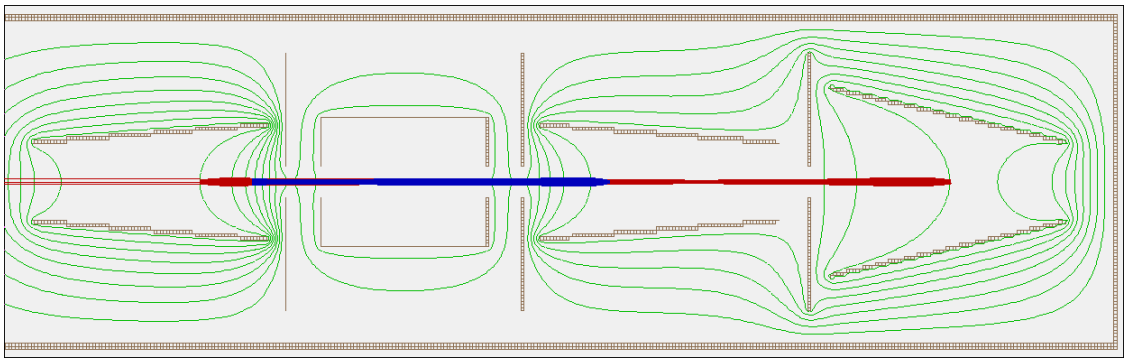

(a) Potential contours and typical ion orbits inside an acceptance-independent "dual-stability" ConeTrap. Contours are in steps of 100 V, with injected and contained $1^+$ orbits shown in red and contained $2^+$ orbits shown in blue.

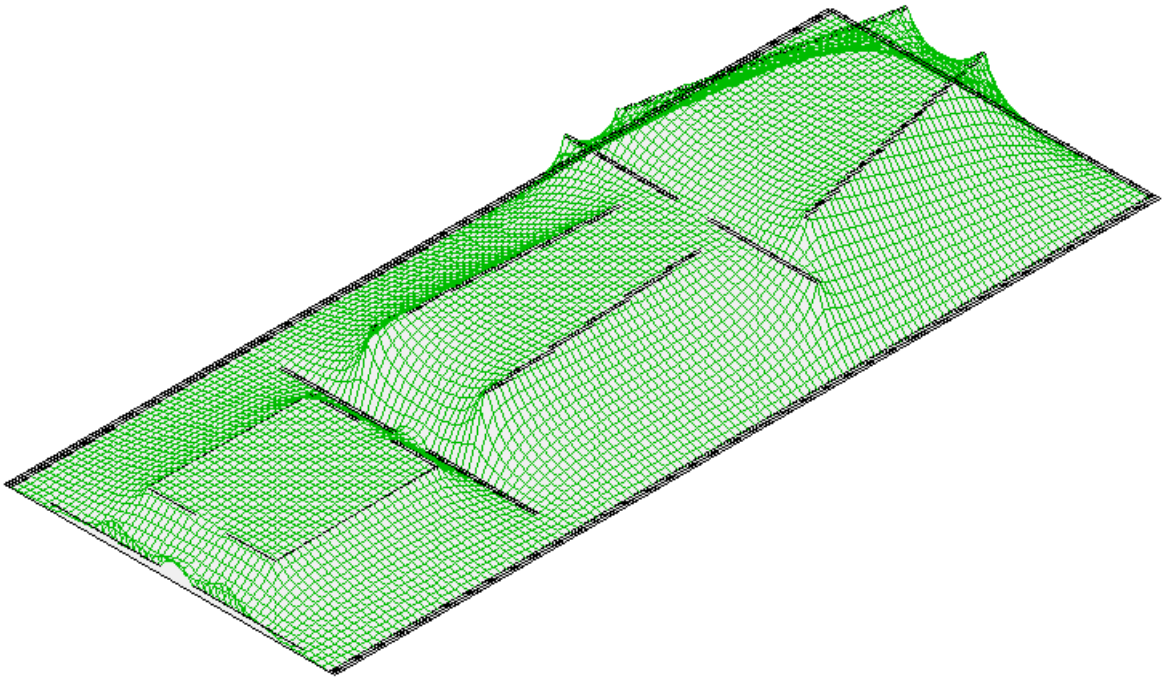

(b) Shape of the electrostatic potential inside an acceptance-independent "dual-stability" ConeTrap.

**Figure B.7:** Structure, orbital shape, potential contours and 3D potential of the acceptance-independent "dual-stability" ConeTrap, with the front, middle and back cone electrodes at 830, 545 and 807 V respectively and the ionisation chamber at 250 V (requiring an injection-extraction voltage of 500 V). The acceptance time for the $1^+$ ions is $\sim$25 $\mu$s and the bunch size of the extracted $2^+$ ions is $\sim$9 $\mu$s.

$E_{1^+}$, are:

$$
\begin{aligned}
V_F &= E_{1^+}(eV) R_{LV} \\
V_I &= E_{1^+}(eV) \left( \frac{2R_{LV}}{R_{HV}} - 1 \right) \\
V_C &= E_{1^+}(eV) \frac{R_{LV}^2}{R_{HV}} \\
V_B &= E_{1^+}(eV) \left( R'_{LV,HV} \left( 1 - \frac{R_{LV}^2}{R_{HV}} \right) + \frac{R_{LV}^2}{R_{HV}} \right).
\end{aligned}
$$

## B.3 "Fast-beam" ConeTrap

A trap capable of operating at the potentials commonly used in collinear laser spectroscopy can be realised by mounting the cone electrodes on high-voltage platforms either side of a grounded box containing the light collection region (thus allowing spectroscopy to be performed on the contained ions). This would increase the interaction time between the contained ions and the laser beam, thus increasing the efficiency of spectroscopy experiments. A possible design for a "fast-beam" ConeTrap is shown in Figure B.8 (where only half of the trap is shown). The design assumes 250 mm long insulators, similar to the one currently used at the exit to the high-voltage region, and has a ∼100 mm long grounded box bordered by two grounded electrodes (in the centre to fit the light collection apparatus). Focusing barrel electrodes are required to counteract the divergence of the ions as they rise to the platform voltage. The ground electrodes and barrel electrodes both have diameters of 20 mm and have lengths of 50 mm and 10 mm respectively. There are 115 mm and 105 mm gaps between the barrel electrodes and the disc and ground electrodes, respectively, and gaps of 10 mm between the central box and the ground electrodes. The drop to ground potential focuses the ions in the light collection region, increasing overlap with the axial laser beam.

Figure B.9 shows the symmetric stable regions of the "fast-beam" ConeTrap.

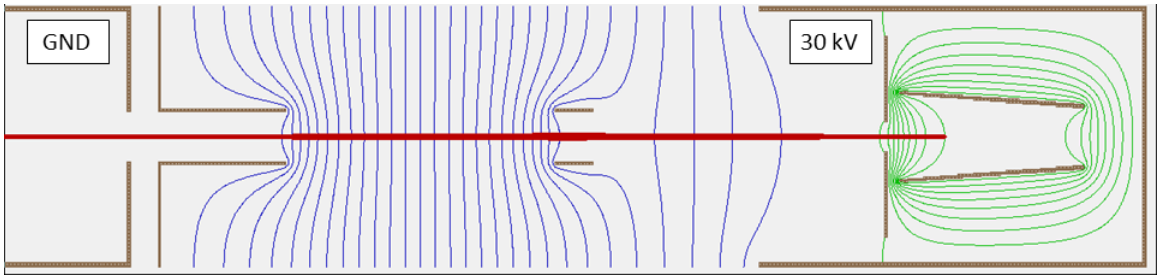


**Figure B.8:** Structure, potential contours and orbital shape of a "fast-beam" ConeTrap (only half is shown). Simulation used 850 V cone electrode and -4000 V focusing electrode potentials with respect to a 30 kV platform. Contours are in steps of 1000 V in the central region from ground up to 29 kV (blue) and in steps of 100 V in the cone electrodes from 30 kV up (green).

The focusing elements increase the stability of the ConeTrap as ions exiting the cone electrodes with large angular divergence are focused back towards the central axis. The tuning voltage of the light collection region, used to Doppler shift the ions into resonance, has a wide range of voltages that have no detrimental effect on the stability of the IGISOL beams (up to ±15 kV compared to the ±5 kV typical at the IGISOL). The tuning voltage does affect the radial density of the ions in the light collection region, however our commonly used negative tuning voltages act to further focus the ions (providing greater densities).

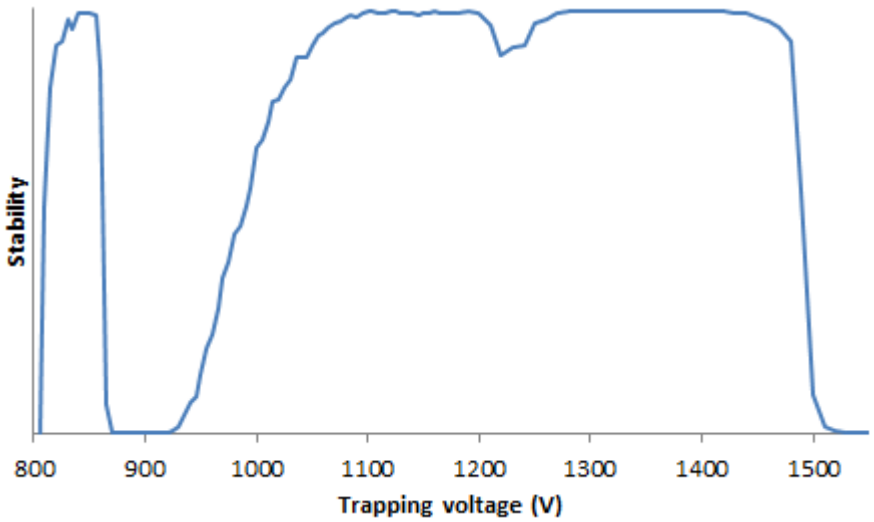


**Figure B.9:** The stable regions of the "fast-beam" ConeTrap, assuming symmetric trapping potentials, injected with the 'test' ion bunch.

# References

[1] J. Pauli W. "Zur Frage der theoretischen Deutung der Satelliten einiger Spektrallinien und ihrer Beeinflussung durch magnetische Felder". *Naturwissenschaften* 12 (1924), pp. 741–743.

[2] H. Schüler and T. Schmidt. *Phys. Z.* 94 (1935), pp. 457–468.

[3] D. Hughes and C. Eckart. "The effect of the motion of the nucleus on the spectra of Li I and Li II". *Physical Review* 36 (1930), pp. 694–698.

[4] W. Pauli and R.Peierls. *Phys. Z.* 32 (1931).

[5] S. L. Kaufman. "High resolution laser spectroscopy in fast beams". *Optics Communications* 17 (1976), pp. 309–312.

[6] J. Billowes et al. "Laser spectroscopy of radioisotopes and isomers at the IGISOL facility, Jyväskylä". *Czechoslovak Journal of Physics* 50 (2000), pp. 249–252.

[7] P. Campbell et al. "Progress of laser spectroscopy at the IGISOL". *Hyperfine Interactions* 127 (2000), pp. 83–90.

[8] J. Ärje et al. "The ion guide isotope separator on-line, IGISOL". *Nuclear Instruments and Methods A* 247 (1986), pp. 431–437.

[9] H. Penttilä et al. "Status report of the Jyväskylä ion guide isotope separator on-line facility". *Nuclear Instruments and Methods in Physics Research Section B: Beam Interactions with Materials and Atoms* 126 (1997), pp. 213 –217.

[10] I. Moore, P. Dendooven, and J. Ärje. "The IGISOL technique - three decades of developments". *Hyperfine Interactions* (2013), pp. 1–46.

[11] A. Nieminen et al. "Beam cooler for low-energy radioactive ions". *Nuclear Instruments and Methods in Physics Research Section A: Accelerators, Spectrometers, Detectors and Associated Equipment* 469 (2001), pp. 244 –253.

[12] P. Campbell et al. "First results from laser spectroscopy on bunched radioactive beams from the JYFL ion-beam cooler". *The European Physical Journal A - Hadrons and Nuclei* 15 (2002), pp. 45–48.

[13] A. Nieminen et al. "Time Characteristics of the Ion Beam Cooler-Buncher at JYFL". *Hyperfine Interactions* 132 (2001), pp. 523–526.

[14] P. Campbell. "Optical pumping in an RF cooler buncher". *Hyperfine Interactions* 171 (2006), pp. 143–148.

[15] H. Penttilä et al. "Performance of IGISOL 3". *The European Physical Journal A - Hadrons and Nuclei* 25 (2005), pp. 745–747.

[16] B. Cheal and D. Forest. "Collinear laser spectroscopy at the new IGISOL 4 facility". *Hyperfine Interactions* 223 (2014), pp. 223–230.

[17] F. C. Charlwood et al. "Nuclear charge radii of molybdenum fission fragments". *Physics Letters B* 674 (2009), pp. 23–27.

[18] K. S. Krane. *Introductory Nuclear Physics*. Wiley, 1987.

[19] N. A. Jelley. *Fundamentals of nuclear physics*. Cambridge University Press, 1990.

[20] S. G. Nilsson. "Binding states of individual nucleons in strongly deformed nuclei". *Dan. Mat. Fys. Medd.* 29 (1955), pp. 1–69.

[21] R. Casten. *Nuclear structure from a simple perspective*. Oxford Science Publications. Oxford University Press on Demand, 2000.

[22] T. Seo. "Nilsson potential parameters for all mass regions". *Zeitschrift für Physik A Atomic Nuclei* 324 (1986), pp. 43–52.

[23] W. D. Myers and K.-H. Schmidt. "An update on droplet-model charge distributions". *Nuclear Physics A* 410 (1983), pp. 61 –73.

[24] E. W. Otten. "Nuclear Radii and Moments of Unstable Isotopes". *Treatise on Heavy Ion Science*. Ed. by D. Bromley. Springer US, 1989, pp. 517–638.

[25] B. Cheal et al. "The shape transition in the neutron-rich yttrium isotopes and isomers". *Physics Letters B* 645 (2007), pp. 133 –137.

[26] D. Forest and B. Cheal. "Physics highlights from laser spectroscopy at the IGISOL". *Hyperfine Interactions* 223 (2014), pp. 207–222.

[27] F. Charlwood. "Ground state properties of Mn and Mo using laser spectroscopic methods". PhD thesis. University of Manchester, 2010.

[28] J. C. Willmott. *Atomic Physics*. John Wiley and Sons Ltd., 1975.

[29] D. Budker, D. F. Kimball, and D. P. DeMille. *Atomic Physics: an exploration through problems and solutions*. Oxford University Press, 2004.

[30] H. Haken and H. C. Wolf. *The Physics of Atoms and Quanta*. 7th ed. Springer, 2005.

[31] H. G. Kuhn. *Atomic Spectra*. Longmans, 1962.

[32] A. Bohr and V. F. Weisskopf. "The influence of nuclear structure on the hyperfine structure of heavy elements". *Physical Review* 77 (1950), pp. 94–98.

[33] A. P. Galván et al. "Comparison of Hyperfine Anomalies in the $5S_{1/2}$ and $6S_{1/2}$ levels of $^{85}$Rb and $^{87}$Rb". *Physics Letters B* 655 (2007), pp. 114–118.

[34] H. Kopfermann. *Nuclear Moments*. Academic Press, New York, 1958.

[35] A. Corney. *Atomic and Laser Spectroscopy*. Oxford Science Publications, 2006.

[36] L. J. S Halloran et al. "Specific mass shift of potassium $5P_{1/2}$ state". *Optics Communications* 282 (2009), pp. 554–557.

[37] E. C. Seltzer. "$K$ X-Ray Isotope Shifts". *Phys. Rev.* 188 (1969), pp. 1916–1919.

[38] K. Heilig and A. Steudel. "Changes in mean-square nuclear charge radii from optical isotope shifts". *Atomic Data and Nuclear Data Tables* 14 (1974), pp. 613 –638.

[39] W. H. King. "Comments on the Article 'Peculiarities of the Isotope Shift in the Samarium Spectrum'". *Journal of the Optical Society of America* 53 (1963), pp. 638–639.

[40] E. Hecht. *Optics*. 4th ed. Addison Wesley, 2002.

[41] H. Penttilä. "The layout of the IGISOL 3 facility". *Hyperfine Interactions* (2012), pp. 1–12.

[42] E. O. Lawrence. "Method and apparatus for the acceleration of ions". Patent (US). Feb. 1934.

[43] D. Pagano, C. Gorse, and M. Capitelli. "Modeling Multicusp Negative-Ion Sources". *IEEE Transactions on Plasma Science* 35 (2007), pp. 1247 –1259.

[44] T. Kalvas et al. "Recent negative ion source activity at JYFL". *AIP Conference Proceedings* 1515 (2013). Ed. by O. Tarvainen and T. Kalvas, pp. 349–358.

[45] M. Lantz et al. "Design of a neutron converter for fission studies at the IGISOL facility". *Physica Scripta* 2012 (2012), p. 014020.

[46] H. Penttilä et al. "Fission yield studies at the IGISOL facility". *The European Physical Journal A* 48 (2012), pp. 1–11.

[47] R. Geller. "ECRIS: the electron cyclotron resonance ion sources - (status)". *Zeitschrift für Physik D Atoms, Molecules and Clusters* 21 (1991), S117–S121.

[48] O. Tarvainen. "Studies of electron cyclotron resonance ion source plasma physics". PhD thesis. University of Jyväskylä, 2005.

[49] J. Ärje et al. "Status report of the JYFL-ECR ion sources". *14th international workshop on ECR sources, ECRIS99*. Geneva, Switzerland.

[50] J. Huikari et al. "Production of neutron deficient rare isotope beams at IGISOL; on-line and off-line studies". *Nuclear Instruments and Methods in Physics Research Section B: Beam Interactions with Materials and Atoms* 222 (2004), pp. 632 –652.

[51] P. Dendooven et al. "The fission ion guide: Present performance and future development". *AIP Conference Proceedings* 447 (1998). Ed. by G. Fioni et al., pp. 135–142.

[52] J. Äystö and V. Rubchenya. "Neutron-rich nuclei and fission; recent developments and future aspects". *The European Physical Journal A - Hadrons and Nuclei* 13 (2002), pp. 109–115.

[53] L. Vainio. "Ion yields in HIGISOL experiments". MA thesis. University of Jyväskylä, 2012.

[54] P. Karvonen et al. "A Sextupole ion beam guide to improve the efficiency and beam quality at IGISOL". *Nuclear Instruments and Methods B* 266 (2008), pp. 4794–4807.

[55] P. Karvonen. "Fission yield studies with SPIG-equipped IGISOL: A novel method for nuclear data measurements". PhD thesis. University of Jyväskylä, 2010.

[56] I. D. Moore et al. "Development of a laser ion source at IGISOL". *Journal of Physics G: Nuclear and Particle Physics* 31 (2005), S1499.

[57] B. W. Tordoff. "Development of resonance ionization techniques at the Jyväskylä IGISOL". PhD thesis. University of Manchester, 2007.

[58] B. Cheal and D. Forest. "Collinear laser spectroscopy techniques at JYFL". *Hyperfine Interactions* 223 (2014), pp. 63–71.

[59] P. Campbell et al. "On-line laser spectroscopy of refractory radioisotopes at the JYFL IGISOL facility". *AIP Conference Proceedings* 455 (1998). Ed. by B. M. Sherrill, pp. 72–77.

[60] D. Eastham et al. "Position sensitive detection of photons in ultrasensitive fluorescent spectroscopy". *Optics Communications* 82 (1991), pp. 23 –26.

[61] R. E. Silverans, P. Lievens, and L. Vermeeren. "A sensitive measuring scheme in collinear fast-ion-beam laser spectroscopy: The optical pumping, state-selective neutralization and particle detection sequence". *Nuclear Instruments and Methods in Physics Research Section B: Beam Interactions with Materials and Atoms* 26 (1987), pp. 591 –597.

[62] H. D. Zeman. "Deflection of an ion beam in the two-dimensional electrostatic quadrupole field". *Review of Scientific Instruments* 48 (1977), pp. 1079–1085.

[63] W. Paul. "Electromagnetic Traps for Charged and Neutral Particles (Nobel Lecture)". *Angewandte Chemie International Edition in English* 29 (1990), pp. 739–748.

[64] A. G. Marshall and S. Guan. "Observation, manipulation, and uses for magnetron motion in ion cyclotron resonance mass spectrometry". *Physica Scripta* 1995 (1995), p. 155.

[65] A. G. Marshall, C. L. Hendrickson, and G. S. Jackson. "Fourier transform ion cyclotron resonance mass spectrometry: A primer". *Mass Spectrometry Reviews* 17 (1998), pp. 1–35.

[66] G. Savard et al. "A new cooling technique for heavy ions in a Penning trap". *Physics Letters A* 158 (1991), pp. 247 –252.

[67] V. Kolhinen et al. "Penning trap for isobaric mass separation at IGISOL". *Nuclear Instruments and Methods in Physics Research Section B: Beam Interactions with Materials and Atoms* 204 (2003), pp. 502 –506.

[68] A. Jokinen et al. "Ion manipulation and precision measurements at JYFLTRAP". *The European Physical Journal A - Hadrons and Nuclei* 25 (2005), pp. 27–30.

[69] T. Eronen et al. "JYFLTRAP: a Penning trap for precision mass spectroscopy and isobaric purification". *The European Physical Journal A* 48 (2012), pp. 1–21.

[70] A. Fardi. "ConeTrap: An electrostatic ion trap for atomic and molecular physics". PhD thesis. Stockholm University, 2001.

[71] H. T. Schmidt et al. "Conetrap: A compact electrostatic ion trap". *Nuclear Instruments and Methods in Physics Research Section B: Beam Interactions with Materials and Atoms* 173 (2001), pp. 523 –527.

[72] R. D. Knight. "Storage of ions from laser-produced plasmas". *Applied Physics Letters* 38 (1981), pp. 221–223.

[73] *Simion*. URL: `http://simion.com`.

[74] P. Reinhed et al. "Cryogenic keV ion-beam storage in ConeTrap - A tool for ion temperature control". *Nuclear Instruments and Methods A* 621 (2010), pp. 83–90.

[75] M. Quack et al., eds. *Quantities, Units and Symbols in Physical Chemistry*. 3rd ed. The Royal Society of Chemistry, 2007.

[76] J. Sugar and A. Musgrove. "Energy levels of molybdenum, Mo I through Mo XLII". *Journal of Physical & Chemical Reference Data* 17 (1988), pp. 155–239.

[77] G. Fricke and K. Heilig. *Nuclear Charge Radii, Landolt - Börnstein - Group I Elementary Particles, Nuclei and Atoms*. Ed. by H. Schopper. Vol. 20. Springer, 2004.

[78] R. Rodríguez-Guzmán et al. "Charge radii and structural evolution in Sr, Zr, and Mo isotopes". *Physics Letters B* 691 (2010), pp. 202 –207.

[79] F. Buchinger et al. "Systematics of nuclear ground state properties in $^{78-100}$Sr by laser spectroscopy". *Physical Review C* 41 (1990), pp. 2883–2897.

[80] P. Lievens et al. "Nuclear ground state properties of $^{99}$Sr by collinear laser spectroscopy with non-optical detection". *Physics Letters B* 256 (1991), pp. 141 –145.

[81] C. Thibault et al. "Hyperfine structure and isotope shift of the $D_2$ line of $^{76-98}$Rb and some of their isomers". *Physical Review C* 23 (1981), pp. 2720–2729.

[82] P. Campbell et al. "Laser Spectroscopy of Cooled Zirconium Fission Fragments". *Physical Review Letters* 89 (2002), p. 082501.

[83] B. Cheal et al. "Laser Spectroscopy of Niobium Fission Fragments: First Use of Optical Pumping in an Ion Beam Cooler Buncher". *Physical Review Letters* 102 (2009), p. 222501.

[84] M. Keim et al. "Laser-spectroscopy measurements of $^{72-96}$Kr spins, moments and charge radii". *Nuclear Physics A* 586 (1995), pp. 219 –239.

[85] S. Raman et al. "Transition probability, B(E2), from the ground to the first-excited 2+ state of even-even nuclides". *Atomic Data and Nuclear Data Tables* 36 (1987), pp. 1 –96.

[86] P. Möller et al. "Axial and reflection asymmetry of the nuclear ground state". *Atomic Data and Nuclear Data Tables* 94 (2008), pp. 758 –780.

[87] J. Skalski, S. Mizutori, and W. Nazarewicz. "Equilibrium shapes and high-spin properties of the neutron-rich A $\approx$ 100 nuclei". *Nuclear Physics A* 617 (1997), pp. 282 –315.

[88] L. Vályi. *Atom and Ion Sources*. John Wiley and Sons, 1977.

[89] R. C. Tolman. *The principles of statistical mechanics*. Dover publications inc., 1979.

[90] P. Van Duppen. "Isotope Separation On Line and Post Acceleration". *The Euroschool Lectures on Physics with Exotic Beams, Vol. II*. Ed. by J. Al-Khalili and E. Roeckl. Vol. 700. Lecture Notes in Physics. Springer Berlin Heidelberg, 2006, pp. 37–77.

[91] T. Sokollik. "Beam Emittance". *Investigations of Field Dynamics in Laser Plasmas with Proton Imaging*. Springer Theses. Springer Berlin Heidelberg, 2011, pp. 55–59.